Modeling global cosmogenic nuclide production through 1st principles


David C. Argento



A dissertation

submitted in partial fulfillment of the

requirements for the degree of


Doctor of Philosophy



University of Washington

2013

Reading Committee:

Dr. John O. Stone, Chair

Dr. Erika Harnett

Dr. Eric Steig

Program Authorized to Offer Degree:

Earth and Space Sciences

University of Washington

**Abstract**

Modeling global cosmogenic nuclide production through 1st principles

David C. Argento

Chair of the Supervisory Committee:

Dr. John O. Stone, Associate Professor

Earth and Space Science

The work contained in this thesis is focused on utilizing radiation transport code software as the basis for developing a well validated, first-principles model of global terrestrial cosmogenic nuclide production rates. The state-of-the-art radiation transport code, MCNPX, is utilized to model the terrestrial radiation field. Folding the radiation field neutron and proton results with cosmogenic nuclide production cross-sections yields production rates. This comprehensive, first-principles model is used to investigate characteristics of cosmogenic nuclide production. The goal of the work is to constrain uncertainties in cosmogenic nuclides by better understanding production systematics. Greater understanding of cosmogenic nuclide production rate systematics will assist in constraining uncertainties in cosmogenic nuclide production rate scaling, thereby reducing uncertainties in calculations based on sample nuclide concentrations

exposure ages, erosion rates, and burial dating. Furthermore, novel uses of cosmogenic nuclides, currently unachievable due to uncertainties, will be enabled by further constraining these.

The model is benchmarked against Dr. Paul Goldhagen's ER-2 aircraft neutron monitor measurements, the Knyahinya meteorite *in-situ* cosmogenic nuclides, the Beacon Heights sandstone core measurements, and estimated sea level production rates. In this work, I examine: the production rates of each commonly used cosmogenic nuclide as a function of altitude and latitude; the angular distribution of nuclide-producing cosmic-ray particles as a function of altitude and latitude; subsurface production rate systematics; and the production of $^{36}$Cl in both the atmosphere and the oceans.

# Acknowledgments

I would like to thank my advisor, Dr, John Stone, for his time, energy and guidance in developing my skills as a thorough and effective researcher. John played a critical role in my growth and provided essential perspective throughout this process.

I would like to thank the members of my committee: Drs. Erika Harnett, Eric Steig, Bruce Nelson, and Greg Hakim for their guidance and insight. I would also like to thank Dr. Robert Winglee, the Chair of the Earth and Space Sciences Department for his support.

I owe a debt of gratitude to Drs. Paul Goldhagen, Gregg McKinney and Laurie Waters whose MCNPX modeling expertise was essential to the success of this project. This work benefited greatly from collaborations with Dr. Robert C. Reedy, Keran O'Brien and Dr. L. Keith Fifield. I would also like to thank the members of CRONUS-Earth who were supportive of my efforts and leant advice and knowledge regarding cosmogenic nuclide formation and applications.

My gratitude goes to my colleagues in the Earth and Space Sciences Department, my friends and my family who have supported me through this journey. Above all, I am grateful to my wife, Valerie, for her support, mentoring and love.

Finally, I would like to dedicate this dissertation to my parents, Joseph Argento and Susan Millington, particularly my father who passed away before seeing me finish this journey. For their unwavering faith in me, their generosity, their never-ending support, and especially their unconditional love, I am deeply grateful.

# Table of Contents

# Chapter 1

A model of global cosmogenic nuclide production

## THESIS STATEMENT

This thesis describes a first-principles model of global terrestrial cosmogenic nuclide production rates. The radiation transport code, MCNPX, is used to simulate the flux and spectra of cosmic rays in the atmosphere, ocean and uppermost crust. Neutron and proton spectra are then folded with reaction cross-sections to derive cosmogenic nuclide production rates. This comprehensive, first-principles model is used to investigate characteristics of cosmogenic nuclide production. The goal of the work is to better understand production systematics. Greater understanding of cosmogenic nuclide production rate systematics will assist in constraining uncertainties in production rate scaling, thereby reducing uncertainties in applications such as exposure dating, erosion rate measurements, and burial dating.

## BACKGROUND

Cosmogenic nuclides are formed when a highly energetic cosmic-ray collides with the nucleus of an atom in the atmosphere or rock with enough energy to fragment the nucleus, a process known as spallation (Dunai, 2010). These high energy particles (protons and atomic nuclei stripped of their electrons) likely originate in supernovae. Because the particles are charged, they interact with the galactic, solar and earth's magnetic field. Most low-energy ($< 500$ MeV) particles are deflected away from the earth either by the solar field or by the geomagnetic field. The high-energy particles that penetrate the magnetic fields collide with the top of the atmosphere creating a cascade of radiation. Some of this radiation penetrates the entirety of the atmosphere where it can cause nuclear spallations in the rock (*in-situ*) and produce new atoms. A portion of these new atoms are geologically useful, such as $^3$He, $^{10}$Be, $^{21}$Ne, $^{26}$Al, $^{36}$Cl, among others. While this

2

is a continuous process, the rarity of these reactions means that *in-situ* production rates at the surface of the earth are low enough (on the order of 10 atom $g^{-1}$ $yr^{-1}$) that measuring the abundance of these isotopes requires high sensitivity mass spectrometry. Secondary neutrons and protons are the component of the radiation field primarily responsible for nuclide production. Production rates closely follow the neutron and proton flux, increasing with both geomagnetic latitude and altitude. The geomagnetic field varies over time in both orientation and strength causing geologic samples to experience production rates varying with time.

Geoscientists use cosmogenic nuclides to investigate a variety of earth surface processes such as surface exposure dating (Lal, 1988), erosion measurement (Bierman and Steig, 1996; Lal, 1991), and burial dating (Balco and Stone, 2005). Dating glacial erratics and glacial moraines has been the mainstay of *in-situ* cosmogenic studies, amassing an invaluable data set in reconstructing the glacial histories of the Quaternary Period (Balco et al., 2005; Balco et al., 2013; Nishiizumi et al., 1991; Nishiizumi et al., 1989; Schaefer et al., 2009; Stone et al., 2003; Zreda et al., 1991).

The accuracy of these methods is directly related to the accuracy with which the production rate of the isotope is known. Calculating production rates is typically done via a "scaling scheme" (Desilets and Zreda, 2003; Dunai, 2001; Lal, 1991; Lifton et al., 2008; Stone, 2000). Scaling schemes are parameterized for altitude and geomagnetic latitude; some account for the geomagnetic field's variations in time. Extensive calibration sampling has been conducted to provide benchmarks for the scaling schemes. None of the schemes satisfactorily match the calibration data. As noted in (Schimmelpfennig et al., 2012), scaling schemes vary by 10% at

sea level high latitude. Furthermore, the time-invariant Lal/Stone scaling scheme performs better than the time-varying neutron monitor based schemes.

Calibration sampling will never sufficiently cover the three primary dimensions of nuclide production: (i) altitude, (ii) latitude, and (iii) the time-dependent geomagnetic shielding because sites where exposure ages are accurately and independently known are scarce. In addition to the primary controls of altitude, latitude, and geomagnetic shielding, cosmogenic nuclide production rates vary with geometric shielding by obstruction to incoming cosmic-rays (Barford and Davis, 1952; Conversi and Rothwell, 1954; Heidbreder et al., 1971). Composition also has a minor effect on production rates due to the "matrix effect" (Masarik and Reedy, 1994). Thickness of a sample will affect the average production rate. Correction for these factors are mostly based on based on cosmic-ray experiments from the 1940s through the 1970s, nuclear theory and a small number of more recent calibration measurements on rock samples (Farber et al., 2008; Nishiizumi et al., 1989).

A necessary complement to calibration sampling is development of the physical systematics underpinning nuclide production. Better understanding of these underpinnings will extend our ability to accurately predict production rates away from these calibration sites. For this purpose, I have built a first-principles nuclide production model using the radiation transport code, MCNPX, implementing all known aspects of physics relevant to nuclide production.

## GOALS & OBJECTIVES

The over-arching goal of the research described in this dissertation is to address gaps in the current state of the knowledge by building and validating a cosmogenic nuclide production rate model based on first principles. While many aspects of terrestrial nuclide production have been addressed by some form of theory or empirical measurement, many assumptions have gone untested. Previous physics-based models were limited to either high latitude studies (Masarik and Reedy, 1995) or atmospheric production (Kovaltsov et al., 2012; Masarik and Beer, 2009). Older radiation transport codes were constrained by computational limitations and the state of high-energy nucleus interaction models. The latter was aimed at calculating atmospheric production rates of nuclides such as $^7$Be, $^{10}$Be, $^{14}$C, and $^{36}$Cl. This model brings all of those capabilities together, being suitable for both atmospheric as well as *in-situ* calculations.

To determine how well this production rate model performs, it has been benchmarked against (i) Dr. Paul Goldhagen's aircraft neutron monitor measurements (Goldhagen et al., 2004; Goldhagen et al., 2003; Goldhagen et al., 2002; Gordon et al., 2004; McKinney et al., 2012), (ii) the Knyahinya meteorite *in-situ* cosmogenic nuclides (Graf 1990) (Graf et al., 1990), (iii) the Beacon Heights sandstone core $^{10}$Be and $^{26}$Al measurements (unpublished data), and (iv) sea level production rates from rock samples. These four benchmarks are discussed in detail in Chapter 3.

## CONTRIBUTIONS

Attempts at first-principles modeling of cosmogenic nuclide production rates have been made in the past (Dep et al., 1994; Dunne, 2002; Masarik and Beer, 2009; Masarik and Reedy, 1995). Much of the work was investigating single aspects of cosmic-ray nuclide production (e.g. – low energy neutron absorption, atmospheric production, high-latitude *in-situ* production). This work is intended to address all aspects of nuclide production.

Model accuracy is directly tied to the accuracy of the high energy fragmentation models used in radiation transport models and the accuracy of nuclear reaction cross-sections for relevant nuclide formation. Both the high-energy fragmentation models and the cross-sections for geologically relevant nuclide producing reactions have seen advances in the last two decades making modeling more functional for the purposes of exploring the systematics of global nuclide production. This model benefits from the latest generation of high-energy fragmentation models CEM and LAQGSM (James et al., 2006; Mashnik, 2008). Results compare well with Paul Goldhagen's ER-2 and ground level neutron measurements. Sea level high latitude production rates predicted by this model are also close to the current sea level production rate calibration estimates for commonly used nuclides.

A unique contribution to the field of cosmogenic nuclide production lies in the comprehensiveness and modularity of my model. I have compared four different input radiations, including the physics-prescribed proton and alpha GCR flux as described by (Castagnoli and Lal, 1980; McKinney et al., 2006; Nymmik et al., 1992; Usoskin and Kovaltsov,

2006) for high geomagnetic latitude ( $>\sim 60°$) simulations. These GCR models are all

parameterized for solar modulation, the affect the sun's magnetic field will have on the energy

spectra at earth's location. For low latitude, the GCR spectra are then modified to account for

the geomagnetic field through rigidity cutoff calculations as a function of zenith and azimuth,

forming the source radiation for the radiation transport software. Close attention was paid to

physics options within MCNPX to ensure particles and reactions with the extreme energies of

cosmic rays were handled optimally. Alternative cross-section performance can also be

evaluated as those become available (Caffee et al., 2013).

This model has yielded rich results characterizing the systematics of cosmogenic nuclide

production. In this work, I examine: (i) the production rates of each commonly used cosmogenic

nuclide as a function of altitude and latitude; (ii) the angular distribution of nuclide-producing

cosmic-ray particles as a function of altitude and latitude; (iii) subsurface production rate

systematics; and (iv) production of $^{36}$Cl in both the atmosphere and the oceans.

i. By analyzing the production rate results as a function of altitude, I have generated

polynomial fits to the data in natural log space. Because of the range of particle energies

and the multiplicity of particles in the upper atmosphere, a simple exponential cannot

adequately describe the production rates with altitude. These fitted scaling functions will

be more accurate than previous simplifying assumptions (Lal, 1991). Results are

discussed both in Chapter 3 and 4.

ii. The current method for shielding correction is based on studies with limited resolution,

limited altitude and latitude coverage, and very large uncertainties (Barford and Davis,

1952; Conversi and Rothwell, 1954; Heidbreder et al., 1971; Lal, 1958). These studies

relied on measuring neutrons either in bulk or in relatively narrow energy ranges. Currently, shielding correction is calculated assuming a simple cosine distribution for incoming cosmic-rays at all altitudes and latitudes:

$$I(\theta) = cos^{2.3}(\theta) \text{ (Gosse and Phillips, 2001)}$$ Eq. 1.1

Where $I$ is cosmic-ray intensity and $\theta$ is the zenith angle. The simple description neglects the effects of high-angle particle scattering, and has never been verified experimentally. To investigate angular production distribution in my simulations, neutrons and protons were binned both in energy and in angle; the results were then folded with production cross-sections. This was done for 6 points in geologic sampling altitudes for all geomagnetic latitudes. Chapter 4 discusses the results.

iii. The exact behavior of production rates with depth in rock has been difficult to characterize. In early studies analytical uncertainties were large and rock density was variable or poorly measured, leading to large disagreements between results (Table 3 of Gosse and Phillips, 2001). Most theory and practice assumes that production rates decrease as a simple exponential. Alternatively, (Masarik and Reedy, 1995) proposed a non-exponential subsurface production profile. Their modeling results indicate a flat production rate or "plateau" roughly 20 g/cm$^2$ deep (~8 cm) for production of $^{10}$Be in SiO$_2$, below which production decreased exponentially with an attenuation length of 157 g/cm$^2$. Little empirical evidence has been found to support such a plateau, in part, because the region in question is subject to erosion. I have developed three lithological simulations to investigate the subsurface profile. Production rate profiles are calculated for all commonly used nuclides. Results generally conform to the exponential form, but the attenuation length is longer near the surface for all nuclide production profiles.

Chlorine-36 produced from potassium is the one profile that shows a flattened region of production at the surface, but it is quite shallow. Results are discussed in detail in Chapter 4.

iv.　The $^{36}$Cl/Cl ratio of seawater is a unique long-term average cosmic-ray recorder. Effectively all $^{36}$Cl produced in the atmosphere should be delivered to the ocean rapidly compared to the 300,000 year half-life of this nuclide. Chlorine-36 production is calculated in both atmospheric and in ocean simulations as a function of latitude. These production rates are column and latitude integrated to calculate the total global production of $^{36}$Cl. In Chapter 5 I discuss the calculations and the measurements.

## OUTLINE OF THESIS

**Chapter 2** describes results of my first generation model. The model was limited to high geomagnetic latitude at the time. This chapter demonstrates the fine spatial resolution achievable with a comprehensive model and the proper post-processing. The model covered six commonly measured nuclides. Production rate ratios are shown to change with altitude as a result of each nuclide having a slightly different scaling.

**Chapter 3** describes in detail the modeling methods, validations and initial results after several refinements, enhancements and revisions to the model. The primary differences between the model described here and the model described in Chapter 2 are:

1. Use of a more optimal physics package within MCNPX
2. Corrected normalization for conversion from "current" to "flux"
3. Improved interpolation in cross section folding

4. Expansion of model to lower latitudes through the use of geomagnetic modification of GCR source radiation

5. Comparisons with Goldhagen neutron measurements improved through the use of geomagnetic modification of GCR source radiation.

**Chapter 4** focuses on model results that will most directly affect the accuracy of studies utilizing cosmogenic nuclides. The three primary components in this chapter are: (i) Fitting production rates as functions of altitude with polynomial exponentials, (ii) describing a new form of angular distribution for shielding corrections, and (iii) subsurface production rate profiles.

**Chapter 5** describes the efforts to bring together our measurements of seawater $^{36}$Cl and my simulations of atmospheric and seawater $^{36}$Cl production. Seawater $^{36}$Cl is unique as an integrated time-averaged signal of the cosmic-ray radiation field, and can be developed to be an important benchmark for terrestrial cosmic-ray models.

**Chapter 6** summarizes the work presented in the previous 4 chapters and discusses the research that will logically follow the work described here.

# REFERENCES

Balco, G., Rovey II, C.W., Stone, J., 2005. First Glacial Maximum in North America. Science 307, 222.

Balco, G., Schaefer, J.M., Grp, L., 2013. Exposure-age record of Holocene ice sheet and ice shelf change in the northeast Antarctic Peninsula. Quaternary Science Reviews 59, 101-111.

Balco, G., Stone, J., 2005. Measuring middle Pleistocene erosion rates with cosmic-ray-produced nuclides in buried alluvial sediment, Fisher Valley, southeastern Utah. Earth Surface Processes and Landforms 30, 1051-1067.

Barford, N.C., Davis, G., 1952. The Angular Distribution and Attenuation of the Star-Producing Component of Cosmic Rays. Proceedings of the Royal Society of London. Series A, Mathematical and Physical Sciences 214, 225-237.

Bierman, P., Steig, E.J., 1996. Estimating rates of denudation using cosmogenic isotope abundances in sediment. Earth Surface Processes and Landforms 21, 125-139.

Caffee, M.W., Nishiizumi, K., Sisterson, J.M., Ullmann, J., Welten, K.C., 2013. Cross section measurements at neutron energies 71 and 112 MeV and energy integrated cross section measurements ($0.1 < En < 750$ MeV) for the neutron induced reactions O(n,x)10Be, Si(n,x)10Be, and Si(n,x)26Al. Nuclear Instruments and Methods B 294, 479-483.

Castagnoli, G., Lal, D., 1980. SOLAR MODULATION EFFECTS IN TERRESTRAIL PRODUCTION OF CARBON-14. Radiocarbon 22, 133-158.

Conversi, N.C., Rothwell, P., 1954. Angular Distributions in Cosmic Ray Stars at 3500 Meters. Il Nuovo Cimento 12, 191-210.

Dep, L., Elmore, D., Fabryka-Martin, J., Masarik, J., Reedy, R.C., 1994. Production rate systematics of in-situ-produced cosmogenic nuclides in terrestrial rocks: Monte Carlo approach of investigating 35Cl(n,g)36Cl. Nuclear Instruments and Methods B 92, 321-325.

Desilets, D., Zreda, M.G., 2003. Spatial and temporal distribution of secondary cosmic-ray nucleon intensities and applications to in situ cosmogenic dating. Earth and Planetary Science Letters 206, 21-42.

Dunai, T.J., 2001. Infuence of secular variation of the geomagnetic field on production rates of in situ produced cosmogenic nuclides. Earth and Planetary Science Letters 193, 197-212.

Dunai, T.J., 2010. Cosmogenic nuclides: principles, concepts and applications in the Earth Surface Sciences, First ed. Cambridge University Press, Cambridge.

Dunne, J., 2002. Monte Carlo simulations of neutron fluxes for varying rock types. Nuclear Instruments and Methods 194, 226-228.

Farber, D.L., Meriaux, A.S., Finkel, R.C., 2008. Attenuation length for fast nucleon production of Be-10 derived from near-surface production profiles. Earth and Planetary Science Letters 274, 295-300.

Goldhagen, P., Clem, J., Wilson, J.W., 2004. THE ENERGY SPECTRUM OF COSMIC-RAY INDUCED NEUTRONS MEASURED ON AN AIRPLANE OVER A WIDE RANGE OF ALTITUDE AND LATITUDE. Radiation Protection Dosimetry 110, 387-392.

Goldhagen, P., Clem, J.M., Wilson, J.W., 2003. RECENT RESULTS FROM MEASUREMENTS OF THE ENERGY SPECTRUM OF COSMIC-RAY INDUCED NEUTRONS ABOARD AN ER-2 AIRPLANE AND ON THE GROUND. Advanced Space Research 32, 35-40.

Goldhagen, P., Reginatto, M., Kniss, T., Wilson, J.W., Singleterry, R.C., Jones, I.W., Van Steveninck, W., 2002. Measurement of the energy spectrum of cosmic-ray induced neutrons aboard an ER-2 high-altitude airplane. Nuclear Instruments and Methods A 476, 42-51.

Gordon, M.S., Goldhagen, P., Rodbell, K.P., Zabel, T.H., Tang, H.H.K., Clem, J., Bailey, P., 2004. Measurement of the Flux and Energy Spectrum of Cosmic-Ray Induced Neutrons on the Ground. IEEE Transactions on Nuclear Science 51, 3427-3434.

Gosse, J., Phillips, F., 2001. Terrestrial in situ cosmogenic nuclides: theory and application. Quaternary Science Reviews 20, 1475-1560.

Graf, T., Signer, P., Wieler, R., Herpers, U., Sarafin, R., Vogt, S., Fieni, C., Pellas, P., Bonani, G., Suter, M., Wolfli, W., 1990. Cosmogenic nuclides and nuclear tracks in the chondrite Knyahinya. Geochimica et Cosmochimica Acta 54, 2511-2520.

Heidbreder, E., Pinkau, K., Reppin, C., Schönfelder, V., 1971. Measurements of the Distribution in Energy and Angle of High-Energy Neutrons in the Lower Atmosphere. Journal of Geophysical Research 76, 2905-2916.

James, M.R., McKinney, G.W., Hendricks, J.S., Moyers, M., 2006. Recent enhancements in MCNPX: Heavy-ion transport and the LAQGSM physics model. Nuclear Instruments and Methods A 562, 819-822.

Kovaltsov, G.A., Mishev, A., Usoskin, I.G., 2012. A new model of cosmogenic production of radiocarbon 14C in the atmosphere. Earth and Planetary Science Letters 337, 114-120.

Lal, D., 1958. Investigations of nuclear interactions produced by cosmic rays, Tata Institute of Fundamental Research. Bombay University, Bombay, India, p. 116.

Lal, D., 1988. IN SITU-PRODUCED COSMOGENIC ISOTOPES IN TERRESTRIAL ROCKS. Annual Review of Earth Planet Science 16, 355-388.

Lal, D., 1991. Cosmic-ray labeling of erosion surfaces: in situ nuclide production rates and erosion models. Earth and Planetary Science Letters 104, 424-439.

Lifton, N.A., Smart, D.F., Shea, M.A., 2008. Scaling time-integrated in situ cosmogenic nuclide production rates using a continuous geomagnetic model. Earth and Planetary Science Letters 268, 190-201.

Masarik, J., Beer, J., 2009. An updated simulation of particle fluxes and cosmogenic nuclide production in the Earth's atmosphere. Journal of Geophysical Research - Atmospheres 114, 1-9.

Masarik, J., Reedy, R., 1994. Effects of bulk composition on nuclide production process in meteorites. Geochimica et Cosmochimica Acta 58, 5307-5317.

Masarik, J., Reedy, R.C., 1995. Terrestrial cosmogenic-nuclide production systematics calculated from numerical simulations. Earth and Planetary Science Letters 136, 381-395.

Mashnik, S.G., 2008. Overview and Validation of the CEM and LAQGSM Event Generators for MCNP6, MCNPX, and MARS15, 1st Workshop on Accelerator Radiation Induced Activation, Paul Scherrer Institut, Switzerland.

McKinney, G.W., Armstrong, H.J., James, M.R., Clem, J.M., Goldhagen, P., 2012. MCNP6 Cosmic-Source Option. Transactions of the American Nuclear Society 106.

McKinney, G.W., Lawrence, D.J., Prettyman, T.H., Elphic, R.C., Feldman, W.C., Hagerty, J.J., 2006. MCNPX benchmark for cosmic ray interactions with the Moon. Journal of Geophysical Research 111, 1-14.

Nishiizumi, K., Kohl, C.P., Arnold, J.R., Klein, J., Fink, D., Middleton, R., 1991. COSMIC-RAY PRODUCED BE-10 AND AL-26 IN ANTARCTIC ROCKS - EXPOSURE AND EROSION HISTORY. Earth and Planetary Science Letters 104, 440-454.

Nishiizumi, K., Winterer, E.L., Kohl, C.P., Klein, J., Middleton, R., Lal, D., Arnold, J.R., 1989. Cosmic Ray Production Rates of 10Be and 26Al in Quartz from Glacially polished Rocks. Journal of Geophysical Research 94, 17,907-917,915.

Nymmik, R.A., Panasyuk, M.I., Pervaja, T.I., Suslov, A.A., 1992. A Model of Galactic Cosmic Ray Fluxes. Nuclear Tracks and Radiation Measurements 20, 427-429.

Schaefer, J., Denton, G., Kaplan, M., Putnam, A., Finkel, R.C., Barrel, D.J.A., Andersen, B.G., Schwartz, R., Mackintosh, A., Chinn, T., Schluchter, C., 2009. High-Frequency Holocene Glacier Fluctuations on New Zealand Differ from the Northern Signature. Science 324, 622-625.

Schimmelpfennig, I., Schaefer, J.M., Goehring, B.M., Lifton, N.A., Putnam, A.E., Barrel, D.J.A., 2012. Calibration of the in situ cosmogenic 14C production rate in New Zealand's Southern Alps. Journal of Quaternary Science 27, 671-674.

Stone, J., 2000. Air pressure and cosmogenic isotope production. Journal of Geophysical Research 105, 23,753-723,759.

Stone, J., Balco, G., Sudgden, D.E., Caffee, M., Sass III, L., Cowdery, S., Siddoway, C., 2003. Holocene Deglatiation of Marie Byrd Land, West Antarctica. Science 299, 99-102.

Usoskin, I.G., Kovaltsov, G.A., 2006. Cosmic ray induced ionization in the atmosphere: Full modeling and practical applications. Journal of Geophysical Research 111, 1-9.

Zreda, M.G., Phillips, F.M., Elmore, D., Kubik, P.W., Sharma, P., Dorn, R.I., 1991. COSMOGENIC CL-36 PRODUCTION-RATES IN TERRESTRIAL ROCKS. Earth and Planetary Science Letters 105, 94-109.

# Chapter 2


## Modeling the Earth's Cosmic Radiation

## ABSTRACT

In this study, we use physics based cross sections and the radiation transport code MCNPX to develop a purely physics based global model of cosmogenic nuclide production. Modeling the earth as a series of concentric, spherical shells of various media, we propagate the radiation cascade resulting from bombarding the model with primary protons and helium nuclei. The hadronic component of the radiation cascade is tracked throughout the atmosphere as well as the upper region of simple, rock earth-planets. Tallying the energy spectrum throughout the geometry allows us to fold the energy dependent flux with excitation functions to determine nuclide specific spallogenic production rates and attenuation lengths. Using these results, we characterize facets of the radiation cascade and resulting productions rates that are currently unaccounted for in modern scaling schemes.


Preliminary results of our deep atmosphere model show nuclide dependent attenuation lengths, therefore, altitude dependent production ratios. Preliminary results from simple, homogeneous rock planets show production rate depth profiles that diminish at a rate inconsistent with a simple exponential, the currently accepted assumption.

15

# INTRODUCTION

*In-situ* cosmogenic nuclides provide powerful tools to quantify erosion, surface exposure ages, burial ages and other aspects of geomorphic history [1, 2]. Cosmogenic nuclide methods are all dependent on knowing nuclide production rates well at the sampling location. The latitude and altitude variation of production rates are predicted by scaling schemes [3-7]. More complete understanding of the physics of the radiation cascade will reduce systematic uncertainties in current global scaling schemes and help to predict nuclide production rates in the atmosphere and over the earth's surface. As part of the CRONUS-Earth project, a collaboration of researchers has undertaken an extensive sampling campaign to constrain the production rates of the primary *in-situ* produced nuclides, $^3$He, $^{10}$Be, $^{14}$C, $^{21}$Ne, $^{26}$Al, and $^{36}$Cl.

Our goal is to calculate nuclide production rates using a physics-based model and compare the results to these experimental values. By applying modern radiation transport codes to cosmic ray propagation through the atmosphere, and combining the calculated fluxes with the latest cross section data, we predict the cosmogenic nuclide production rates at all altitudes and latitudes, for air and for rocks of different chemical composition. We use the Monte Carlo N-Particle eXtended (MCNPX) code to characterize the particle flux responsible for cosmogenic nuclide production in a variety of geologic scenarios. In this paper, we report production rates as functions of altitude at high latitude, for the nuclides listed above.

Scaling schemes currently in use [3-8] assume that production rates of all nuclides vary with altitude in an identical manner and have generally been calibrated with $^{10}$Be production. Global

scaling models have been based on cosmic ray fluxes derived from extensive sets of photographic emulsion measurements [7] or from neutron monitor measurements [4-6]. Although both methods are sensitive to the range of cosmic ray energies that produce nuclides by spallation reactions, neither captures the detailed particle energy spectrum. Without information about variation in energy spectra, these scaling models have been applied assuming that production rates of the different nuclides vary identically. This assumption has been questioned based on theoretical and experimental data (*e.g.,* [9-12]). Excitation functions are unique to each nuclide production reaction, and there is evidence the energy distribution of cosmic ray neutrons and protons in the atmosphere changes with altitude and geomagnetic latitude [13-15] – hence it is likely that production rate scaling might differ from nuclide to nuclide. Our results presented below suggest that the assumption that nuclide production ratios are constant is incorrect, and that variations in production ratios may range up to 8% at sampling altitudes (between sea level and 6 km).


Recently, Goldhagen et al. [14], Sheu & Jiang [16] and Kowatari et al. [15] have measured differential neutron spectra at different altitudes, solar conditions and geomagnetic fields using Bonner Spheres, which are multiple neutron monitors with unique energy response functions [14]. These measurements provide data on the cosmic ray neutron energy spectrum that we can use for detailed comparisons with our calculations. High energy cross sections (excitation functions) for neutrons, the dominant particle responsible for spallation production of cosmogenic nuclides in the lower atmosphere, are also being measured for use with this model [17]. By combining these excitation functions with our calculated cosmic ray spectra, the model results can be directly compared with measured nuclide production rates. Note however, in this

case, we are comparing instantaneous model results with time integrated results of the irradiation history.

Radiation transport codes are designed to simulate the movement, generation and attenuation of various radiation types. MCNPX is the latest of several codes developed over the decades at Los Alamos National Laboratory for various physics particle transport applications. Modeling the cosmic-ray radiation cascade in MCNPX allows us to explore characteristics of the radiation field, which are difficult to measure. Direct measurements of the energy spectrum of the neutron component are extremely difficult, making data very sparse; and many particles' energy distributions are impossible to measure. With MCNPX, we can calculate the energy spectrum and direction of travel of all particles, at all altitudes.

## METHODS

The atmosphere is modeled as a series of approximately 100 concentric spherical shells of varying density (depending on the simulation). We use the US Standard atmospheric model [18] for those densities. The atmosphere is modeled up to 100 km, approximately the region where molecular diffusion affects the composition. Although atmospheric density is very low at this altitude ($<10^{-10}$ g/cm$^3$), the model is extended to ensure realistic treatment of the development of the muon spectrum from pion decay. Below the atmosphere, the lithosphere or the ocean is also modeled as concentric spherical shells.

We used the energy spectrum described in Castagnoli & Lal [19] and McKinney et al. [20] for the primary proton and alpha radiation respectively. We use the estimated long term solar average solar modulation of 550 MV [20-22]. For the high latitude (>~60° geomagnetic latitude), the source is isotropic at the upper surface of the atmosphere with particle energies from $10^1$ MeV to $10^6$ MeV/nucleon. Low latitude models are still in development.

Protons, alpha particles, neutrons, deuterons, tritons, He-3 nuclei, kaons, pions, and muons are all tracked and tallied throughout the geometry. In tracking these particles, MCNPX tallies both energy and direction of travel. For this paper we report particle spectra integrated over all incidence angles. Sato et al. [13, 23] have done similar work using a different radiation transport code, PHITS. Their work is primarily targeted towards radiation safety calculations for air travel.

Excitation functions for the production rates of each nuclide from every target, from both neutrons and protons are used to determine total production rates. For instance, for the production rate of $^{10}$Be in quartz ($SiO_2$), we use the excitation functions of both O and Si. Each excitation function is then convolved with the corresponding energy spectrum at each atmospheric depth. The excitation functions used in this study [24] were determined from a combination of irradiation measurements and theory. By folding in these excitation functions with our neutron and proton fluxes throughout the atmosphere, we have developed nuclide specific production rates as functions of altitude. Furthermore, attenuation lengths for each specific nuclide production rate can be determined and compared against each other.

Two general geometries have been developed, both of which are spherical:

i – Deep atmosphere: We ran one set of simulations with an artificially deep atmosphere that extends to twice the mass depth of the normal terrestrial atmosphere.   This allows us to investigate the development of the radiation cascade propagating through a pure medium without the effect of particles reflected from the surface of the earth.  Results reported are for atmospheric depth of 1033 $g/cm^2$ (sea level) and above.

ii – Homogeneous planets beneath the standard atmosphere: Models with granite and basalt layers below a standard atmosphere were used to investigate *in-situ* production rates and the effect of the underlying surface composition on the nucleonic flux above and below the air-ground boundary.  This approach allows us to investigate phenomena such as changes in the energy spectra of the nucleonic flux, neutron moderation and changes in the angular scattering characteristics of the radiation as it penetrates into materials of different compositions.  Furthermore, folding these flux results with excitation functions allows individual nuclide production rates to be determined and compared to experimentally calibrated rates in similar rock types.


## RESULTS

**Deep atmosphere**

Data from Goldhagen et al. [14] were used to benchmark the deep atmosphere model.  Their study describes results of measurements of the cosmic ray neutron spectrum at several levels in the atmosphere, using Bonner Spheres.  The measurements were taken in June 1997 during solar

minimum when values for the solar modulation parameter $\phi$ averaged 440 MV [13] or 404 MV [25]. This study also included simulation work similar to ours, using the MCNPX code.

There are two differences to note in this comparison: i) the measurements were made at solar minimum, whereas these simulations use solar average values; ii) the measurements were made over a range of geomagnetic latitudes, whereas our simulations use high latitude geomagnetic conditions. However, our results compare well qualitatively with the measured spectrum. The neutron spectra of our simulations have similar peaks centered at ~2 MeV and ~300 MeV - the evaporation and knock-on neutrons respectively.
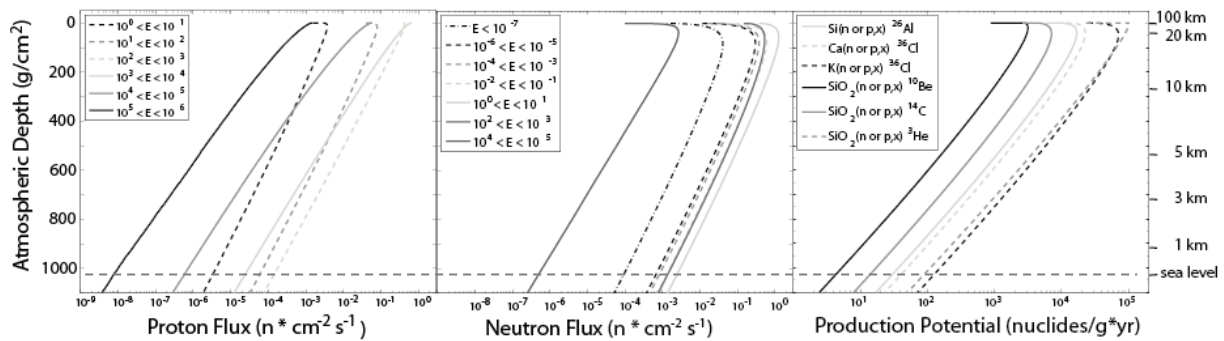


Figure 2.1 – Particle fluxes and productions rates of select nuclides in a deep atmosphere as functions of atmospheric depth.  A) MCNXP proton flux results, binned in energy of MeV.  B) Select MCNPX neutron flux results binned in energy of MeV.  C) Production rate potentials for $^{26}$Al, $^{10}$Be, $^{14}$C and $^{3}$He from silica ($SiO_2$), and $^{36}$Cl from pure elemental calcium and potassium.

Figure 2.1 shows proton and neutron fluxes, binned in decades of energy, as functions of atmospheric depth (altitude).  There are small but significant differences in the slope between different particle energies.  This indicates that the energy spectra of both protons and neutrons change subtly as the cascade develops through the atmosphere, and these fluxes have not reaches a strict equilibrium even in the lower troposphere.  Comparing the energy spectra of several altitudes normalized to the spectrum at 400 g/cm$^2$, Figure 2.2 further demonstrates that the energy spectrum of both neutrons and protons softens with atmospheric depth.  Therefore,

because production rates for different nuclides are sensitive to different regions of the proton and

neutron spectra, we expect them to change at different rates as a function of altitude.
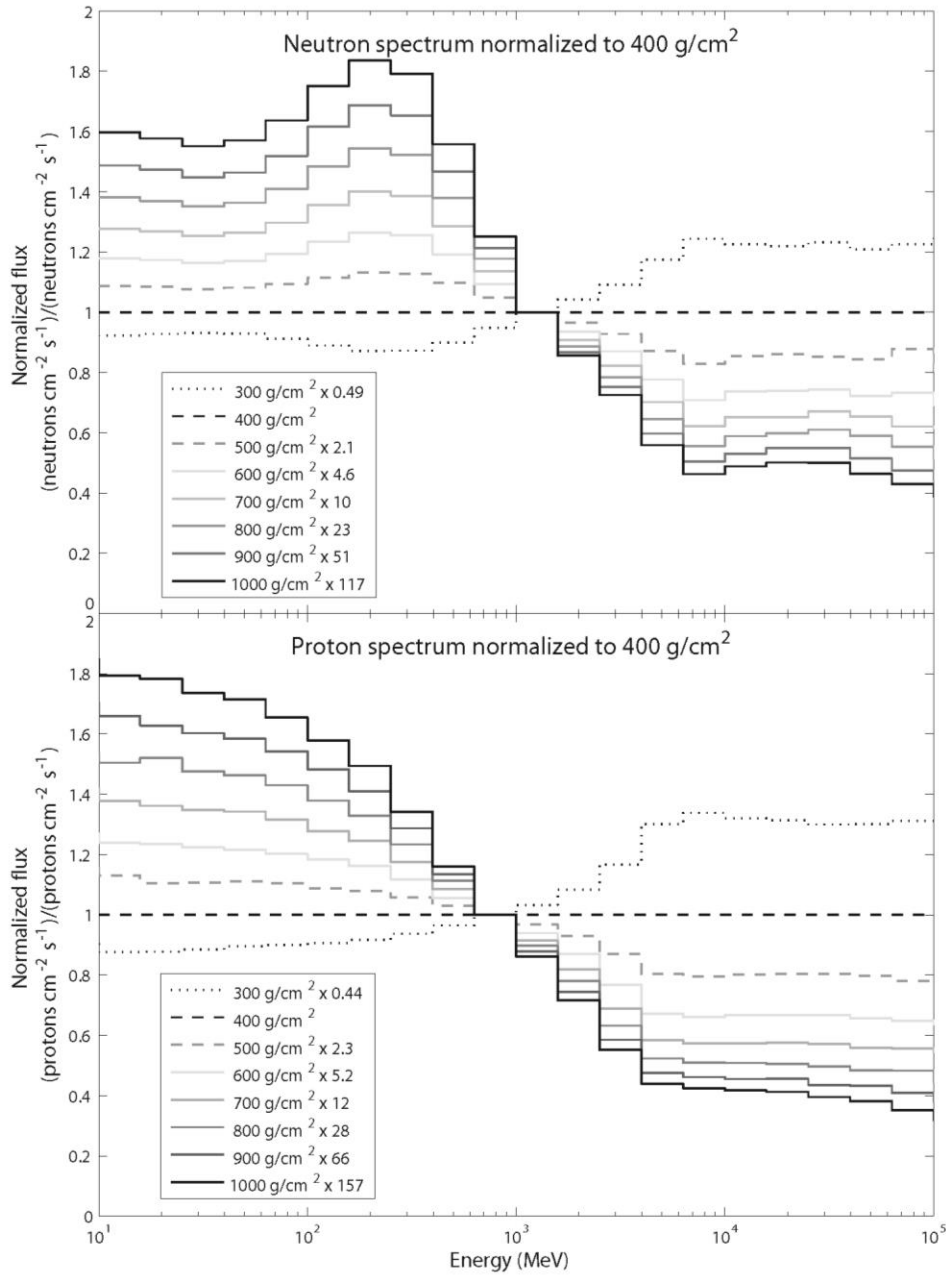


Figure 2.2 – Neutron and proton fluxes normalized to the 400 g/cm$^2$ spectra and scaled to overlay. In both cases, the spectrum steepens indicating comparatively fewer high energy particles, also known as softening.

For direct investigation of the production rates via these simulations, we use the neutron and proton energy spectrum flux values throughout the atmosphere, and fold them with the respective spallation cross sections. Production values are generated for each target material and both neutrons and protons for each nuclide in question. These values are then summed to give production rates in units of atoms per year per gram of target material in the rightmost panel of Figure 2.1. It is clear upon close inspection that the variation in production rate is not strictly exponential with atmospheric depth. The shape of the curves requires attenuation lengths to increase with increasing altitude. Production rates at sea level, listed in Table 2.1, agree well with calibration values for sea level, high latitude (e.g., Balco et al. 2008 [26] and forthcoming results from the CRONUS project).

| Nuclide | Target material | Production Rate (atoms g$^{-1}$ yr$^{-1}$) | Attenuation length (g cm$^{-2}$) | Production ratio to $^{10}$Be |
|---------|-----------------|--------------------------------------------|----------------------------------|-------------------------------|
| $^{10}$Be | SiO$_2$ | 4.1 | 129.7 | 1 |
| $^{14}$C | SiO$_2$ | 13.3 | 131.2 | 3.2 |
| $^{26}$Al | SiO$_2$ | 29 | 130.2 | 7.1 |
| $^{36}$Cl | Ca | 39 | 130.5 | 9.5 |
| $^{36}$Cl | K | 120 | 131.0 | 29.3 |

Table 2.1 – Cosmogenic nuclide production rates, attenuation lengths and production ratio to $^{10}$Be at sea level, high latitude. Rates are per unit mass of SiO$_2$ or elemental K and Ca.

While there are no target materials present in this simulation, the values represent the potential production rate, as if a small sample were suspended in the atmosphere at various altitudes. These results are not actual *in-situ* production rate estimates, although they are very close to those estimates. The lithology of each target material, has a small effect on *in-situ* production rates because different average multiplicities, scattering and absorption characteristics depend on bulk rock composition. These effects are explored in the following simulations.

**Simple planet**

Simple, homogeneous planet geometries were developed to investigate the possible boundary

effects on *in-situ* production rates as the radiation cascade transitions from the atmosphere to the

underlying rock.  We chose to develop two lithological models for our initial investigations –

granite and basalt – as they represent the two most common end members of sampled rock and

have a significantly different elemental composition.  These simulations were run using a solar

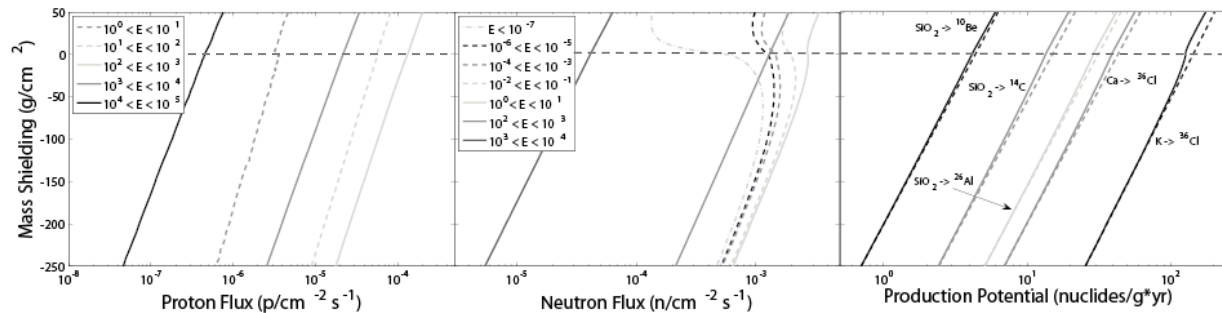modulation of 550 MV, high latitude and the US Standard Atmosphere.



Figure 2.3 – MCNPX simulation results of hadron fluxes and resulting production rates at upper surface of simple, homogeneous, granite planet.  A) Proton flux, binned by decadal energies, at atmosphere-granite boundary region. B) Select neutron flux binned by decadal energies, at atmosphere-granite boundary region.  C) Select production rates in select mineral phases.  Solid lines show total production rates predicted by folding MCNPX simulation particle results with excitation functions.  Dashed lines are exponential functions fitted to lower portion of production rate depth profile, showing the deviation of sub-surface production rates from a simple exponential.

Figure 2.3 shows the fluxes for protons and neutrons across the surface of the homogeneous

planet simulation for a typical granite composition.  Note the distinct difference in the boundary

effect between the neutron and proton fluxes.  Proton flux values barely respond to the boundary,

whereas there is a significant enhancement in the low to middle energy neutron fluxes (from

thermal energies up to ~50 MeV).  Because of this, and the fact that the threshold energies for

the reactions we are studying range from $10 - 50$ MeV, and that the neutron component tends to

dominate the nuclide production, *in-situ* production rates decrease with depth in a non-

24

exponential manner as shown in Figure 2.4.  Furthermore, the magnitude of the deviation from

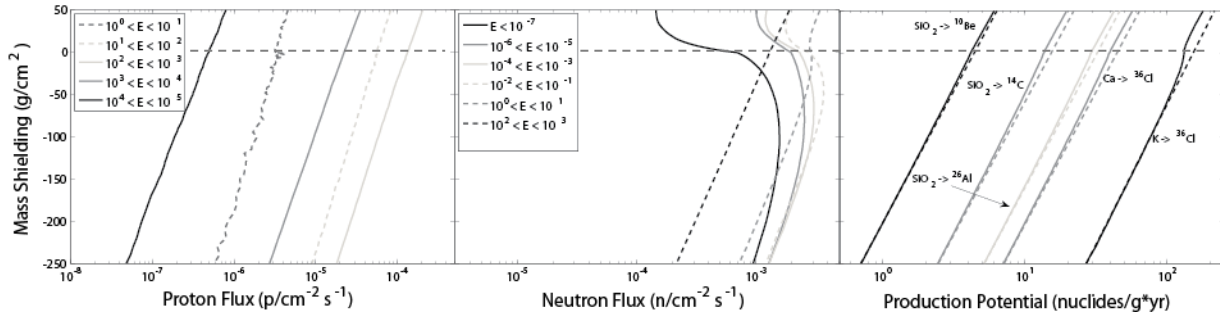the exponential decrease is nuclide dependent.



Figure 2.4 – MCNPX simulation results of hadron fluxes and resulting production rates at upper surface of simple, homogeneous, basalt planet.  A) Proton flux, binned by decadal energies, at atmosphere-basalt boundary region.  B) Select neutron flux binned by decadal energies, at atmosphere-basalt boundary region.  C) Select production rates in select mineral phases.  Solid lines show total production rates predicted by folding MCNPX simulation particle results with excitation functions.  Dashed lines are exponential functions fitted to lower portion of production rate depth profile, showing the deviation of sub-surface production rates from a simple exponential.

Figures 2.4 shows similar flux plots for a homogeneous planet made of basalt based on a Mauna

Loa basalt flow.  They are similar to those for granite; the proton fluxes show little change when

transitioning to the basalt, whereas the neutrons show an enhancement at low to mid energies.

The depth profiles of the production rates show similar, but slightly larger, deviations from the

simple exponential production profile (Figure 2.4) as in granite.  The percentage that the surface

production rates deviate from an exponential fitted to the production profile below ~100 g/cm$^2$

are listed in Table 2.2.

| Production reaction | Granite | | | Basalt | | |
|---|---|---|---|---|---|---|
| | Simulated | Fitted exponential | Percent deviation from exponential | Simulated | Fitted exponential | Percent deviation from exponential |
| $SiO_2 \rightarrow {}^{10}Be$ | 4.12 | 4.35 | 5.3 | 4.16 | 4.40 | 5.5 |
| $SiO_2 \rightarrow {}^{14}C$ | 13.5 | 15.0 | 10.0 | 13.7 | 15.3 | 10.5 |
| $SiO_2 \rightarrow {}^{26}Al$ | 28.9 | 31.3 | 7.7 | 29.2 | 32.3 | 9.3 |
| $Ca \rightarrow {}^{36}Cl$ | 38.9 | 43.0 | 9.5 | 39.3 | 44.3 | 11.3 |
| $K \rightarrow {}^{36}Cl$ | 127 | 144 | 11.8 | 132 | 152 | 13.8 |

Table 2.2 – Surface production rates in simple planet simulations.

## DISCUSSION

Simulation results of a deep atmosphere show changing attenuation lengths with depth, as well as slightly different attenuation lengths for each nuclide as shown in Figure 2.5. Furthermore, these values separate from each other with increasing altitude. Because nuclide production rates scale at different rates with altitude, the production ratio will change with altitude. By
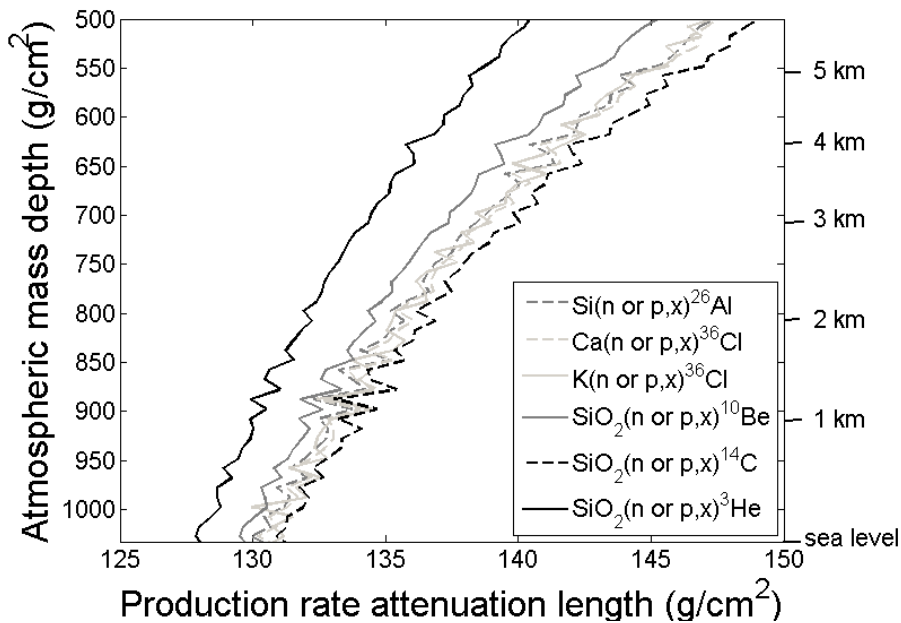


Figure 2.5 – Attenuation lengths for $^{26}$Al, $^{10}$Be, $^{14}$C and $^3$He from silica (SiO$_2$), and $^{36}$Cl from calcium and potassium in deep atmosphere simulation.

normalizing the ratio values to sea level, we find that the production ratios of most nuclides relative to $^{10}$Be decrease as a function of altitude with the exception of $^3$He (Figure 2.6). This result is similar to the conclusions of Gayer et al. 2004 [12] and Amidon et al. 2008 [11], although our results are smaller in magnitude. Our calculations are based on quartz at high latitude, whereas the measurements in both Gayer et al. [12] and Amidon et al. [11] were made on garnet at lower latitude, so a direct comparison cannot be made. By contrast,

Schimmelpfennig et al. 2011 [10] shows little to no altitude dependence, in their Kilimanjaro (equatorial) $^{36}Cl/^{3}He$ dataset measured in pyroxene and olivine.



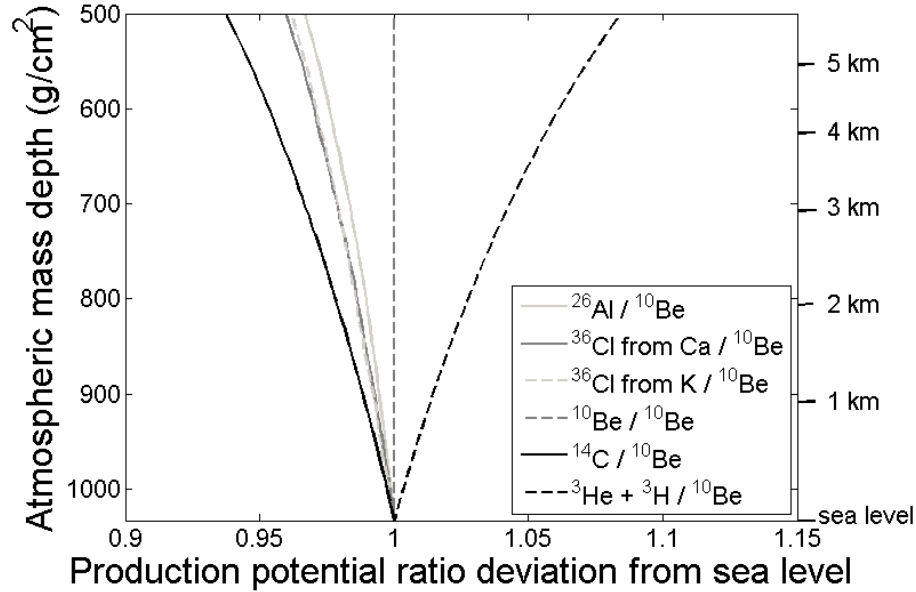Figure 2.6 – Ratios of various nuclide production rates to $^{10}Be$ production rate as functions of altitude, all normalized to sea level values.

The $^{26}Al /^{10}Be$ concentration ratio in quartz is often used to measure burial ages [27]. Our $^{26}Al/^{10}Be$ production rate ratio can be compared with measurements, as the CRONUS collaborative project has generated a substantial data set of both $^{26}Al$ and $^{10}Be$ measurements on calibration samples from high and low altitudes. While these data scatter at low $^{26}Al$ concentrations, the altitude dependent $^{26}Al/^{10}Be$ production rate ratio predicted by our model agrees reasonably well with the data (Figure 2.7) [28] with a reduced $\chi^2$ fit of 1.8. The present estimate of the $^{26}Al/^{10}Be$ ratio in quartz is 6.7 [29] after correction to revised values of the KNSTD $^{10}Be$ AMS standard series [30]. Our model predicts a ratio of 7.0 at sea-level and a value of 6.9 at 3000 m. The altitude dependence of the $^{26}Al/^{10}Be$ production rate ratio may also vary with latitude; however this study only investigates high latitude.
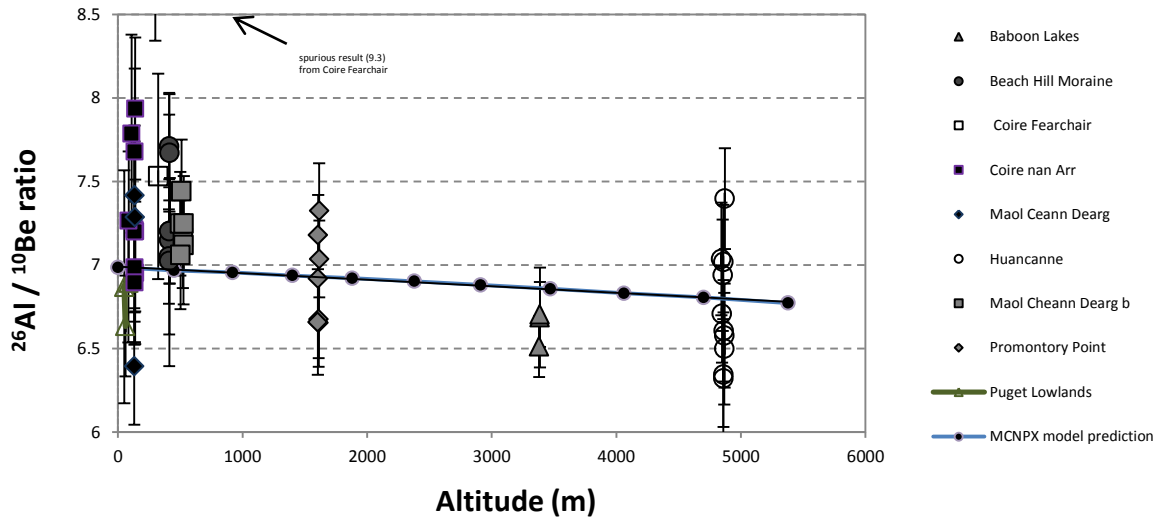
Figure 2.7 – Calibration data for the measured $^{26}$Al/$^{10}$Be ratio from CRONUS project and our model prediction.

## CONCLUSION

We present preliminary results of a physics-based model of the atmospheric cosmic ray flux, with the aim of better understanding the fundamental behavior of the radiation cascade. Beginning with a primary radiation of protons and alpha particles, we track the resulting radiation propagation through the atmosphere and into rock surfaces. We find that: (1) Nuclide production rates scale with altitude at slightly different rates unique to each nuclide. (2) Production rate attenuation lengths increase with increasing altitude. We attribute this to the continuing evolution of the radiation field in combination with the different sensitivity of each nuclide's excitation function to different ranges of neutron and proton energy.

We have also modeled granite and basalt, and found that the production rate depth profiles decrease in a manner that deviates from the expected exponential decrease. This effect is

greater in the basalt than granite, probably due to its higher mean atomic weight.  This

phenomenon will have an effect on calculated exposure age and estimates of slow erosion rates.

We believe that utilizing modern physics-based radiation transport codes in conjunction with

measured reaction cross sections will provide a better understanding the characteristics of the

radiation cascade and how those characteristics affect cosmogenic nuclide production rates.  Use

of these models will allow us to refine scaling models and better understand the rich data set of

sample and calibration measurements that have been made to date.

# REFERENCES

[1] D.E. Granger, P. Muzikar, Dating sediment burial with in situ-produced cosmogenic nuclides: theory, techniques, and limitations, Earth and Planetary Science Letters, 188 (2001) 269-281.

[2] G. Balco, C.W. Rovey II, AN ISOCHRON METHOD FOR COSMOGENIC-NUCLIDE DATING OF BURIED SOILS AND SEDIMENTS, American Journal of Science, 308 (2008) 1083-1114.

[3] J. Stone, Air pressure and cosmogenic isotope production, Journal of Geophysical Research, 105 (2000) 23,753-723,759.

[4] T.J. Dunai, Infuence of secular variation of the geomagnetic field on production rates of in situ produced cosmogenic nuclides, Earth and Planetary Science Letters, 193 (2001) 197-212.

[5] D. Desilets, M.G. Zreda, Spatial and temporal distribution of secondary cosmic-ray nucleon intensities and applications to in situ cosmogenic dating, Earth and Planetary Science Letters, 206 (2003) 21-42.

[6] N.A. Lifton, D.F. Smart, M.A. Shea, Scaling time-integrated in situ cosmogenic nuclide production rates using a continuous geomagnetic model, Earth and Planetary Science Letters, 268 (2008) 190-201.

[7] D. Lal, Cosmic-ray labeling of erosion surfaces: in situ nuclide production rates and erosion models, Earth and Planetary Science Letters, 104 (1991) 424-439.

[8] J. Gosse, F. Phillips, Terrestrial in situ cosmogenic nuclides: theory and application, Quaternary Science Reviews, 20 (2001) 1475-1560.

[9] T.J. Dunai, Reply to comment on `Scaling factors for production rates of in situ produced cosmogenic nuclides: a critical reevaluation' by Darin Desilets, Marek Zreda and Nathaniel Lifton, Earth and Planetary Science Letters, 188 (2001) 289-298.

[10] I. Schimmelpfennig, A. Williams, R. Pik, P. Burnard, S. Niederman, R. Finkel, B. Schneider, L. Benedetti, Inter-comparison of cosmogenic in-situ 3He, 21Ne and 36Cl at low latitude along an altitude transect on the SE slope of Kilimanjaro volcano (3S, Tanzania), Quaternary Geochronology, 6 (2011) 425-436.

[11] W.H. Amidon, K.A. Farley, D.W. Burbank, B. Pratt-Sitaula, Anomalous cosmogenic 3He production and elevation scaling in the high Himalaya, Earth and Planetary Science Letters, 265 (2008) 287-301.

[12] E. Gayer, R. Pik, J. Lave, C. France-Lanourd, D.L. Bourles, B. Marty, Cosmogenic 3He in Himalayan garnets indicating an altitude dependence of the 3He/10Be production ratio, Earth and Planetary Science Letters, 229 (2004) 91-104.

[13] T. Sato, H. Yasuda, K. Niita, A. Endo, L. Sihver, Development of PARMA: PHITS-based Analytical Radiation Model in the Atmonsphere, Radiation Research, 170 (2008) 244-259.

[14] P. Goldhagen, M. Reginatto, T. Kniss, J.W. Wilson, R.C. Singleterry, I.W. Jones, W. Van Steveninck, Measurement ofthe energy spectrum of cosmic-ray induced neutrons aboard an ER-2 high-altitude airplane, Nuclear Instruments and Methods A, 476 (2002) 42-51.

[15] M. Kowatari, K. Nagaoka, S. Satoh, Y. Ohta, J. Abukawa, S. Tachimori, T. Nakamura, Evaluation of the Altitude Variation of the Cosmic-ray Induced Environmental Neutrons in the Mt. Fuji Area, Journal of Nuclear Science and Technology, 42 (2005) 495-502.

[16] R.J. Sheu, S. Jiang, COSMIC-RAY-INDUCED NEUTRON SPECTRA AND EFFECTIVE DOSE RATES NEAR AIR/GROUND AND AIR/WATER INTERFACES IN TAIWAN, Health Physics, 84 (2003) 92-99.

[17] K. Nishiizumi, K.C. Welten, H. Matsumura, M. Caffee, K. Ninomiya, T. Omoto, R. Nakagaki, T. Shima, N. Takahashi, S. Sekimoto, H. Yashima, S. Shibata, K. Bajo, K. Nagao, N. Kinoshita, M. Imamura, J. Sisterson, A. Shinohara, Measurements of high-energy neutron cross sections for accurate cosmogenic nuclide production rates, Geochimica et Cosmochimica Acta, 73 (2009) A945.

[18] M. Dubin, A.R. Hull, K.S.W. Champion, US Standard Atmosphere, 1976, (1976) 241.

[19] G. Castagnoli, D. Lal, SOLAR MODULATION EFFECTS IN TERRESTRAIL PRODUCTION OF CARBON-14, Radiocarbon, 22 (1980) 133-158.

[20] G.W. McKinney, D.J. Lawrence, T.H. Prettyman, R.C. Elphic, W.C. Feldman, J.J. Hagerty, MCNPX benchmark for cosmic ray interactions with the Moon, Journal of Geophysical Research, 111 (2006) 1-14.

[21] R.C. Reedy, Nuclide Production by Primary Cosmic-Ray Protons, Journal of Geophysical Research, 92 (1987) E697-E702.

[22] J. Masarik, R.C. Reedy, Terrestrial cosmogenic-nuclide production systematics calculated from numerical simulations, Earth and Planetary Science Letters, 136 (1995) 381-395.

[23] T. Sato, K. Niita, Analytical Functions to Predict Cosmic-Ray Neutron Spectra in the Atmosphere, Radiation Research, 166 (2006) 544-555.

[24] R.C. Reedy, Cosmogenic-Nuclide production rates: reaction cross section update, Nuclear Instruments and Methods B, 294 (2013) 470-474.

[25] I.G. Usoskin, K. Alanko-Huotari, G.A. Kovaltsov, K. Mursula, Heliospheric modulation of cosmic rays: Monthly reconstruction for 1951-2004, Journal of Geophysical Research, 110 (2005).

[26] G. Balco, J.O.H. Stone, N.A. Lifton, T.J. Dunai, A complete and easily accessible means of calculating surface exposure ages or erosion rates from 10Be and 26Al measurements, Quaternary Geochronology, 3 (2008) 174-795.

[27] G. Balco, J. Stone, C. Jennings, DATING PLIO-PLEISTOCENE GLACIAL SEDIMENTS USING THE COSMIC-RAY-PRODUCED RADIONUCLIDES Be-10 and Al-26, American Journal of Science, 305 (2005) 1-41.

[28] Unpublished CRONUS-Earth data

[29] K. Nishiizumi, E.L. Winterer, C.P. Kohl, J. Klein, R. Middleton, D. Lal, J.R. Arnold, Cosmic Ray Production Rates of 10Be and 26Al in Quartz from Glacially polished Rocks, Journal of Geophysical Research, 94 (1989) 17,907-917,915.

[30] K. Nishiizumi, M. Imamura, M. Caffee, J.R. Southon, R.C. Finkel, J. McAninch, Absolute calibration of 10Be AMS standards, Nuclear Instruments and Methods B, 258 (2007) 403-413.

Chapter 3

A physics-based system for determining cosmic-ray produced nuclide

production rates

## ABSTRACT

This chapter presents the comprehensive, nuclear-physics-based cosmogenic nuclide production rate model combining radiation transport modeling with excitation functions for commonly measured nuclides. This model allows investigation of factors influencing nuclide production such as energy spectrum and angular distribution of the incident radiation which cannot be easily isolated in calibration measurements on natural samples. Neutron and proton fluxes over a range of atmospheric depths and cut-off rigidities and production rates for $^3$He, $^{10}$Be, $^{14}$C, $^{21}$Ne, $^{26}$Al, and $^{36}$Cl based on these fluxes are presented. The model predicts that production rates for these nuclides diverge from one another with altitude, hence that production ratios change with altitude. Model results for particle flux, production rates, production rate attenuation lengths, and production ratios are discussed. Production rates scale in altitude with increasing attenuation lengths which are unique to each nuclide. This causes production ratios to change with altitude.

34

# INTRODUCTION

Over the past two decades, cosmogenic-nuclide geochemistry has become widely used with broad applications in surface exposure dating (Lal, 1988a), erosion-rate measurement (Lal, 1991), burial dating of clastic sediments (Balco et al., 2005), and sediment tracer studies (Bierman and Steig, 1996). Recently, studies investigating asynchrony in glacial advance and retreat have employed high-precision cosmogenic nuclide measurements (Schaefer et al., 2009). At present, all these applications rely on empirical calibrations of nuclide production rates that are based on only a small number of sites where independently dated geologic events have produced surfaces suitable for cosmogenic nuclide exposure dating. The sparseness of calibrations sites and inherent analytic uncertainties in this data set, so far, preclude rigorous validation of the geographic and temporal production rate scaling schemes that are necessary to both predict production rates at unknown-age sites and to determine whether different cosmogenic nuclides require different scaling. The latter is especially important for predicting nuclide production ratios that are required for multiple-nuclide applications such as burial dating (Balco and Rovey II, 2008; Balco and Stone, 2005; Erlanger et al., 2012). Two approaches are necessary to overcome these limitations: (1) continued efforts to identify high quality calibration sites and expand their coverage of altitude, geomagnetic latitude and exposure time, and (2) development of a well validated, first-principles understanding of the nuclear underpinnings of production rate variations. This work focuses on the latter.

As cosmogenic nuclide methods grow more sophisticated and demand shrinking systematic uncertainties, our understanding of the nuclide production systematics must advance. Calibration sampling has constrained the sea level high latitude (SLHL) production rate of $^{10}$Be

to ~ +/- 10% (Schimmelpfennig et al., 2012), but predicting the production rate globally continues to be a challenge because of the sparseness of reliable calibration material. Furthermore, analytic uncertainties and environmental factors may obscure subtle but important characteristics of the global production rate phenomena, as shown in Chapter 2 (Argento et al., 2013).

Determining the production rate at any point on the earth requires knowledge of how the radiation field changes with many factors, including altitude and latitude. Some scaling schemes have approached this via analogs such as photo-emulsion studies (Lal, 1991; Stone, 2000) or utilizing neutron monitor records (Desilets and Zreda, 2003; Dunai, 2001; Lifton et al., 2008). Neutron monitor based scaling schemes were considered a critical improvement because of their dense data set and because neutron monitor events are initiated by a similar range of cosmic-ray particles and energies to those that produce cosmogenic nuclides. However, these scaling schemes have not succeeded in predicting the calibration sample concentrations better than the original scaling scheme of Lal (1991). It is therefore essential to continue building our understandings of the radiation cascade and resulting production of cosmogenic nuclides through the use of physics based models (Argento et al., 2013). The purpose of this research is to develop a purely physics based model which allows us to simulate all of the processes in cosmogenic nuclide production separately, in contrast to natural sample calibration in which they are superimposed. With this model, we have generated global production rates for all nuclides, at all altitudes, at all latitudes, explored the effect of changing the GCR profile on sea level production rates, and validated the model against a number of measurements. All production rate

results presented in this work are strictly for the spallogenic component. Muons are not considered here.

Several improvements and enhancements have been made to the model since the preliminary results were published (Argento et al., 2013). Most importantly, we optimized the high energy physics settings for MCNPX and normalization calculations. In this work, we present a detailed description of the radiation transport settings, the methods to calculate production rates from the radiation transport results, and efforts to benchmark the system.

## METHODS

Our model has three essential components: i) the primary galactic cosmic ray (GCR) source radiation, ii) radiation transport using MCNPX (Monte Carlo N-Particle eXtended) and resulting tallies for various particles, and iii) cross sections for nuclide production, which are folded the particle spectra to predict nuclide production rate. The model is modular in its use of the components, making it possible to substitute other options of each component to determine effects on the final cosmogenic nuclide production results.

### GCR models

This work focuses on production from galactic cosmic-rays. We primarily use the GCR model as described in (McKinney et al., 2006). We have also investigated the differences in sea level high latitude production rates (SLHL) using primary spectra from (Usoskin and Kovaltsov, 2006). Figures 3.1a and 3.1b show the model predictions for protons and alpha particles for these GCR models. The McKinney model is based on the model originally developed by

(Castagnoli and Lal, 1980) and (Lal, 1988b), with revision to the parameters. These two models were based on (Urch and Gleeson, 1972) and (Garcia-Munoz et al., 1975). McKinney 2006 used the South Pole neutron monitor records as well as the Apollo 17 Lunar Neutron Probe Experiment (LNPE) for calibration. The Usoskin and Kovaltsov (2006) model is based on the GCR model developed by (Burger et al., 2000), and calibrated by comparison with extensive atmospheric ionization measurements.

The two models predict similar energy spectra with the greatest differences in particle flux below ~3 GeV. Cosmic-ray particles with energies lower than 3 GeV do not have enough penetrating power to account for substantial sea level production. However, given their substantial flux at the top of the atmosphere, they contribute increasingly to the total production rates at higher altitudes.
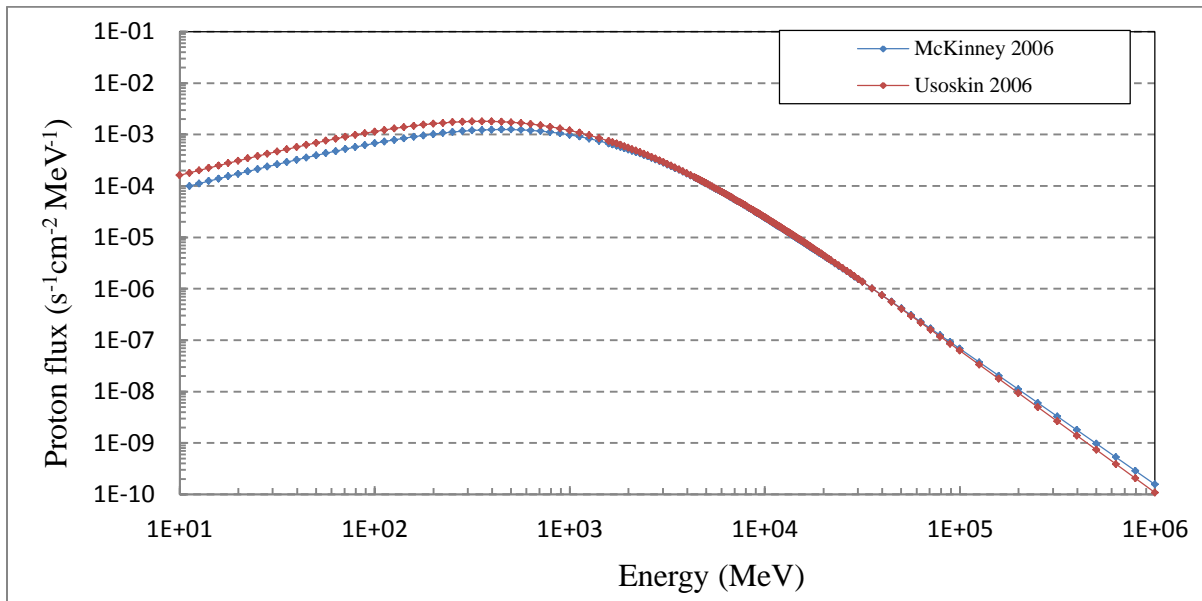


Figure 3.1a – GCR model proton spectra from McKinney 2006 and Usoskin 2006 at 550 MV solar modulation. Models show close agreement in the region above 3 GeV, but diverge at lower energies. These lower energy particles don't penetrate the entire atmosphere effectively, but can have an effect on production rates at very high altitude, and especially on meteoric production.
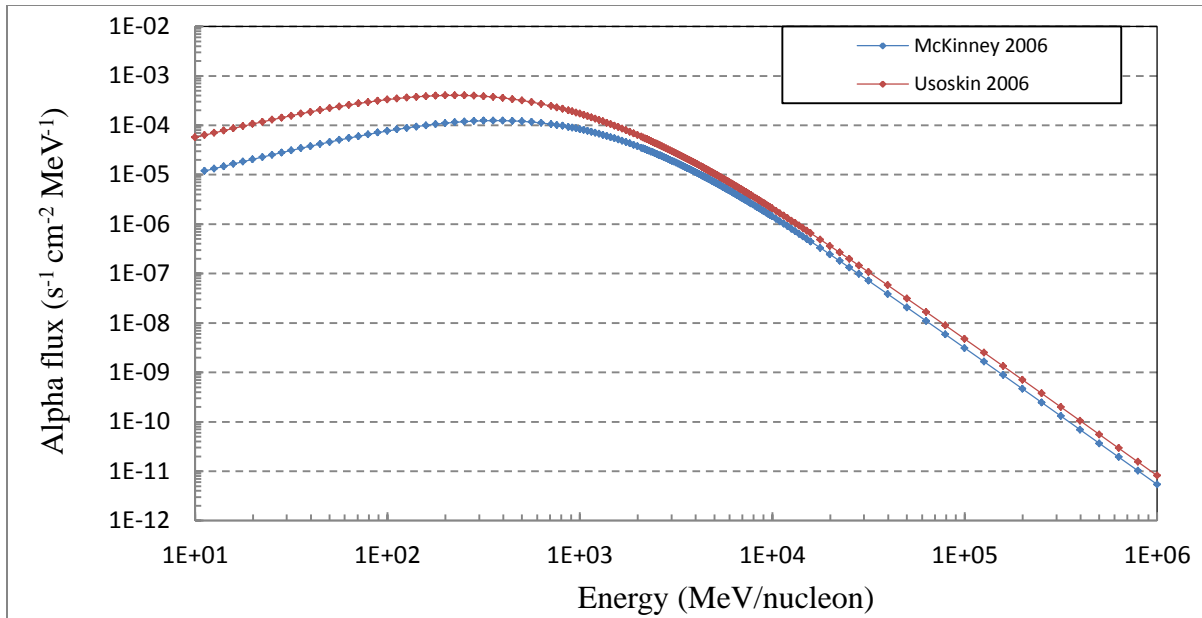
Figure 3.1b – GCR model alpha particle spectra from McKinney 2006 and Usoskin 2006 at 550 MV solar modulation. The GCR models differ in magnitude at all energies, but most dramatically below 4 GeV.

The GCR flux models all utilize a power law of ~ -2.7 derived from diffusive acceleration theory of charged particles in supernovae. They differ somewhat on how the solar modulation is treated, resulting in moderate differences in lower energy particle flux predictions. The models also differ in how they predict the proton / alpha flux ratios. Usoskin and Kovaltsov (2006) considers everything in the GCR flux heavier than protons to be effectively alpha particles because the proton to neutron ratio is roughly the same, thus imparting roughly the same magnetic rigidity characteristics. McKinney et al., 2006 only considers the alpha particles themselves which is the likely source of the discrepancy between the two model predictions.

All of these models account for solar modulation of the GCR flux at Earth's orbit. Most studies in the past indicate a long term average solar modulation around 550 MV (Masarik and Reedy, 1995; Reedy, 1987). There is some debate about what this value should be with values between 480 – 650 MV being suggested (Leya and Masarik, 2009; Masarik and Beer, 2009; Steinhilber et

al., 2008). In keeping with earlier models, we use a value in the middle of this range, 550 MV

for our terrestrial production rate results. For benchmark comparisons with Goldhagen's neutron

spectrum measurements, we use 400 MV (Goldhagen et al., 2004; Goldhagen et al., 2003;

Goldhagen et al., 2002; Gordon et al., 2005; McKinney et al., 2012).


It should be noted that particles originating from the sun are generally too low in energy to affect

*in-situ* production rates. On rare occasions coronal mass ejections (CMEs) generate particles in

the energy ranges that can affect production rates in the upper atmospheres. However, it has

been shown that these events are too brief to substantially contribute to the long-term average

inventories (Usoskin et al., 2006).


**Radiation transport**

MCNPX is a general purpose, relativistic, Monte Carlo style radiation transport code. The code

has the capability to transport 34 different sub-atomic particles as well as light ion recoil

fragments, continuously from low energy to 1 TeV (James et al., 2006). MCNPX evolved from

the low energy transport code, MCNP, developed at Los Alamos National Laboratory. Both

variants are widely regarded as leaders in handling neutrons from very low to mid-energies.

MCNPX has extended high energy capability allowing the use of one single, coherent simulation

for all particles for all energies, rather than using a high energy package such as LAHET, and

transferring the results to a low energy transport code, such as MCNP (Goldhagen et al., 2002;

Masarik and Beer, 2009; Masarik and Reedy, 1995). For this study, we use MCNPX 2.7.

The GCR source radiation we specify spans five orders of magnitude in energy (10 MeV/nucleon

to 1 TeV/nucleon). The modeled atmosphere is composed of nine elemental species and 32

isotopic species. High energy reactions give rise to secondary particles such as free neutrons,

muons, pions, kaons, and various combinations of nucleons (alpha particles, etc.), each of which has characteristic scattering, absorption and reaction probabilities. Each projectile particle-isotope combination has its own unique range of potential reactions, and every one of those reactions is energy dependent.

Monte Carlo style codes rely on stochastic input to simulate complex systems such as these. Some inputs are user defined such as source radiation parameters, geometry, and physics options; and MCNPX controls the other parameters such as reaction cross sections, particle mean free path, and particle decay time. MCNPX will track individual particles until the particle terminates via decay, absorption or a user determined cut-off (energy, time, etc.). For each step, MCNPX generates a random number to sample the pertinent probability density function: (i) particle type, particle energy, particle angle; (ii) distance to interaction; (iii) target nucleus or ionization; and (iv) reaction type: (a) scatter, (b) particle absorption, or (c) new particle generation.

Assigning reaction cross section tables is an important aspect of user-defined input in MCNPX. Tables are where the considerable amount of evaluated cross section data resides. Careful selection of which isotopes are defined is critical to achieving accurate results. If the assigned isotope is not contained in the table library, MCNPX will default to model treatment. In the case of mid to low energy neutrons, this can result in incorrect results. A common mistake is to use the natural abundance identifier (ZAID: zz000) when the table may not exist. In this model, we use individual isotopic identifiers rather than natural abundance identifiers when available.

The statistical nature of MCNPX makes Monte Carlo style codes very computationally intensive. Simulations often take several days and in some cases several weeks to achieve convergent solutions on modern workstation class computers.

**Application of angular rigidity cut-offs**

While the above descriptions of the GCR radiation suffice for high latitude studies (greater than ~60° geomagnetic latitude), the modifications to these fluxes due to the earth's geomagnetic field must be considered for studies of lower latitudes. Modification of the GCR flux is weakest at the poles where the charged cosmic-ray particles are traveling very close to parallel to the earth's magnetic field lines. Modification increases towards the equator where incoming particles are traveling closer to perpendicular to the field lines. The removal of the particles from the incoming flux is quantified by the cut-off rigidity term. In this work, we use vertical cut-off ($R_c$) to organize our results.

Rigidity cut-offs have been calculated as a function of azimuth and zenith at many points on the earth for these studies (O'Brien, 2008). These calculations are then applied to the surface source at the top of the atmosphere by segmenting the $2\pi$ solid-angle space into regions corresponding to the azimuth and zenith coordinates (Figure 3.2). Each angular coordinate is assigned a solid angle weight. After modifying the spectrum and total particle flux for each coordinate window, all azimuth windows for a given zenith value are then summed. The resulting spectrum is now a function of zenith only as MCNPX cannot specify a surface source with a distribution in azimuth.
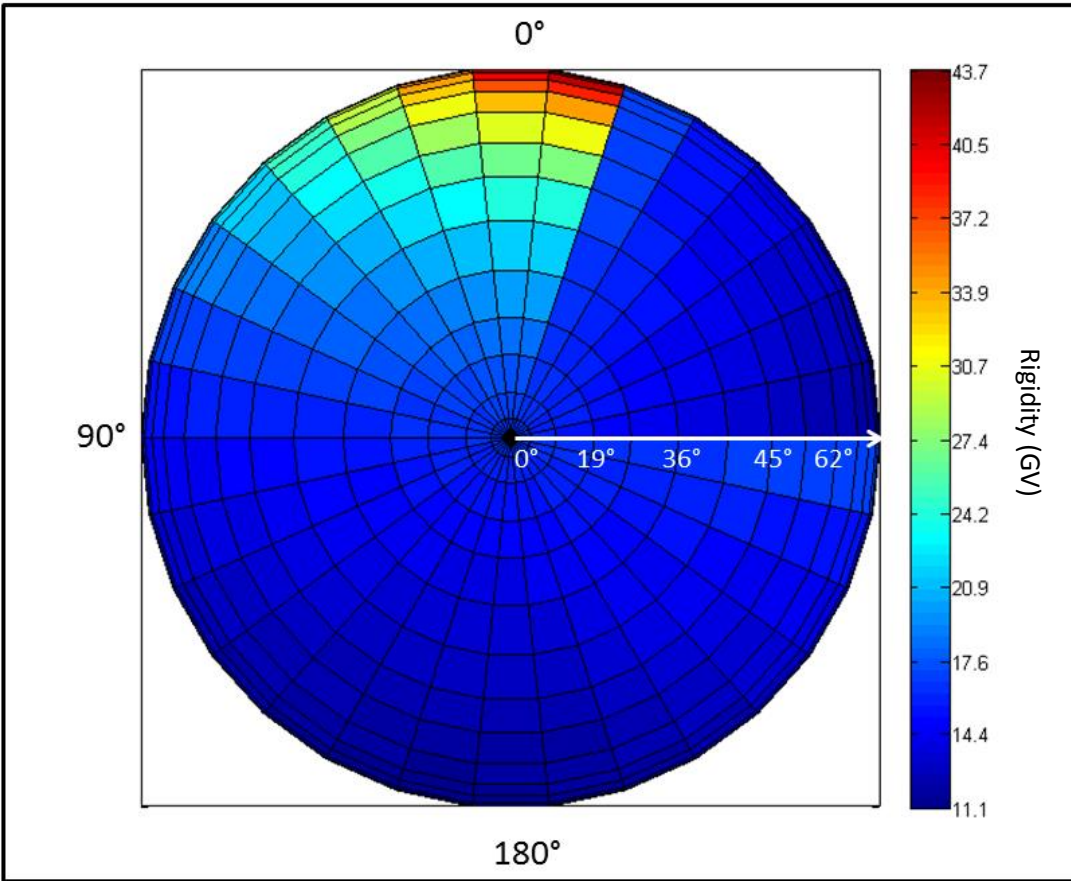
Figure 3.2 – Calculated rigidity in GV for 21N 100E in 2012 illustrating the variation in cut-off rigidity at different angles. 0° represents west. Vertical cut-off rigidity is 16.4 GV.

While these calculations are made for earth's current magnetic field structure, we assume that the second order effects of non-dipole structure are minor. The results are generalized to that of the calculated vertical cut-off at those coordinate points on the surface of the earth. Because the non-dipole features of the earth's magnetic field are transient and thought to average out over time, we would ideally be making cut-off calculations based on a pure dipole magnetic field to generate results that would be more generally applicable to past field reconstructions. This is a project that warrants future effort.

When utilizing cut-off rigidities, care must be taken to define the energy spectrum in sufficiently fine energy (or magnetic rigidity) bins such that the steps are not overly large in the region where the cut-offs are being applied. Neglecting this detail can result in an overly granular resolution in cut-off, resulting in poor reproduction of the radiation spectrum predicted by the geomagnetic angular cut-off models. For this work, steps in rigidity in the region below 20 GV were no wider than 200 MV and in most cases were considerably smaller than this.

**Normalizations**

$2\pi$ - Sources in this MCNPX model are specified as $2\pi$, so the values obtained from the GCR models ($4\pi$) must be divided by 2.

Tally results - MCNPX reports its results as flux per $cm^2$ (area of the tally surface) per source particle. Flux results must be multiplied by the integral particle density of the source (particles $cm^{-2}$ $s^{-1}$) as well as the surface area of the source surface. This is a simple process when evaluating the particle density of an un-modulated GCR source. Evaluating this term for a GCR source which has had angular cut-offs applied becomes more complex because the particle flux must be determined for each defined solid angle "window" (as described above).

Current to flux - MCNPX specifies its source as current, whereas GCR models are specified in flux. Current is defined by MCNPX as particles per $cm^2$ (I), whereas flux is defined as $I/\cos(\theta)$ where $\theta$ is the angle from normal. Thus, a corrective normalization must be made to account for this. For a simple, isotropic source, the normalization is simply a factor of ½ (McKinney et al., 2006). However, since the geo-magnetically modified source is no longer strictly isotropic, a

normalizing factor is also calculated for each GCR source at each coordinate. These values

rarely differ from the value of ½ by more than five percent.


**Model geometry**

The geometry of these simulations is made up of concentric spherical shells. Radiation is

propagated through an entire atmosphere (1033 g/cm$^2$) starting 100 km above the surface of the

earth. The atmospheric structure is based on the Standard US Atmosphere (1976) (Dubin et al.,

1976), with the source radiation emitting at the top of the geometry from the spherical surface.

Above 100 km, the atmosphere is extremely diffuse and the composition also changes. While

the bulk of the initial reactions don't start until ~ 20 km altitude, a full spatial extent to the

atmosphere is important for MCNPX to properly simulate the relativistic decay of short lived

particles. The earth surface radius for sea level simulations is defined to be 6371 km. The

atmosphere is modeled with >100 concentric spherical shells depending on the application and

needed resolution.


Boundary effects in the radiation energy spectrums are of great interest in this work. For this

reason, we use shells that are thin in mass depth near a material boundary to capture increased

resolution near these boundaries. This does not apply to the artificially deep atmosphere

simulations where we intentionally avoid boundary effects.


Deep Atmosphere

We developed the artificially deep atmosphere to investigate radiation cascade characteristics

without any biasing effects of different material. The geometry utilizes 180 shells of air above a

core of water.  The atmosphere is constructed to be roughly 1.5 atmospheres in mass with the air

getting denser below modern sea level (1033 $g/cm^2$) at the standard lapse rate in the troposphere.

The material of the core is irrelevant, as it is simply there to block particles from passing through

the entire planet.  This is ensured by using zero importance parameter in this region (see

Importance Values below).

Knyahinya Meteorite

We modeled the Knyahinya meteorite to benchmark the performance of the GCR spectrums and

radiation transport in the uppermost energies.  The meteorite was modeled as 45 cm in radius

with density 3.35 $g/cm^2$ as prescribed by (Graf et al., 1990), using 45 concentric spherical shells

separated by 1 cm.  Elemental constituents were modeled after an L Chondrite with Al, Cr, Mn,

Fe and Co abundances provided in (Graf et al., 1990).

Beacon Heights Sandstone

The Beacon Heights sandstone of the Antarctic Dry Valleys is modeled for comparisons with

CRONUS calibration core measurements (Stone et al., in preparation).  We simulated the

sandstone as a homogenous quartz planet of 6,373,183.00 m radius (2,183 m elevation above sea

level) with 756 $g/cm^2$ air above (742 hPa) with density of 2.33 $g/cm^3$ and 12% void space filled

with dry air.  The long-term solar modulation value 550 MV was used.  No geomagnetic

modification was used on the GCR spectra.  Concentric spherical shell surfaces were used, with

tight spacing near the air-sandstone boundary (0.25 $g/cm^2$ and increasing as distance from

boundary increases).

**Importance values**

Without statistical method enhancements, Monte Carlo style numeric simulations are burdensomely slow. There are numerous statistical tools built into MCNPX (as well as other similar radiation transport codes) that allow the user to generate acceptable statistics throughout the desired spatial extent of the geometry. For this work, the most important of those tools is the use of "importance values" which dictate the use of particle Splitting or Russian Roulette (Pelowitz, 2011). Splitting and Russian Roulette are the statistical "games" which either split or kill a particle. In regions with splitting, the resulting particles score comparably lower in tallies. In regions with particle killing, the surviving particles score comparably higher in tallies. We have found that using the Weight Window Generator in MCNPX is not stable for a system involving so many particles spanning such a wide range of energies.

Using regions of zero importance to kill particles is important in two situations: 1) the region just outside the earth's atmosphere, and outside the source surface killing albedo particles that are leaving the system and should not be tracked anymore, and 2) in order to kill very deeply penetrating particles that can otherwise occupy inordinate amounts of computational power.

We use values of 1 from the top of the atmosphere until the particle density reaches a maximum (sometimes referred to as the Pfotzer maximum). Importance values are then increased with descending altitude with the goal of maintaining roughly the same particle population in each cell. A rough guide to assigning importance values is 1) dividing the mass depth, $d$ (g/cm$^2$), between surfaces (*i* and *i-1*) by the assumed attenuation length, $\lambda_j$ (g/cm$^2$), and then 2)

multiplying the prior importance by the factor of e raised to this calculated value:

$$I_{i,j} = I_{i-1,j} * e^{d/\lambda_j}$$

Eq 3.1

This procedure should be done individually for each particle type (*j*). For example, the attenuation length of muons is much longer than that of any hadronic particle. Determining appropriate importance values for all particles throughout the region of interest is an iterative process that involves several test run simulations and manual calculations. However, generating appropriate importance values will allow the simulation to achieve balanced statistics throughout the regions of concern, thus minimizing the computation time spent on regions with naturally higher flux. Used carefully, this method will allow the simulation to converge to a solution in all regions of interest in a much shorter period of time than if not used.

**MCNPX Physics options**

Modeling cosmic-ray radiation in any radiation transport code requires close attention to the physics options because of the wide range of energies. We list the settings used for this work, as recommended by (James et al., 2006; Mashnik, 2008) in Appendix A.

**MCNPX particle flux output tallies**

For this work, we use surface flux tallies. Careful choice of energy bins is critical to this work. While wider bins yield good statistics with less computation time, one must consider the resolution in the cross sections. Resonances which generate peaks in particle energy spectra will also be poorly resolved with overly wide bins.

**Atmospheric composition**

For this work, we use a dry atmosphere composed of:

| Molecule | % by volume |
|----------|-------------|
| N2 | 78.08 |
| O2 | 20.95 |
| Ar | 0.93 |
| CO2 | 0.038 |
| Ne | 0.0018 |
| He | 0.0005 |
| Kr | 0.0001 |
| H | 0.00005 |
| Xe | 8.70E-06 |

Table 3.1 – Composition of atmosphere in simulations

Water content in the atmosphere can vary considerably; however, it is typically concentrated near the surface and changes rapidly. Further studies will explore the effects of various water contents.

**Production rates: cross section folding**

To calculate cosmogenic nuclide production rates from the simulation results, energy dependent flux results at a given point in the geometry are convolved or "folded" with the energy dependent cross sections, also known as excitation functions (Reedy, 2013). In this manuscript, references to cross sections always imply energy dependence.

While cross sections are defined as functions of energy, MCNPX flux output comes in user defined bins (Figure 3.3). In order to convolve these energy dependent quantities, one must determine an average cross section value for each energy bin. The cross sections used in this work are meant to be interpolated in either lin-log or log-log space. Summing the entire range of energy bin production potentials yields the total production rate potential for that reaction in

atoms cm$^{-2}$ s$^{-1}$ target nucleus$^{-1}$ at that surface in the geometry.  For these spherical geometries, we tally across the entire spherical shell, effectively collapsing the results into the dimension atmospheric depth or altitude.
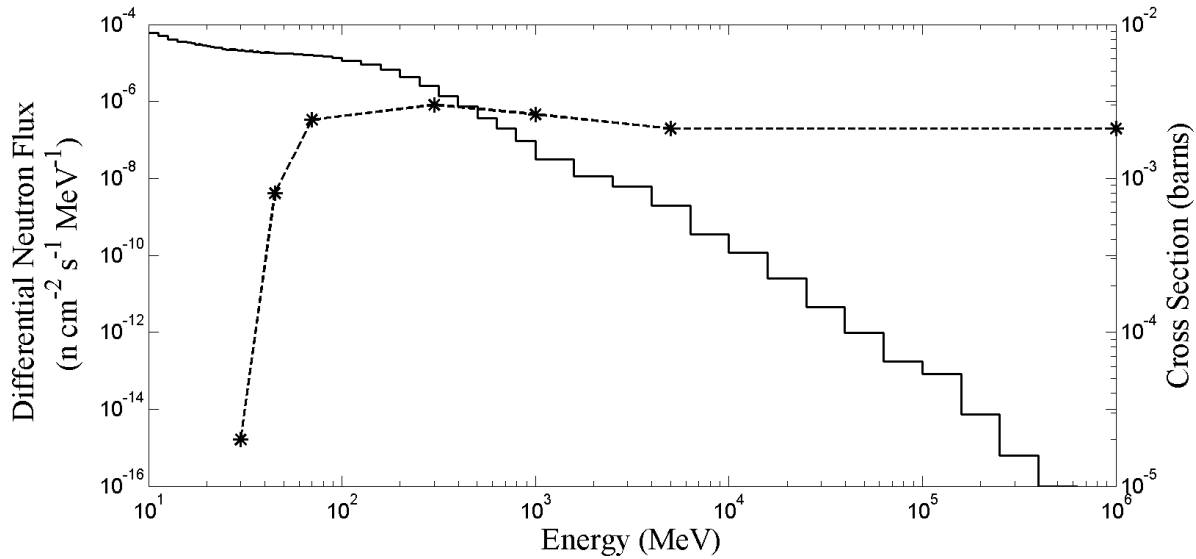


Figure 3.3 – An example of the differential neutron flux results at sea level aligned with the cross section for O(n,x)$^{10}$Be.  The absolute flux of neutrons in an energy bin, not the differential flux, is multiplied with the cross section value at that energy to generate a production rate.

# RESULTS

## Validations

Goldhagen

In this work, we focus on neutrons and protons flux because of their dominance in production of the nuclides of interest.  Of the two, neutrons are the most significant producers of the nuclides in question because of their greater overall flux in altitudes of interest.  However, unlike protons, their energy spectrum is difficult to measure (Carmichael and Bercovitch, 1969; Goldhagen et al., 2004; Goldhagen et al., 2002).  Thus there are relatively few benchmarks to use in assessing the accuracy of the simulated neutron spectrum.  Here we compare our results with the

measurements reported in (Goldhagen et al., 2002) and further analyzed in (Goldhagen et al., 2004) and (McKinney et al., 2012). The 2002 paper discusses the original experimental setup and calculations and (Goldhagen et al., 2004) discusses improved methods to calculate the unfolded neutron spectrum. (McKinney et al., 2012) includes updated calculations of the unfolded neutron spectrum as well as their latest efforts to reproduce the measurements through simulations without scaling. Figure 3.4, 3.5, 3.6 & 3.7 show our results in simulating the conditions using both the (McKinney et al., 2006) and (Usoskin and Kovaltsov, 2006) GCR models as primary radiation input. While these measurements are considered to be the benchmark for atmospheric neutron spectrum measurements, there are reasons to not scale simulation results to match them. The measurements were conducted within an aircraft, with the array of Bonner Sphere detectors all contained within sealed aluminum canisters, all adding to the complexity of interpreting the measurements into neutron flux. There have been several follow-up studies with revisions to the calculated spectrum, and this is an ongoing endeavor (McKinney et al., 2012). Because the onboard proton detector was accidentally disabled during the flight, corrections for protons and pions are entirely calculated. In addition to these potential sources of uncertainty, the uppermost measurements ($> 200$ g/cm$^2$) may be difficult to match in simulations such as these due to low energy re-entrant albedo protons being ejected and magnetically bent back to the Earth (Clem et al., 2004) and a potential for the lower energy portion of the proton spectrum to be influenced by the earth's magnetic field.
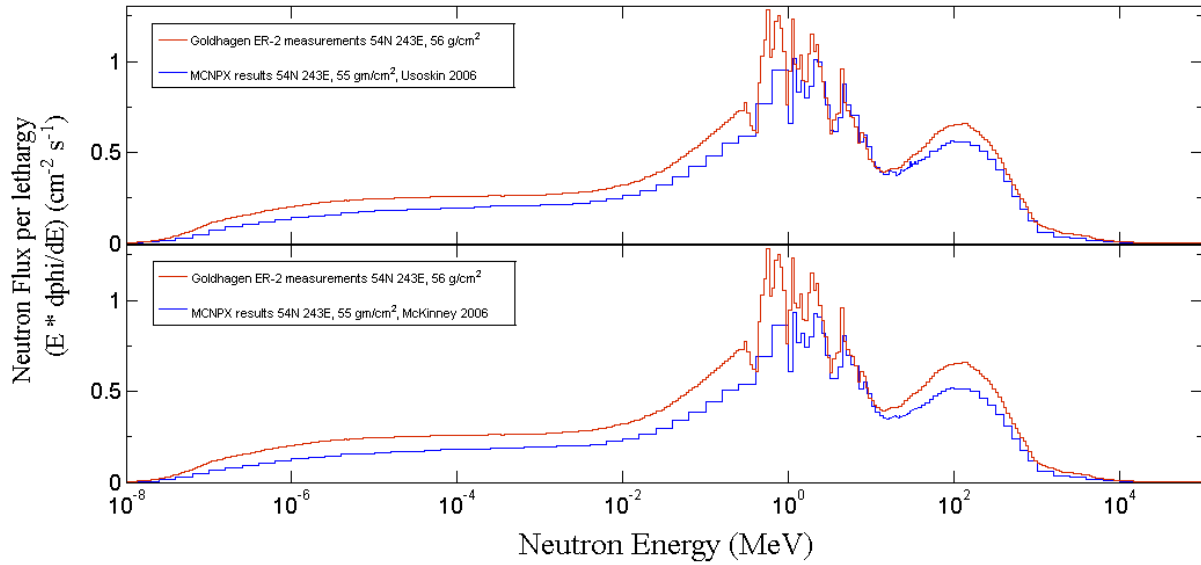
Figure 3.4 – Comparison of MCNPX results using Usoskin 2006 and McKinney 2006 GCR models at 54N 243E 55 g/cm$^2$ with Goldhagen 2004 measurement at 56 g/cm$^2$.  Usoskin 2006 performs better at reproducing this measurement.
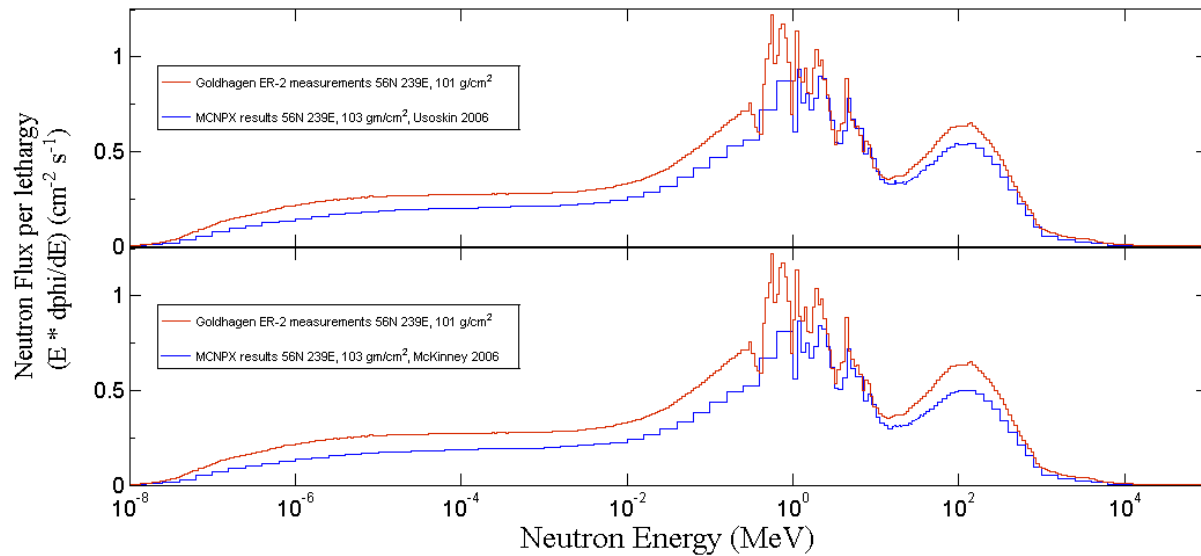


Figure 3.5 – Comparison of MCNPX results using McKinney 2006 at 56N 239E 103 g/cm$^2$ with Goldhagen 2004 measurement at 101 g/cm$^2$.  Again, the Usoskin GCR model reproduces the measurements most closely.
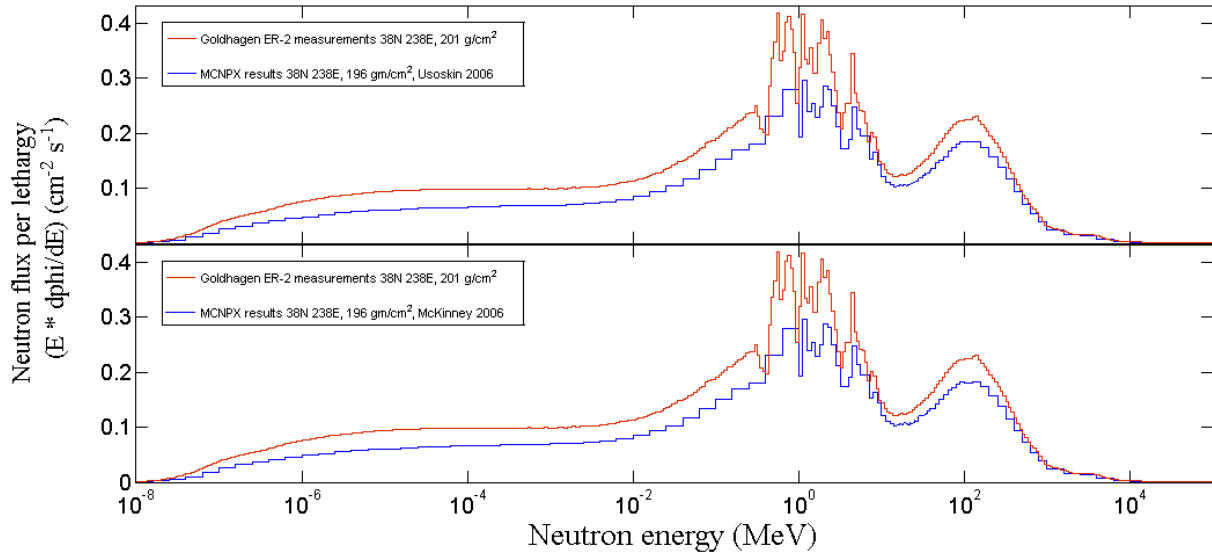
Figure 3.6 – Comparison of MCNPX results using McKinney 2006 at 38N 238E 203 g/cm$^2$ with Goldhagen 2004 measurement at 201 g/cm$^2$. At this altitude, the neutron flux produced by the Usoskin and McKinney GCR models are indistinguishable. Above ~1 GeV, the simulations reproduce the measurements well. Below ~1 GeV, the simulation results are low by 10 – 30%.
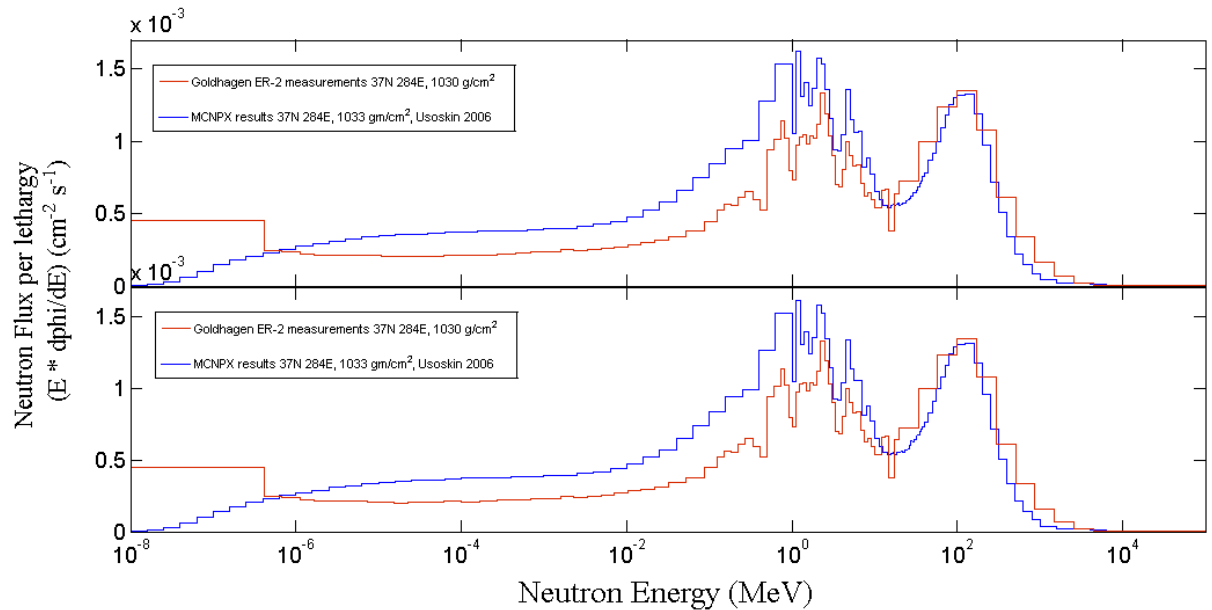


Figure 3.7 – Comparison of MCNPX results using McKinney 2006 and Usoskin 2006 at 37N 284E 1033 g/cm$^2$ with Goldhagen 2004 measurement at 1030 g/cm$^2$. Here, at energies at and above ~1 GeV, we have good agreement, however, at lower energies, our results are high by 10-40 %. This is likely explained by the absence of water bearing soil and concrete in our simulation. Similar to the 201 g/cm$^2$ comparisons, the results from the simulations using Usoskin 2006 and the McKinney 2006 are indistinguishable.

We have also developed a model of the Knyahinya stony meteorite which was analyzed

extensively in (Graf et al., 1990) and others. We use the same GCR sources to irradiate the LL5

chondrite to calculate the production rates and thus expected concentrations. This simulation is

used as a benchmark for the GCR spectra used on a small object with no atmosphere. For

unknown reasons we seem to consistently generate results that are lower than measured by (Graf
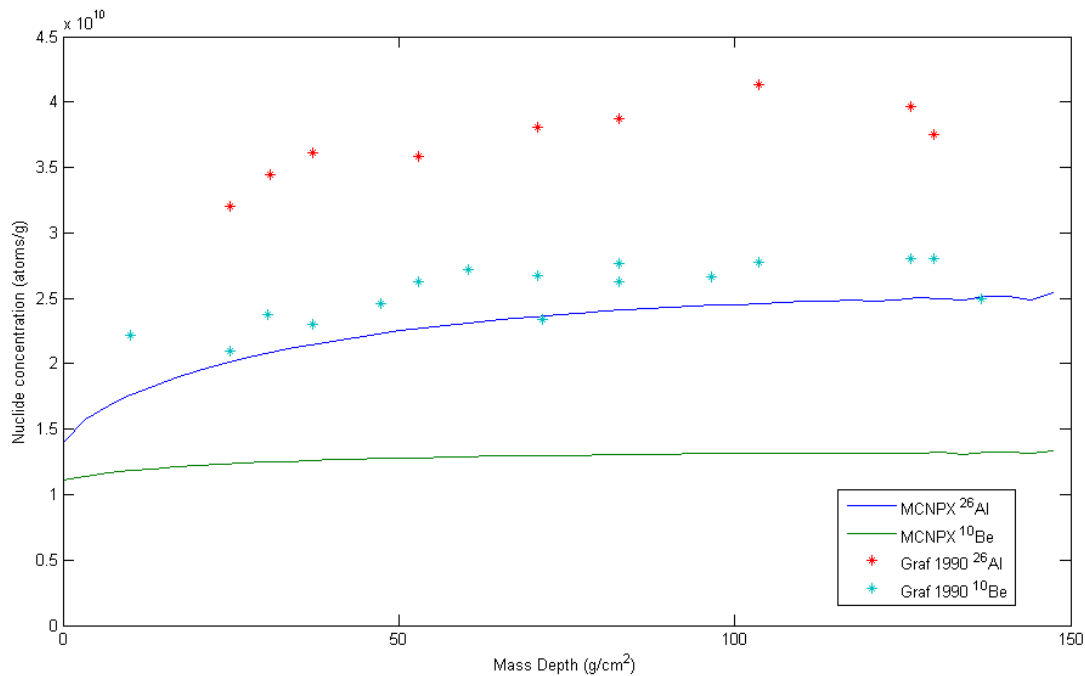
et al., 1990)(shown in Figure 3.8 & 3.9).



Figure 3.8 – Calculated and measured concentrations of $^{26}$Al and $^{10}$Be in Knyahinya meteorite. Calculated profiles are similar in shape but low in magnitude.
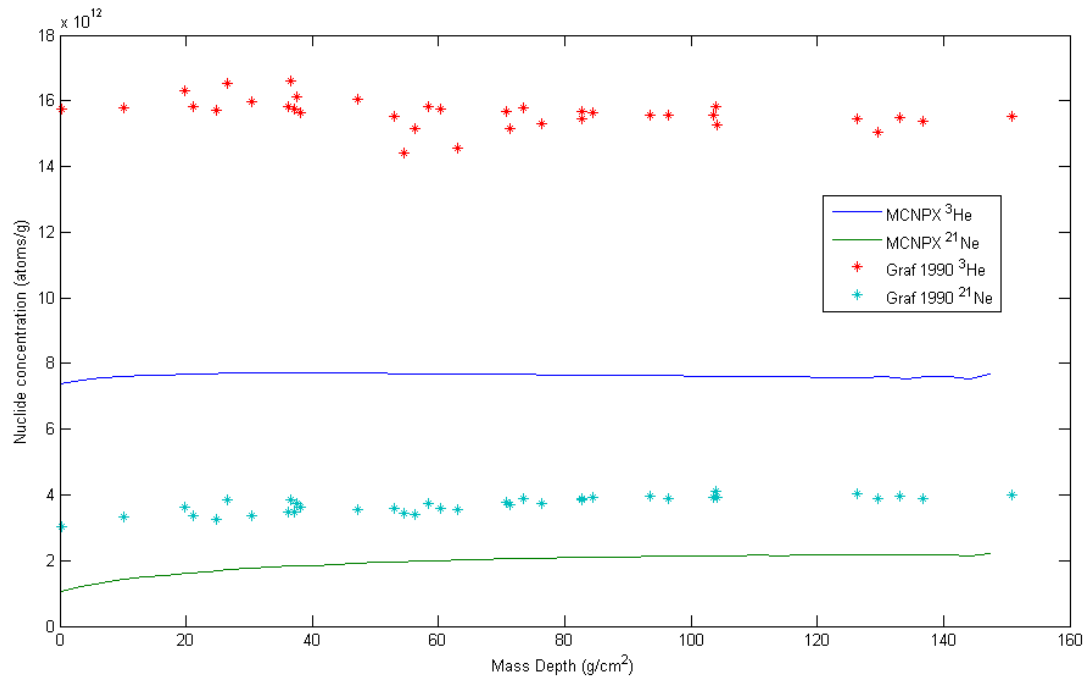
Figure 3.9 – Calculated and measured concentrations of $^3$He and $^{21}$Ne in Knyahinya. Again, the profiles are similar in shape while the magnitudes are low.

## Beacon Heights sandstone core

Simulation results for the Beacon Heights sandstone have a much better agreement with the measured data. Assuming 7.7 cm/Myr erosion, modeled surface concentrations come out ~25% high for $^{10}$Be and ~12% high for $^{26}$Al compared to measurements (Stone et al., in preparation). As shown in Figure 3.10, calculated subsurface production rates/concentrations for the two nuclides have very similar depth profiles to those measured with the exception of the nose over in the measured $^{26}$Al concentrations. We have found the production profile does not behave strictly as a simple exponential. The upper aspects of the profiles show a longer attenuation length than the deeper portion of the profile. The attenuation length for both nuclide concentration profiles settle at 138 g/cm$^2$ in the deeper portion. The upper portions of both profiles are shown in Figure 3.11 where they show substantially different attenuation length profiles.
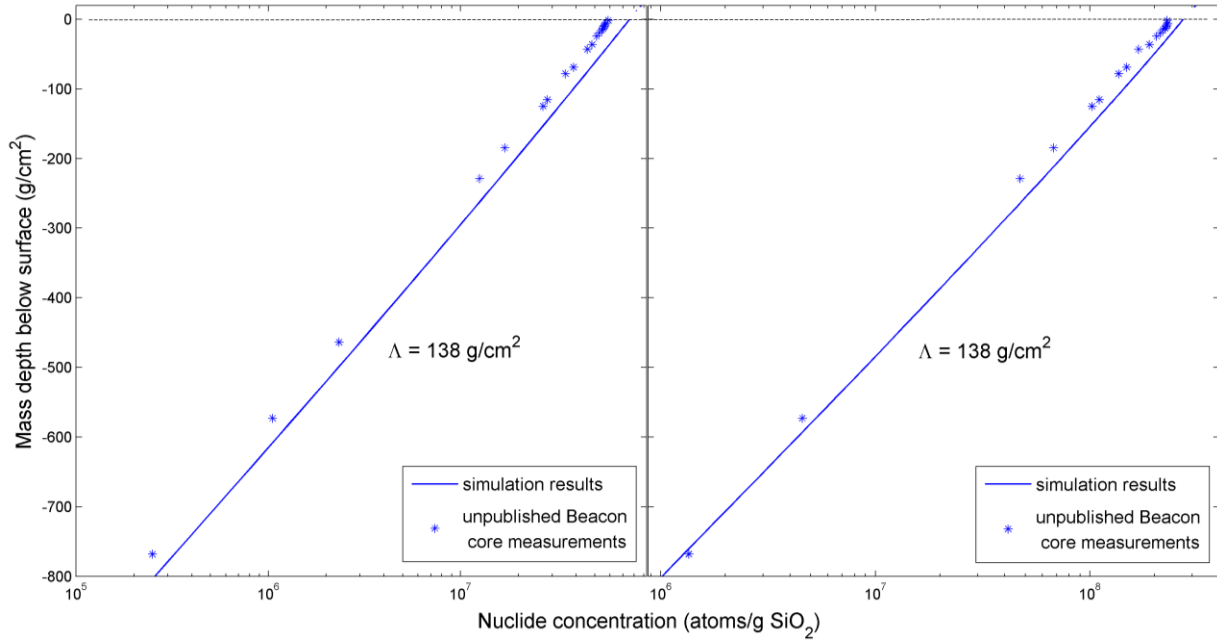
Figure 3.10 – Calculated $^{10}$Be and $^{26}$Al concentrations due to nucleonic spallation in simulation of Beacon Heights sandstone core along with measured values with concentrations due to muonic production subtracted out. Calculated profiles match well, with the calculated $^{10}$Be being ~25% high and the calculated $^{26}$Al being ~12% high. Dashed lines represent the logarithmic profile extensions for upper and lower portions of predicted concentrations.
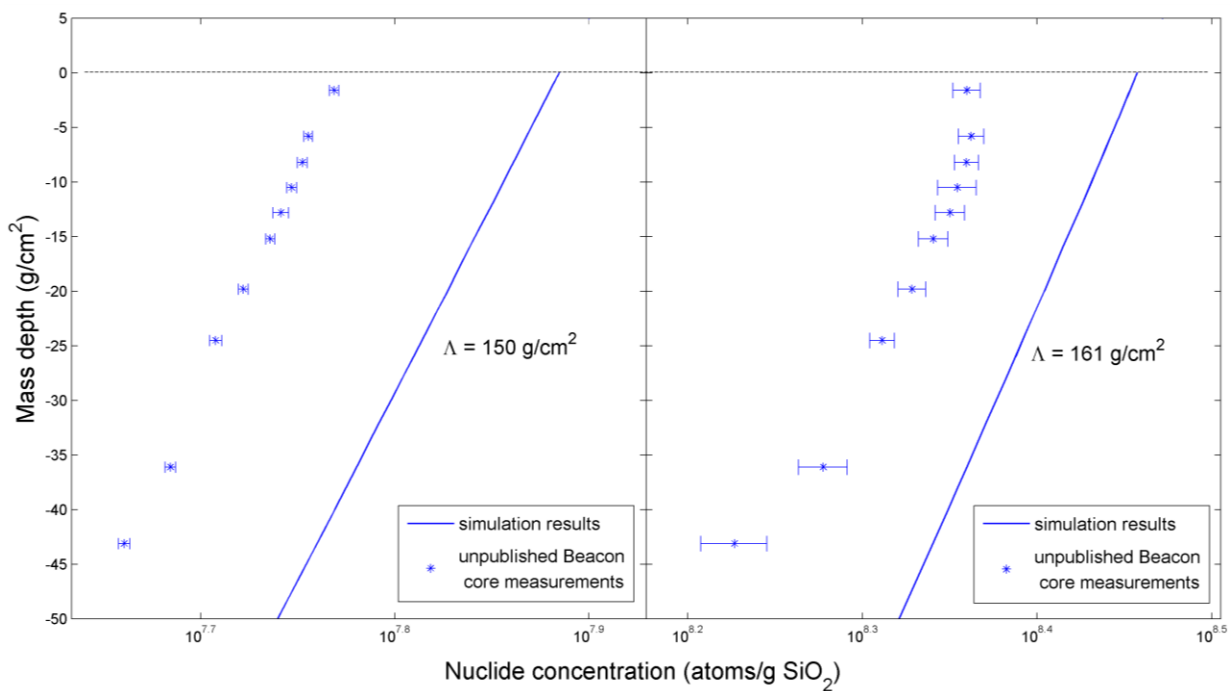


Figure 3.11 – Upper portion of Beacon Heights sandstone core calculated and measured values $^{10}$Be and $^{26}$Al concentrations due to nucleonic spallation. Attenuation length fits of 150 g/cm$^2$ and 161 g/cm$^2$ for calculated $^{10}$Be and $^{26}$Al results respectively generally track well with the measured attenuation length values. However, the $^{26}$Al measurements show a slight build up just below the surface which the simulations do not produce.

**Terrestrial cosmogenic production results**

To investigate cosmic-ray produced nuclide production rate scaling, we developed an artificially

deep atmosphere to propagate the cosmic radiation through. The artificially deep atmosphere

(~1.5 atmospheres) enables examination of radiation cascade and production rate scaling

characteristics without the biasing effect of a different surface material. Figures 3.12 (high

latitude) & 3.13 (low latitude) show the neutron and proton flux and the calculated production

rates of select cosmogenic nuclides as a function of atmospheric depth or altitude.



Figure 3.12 – High latitude (0 GV vertical rigidity cut-off) neutron flux, proton flux and total production rates as functions of atmospheric mass depth or altitude. Production rates for neutrons and protons are determined, then summed together. The very slight difference in slope of the production rate curves give rise to the isotope production ratios changing with altitude.

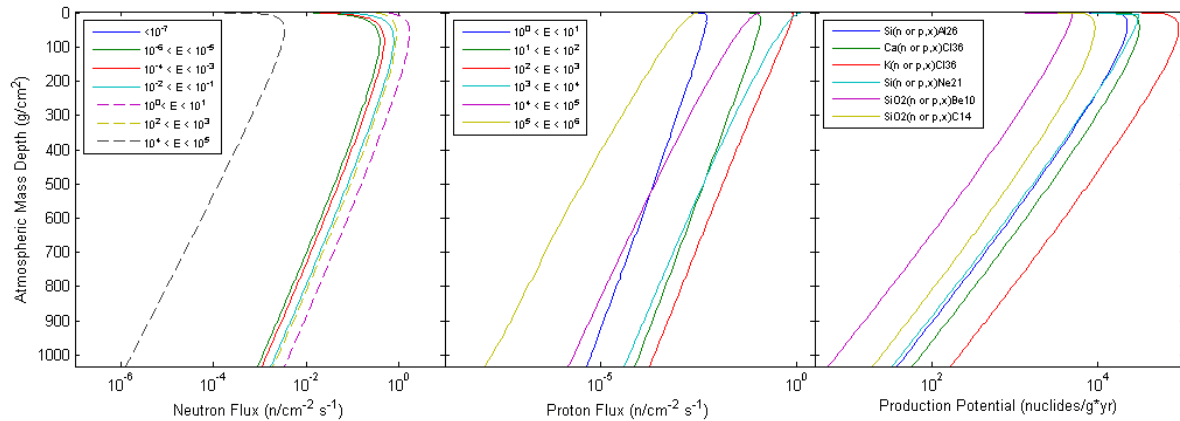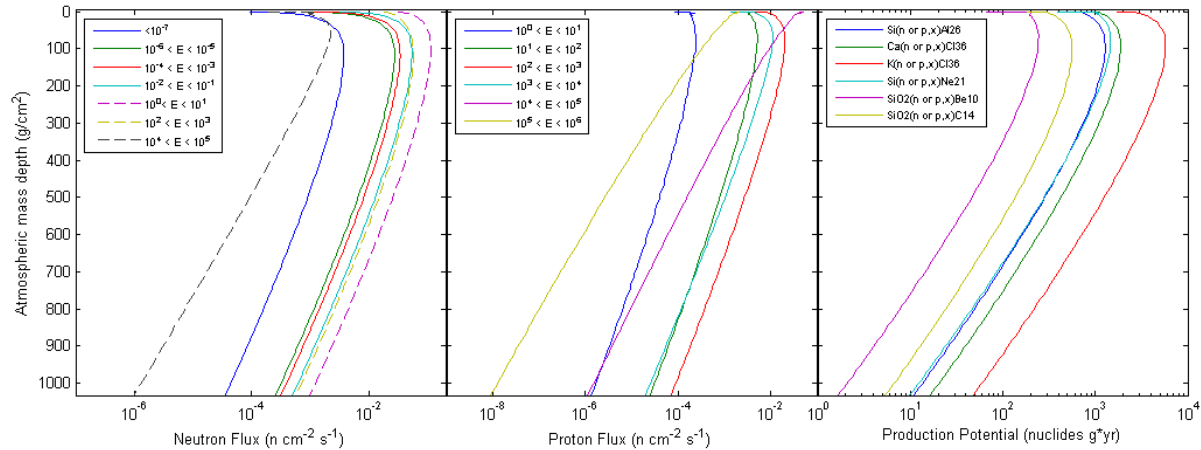Figure 3.13 – Neutron flux, proton flux and total production rates as functions of atmospheric mass depth at 16.4 GV vertical cut-off. This figure resembles that of the high latitude simulation. However, closer inspection reveals several important differences: i) the lower energy ranges of both neutrons and protons are relatively scarcer than at high latitude indicating a harder spectrum; ii) both the slope and the curvature of the all energy ranges are greater than at high latitude which yields a higher attenuation length that changes to a greater extent with altitude; iii) the peak values for both the neutrons and protons occur lower than at high latitude; and iv) the production rate potential curves also have noticeably greater curvature to them giving rise to a more dramatic change in attenuation length with altitude.

While the figures look very similar at first glance, looking closer reveals some important differences between the high latitude and the low latitude (16.4 GV vertical cut-off) simulation results. Starting with the neutron results, note that the overall magnitudes of the flux results are lower for the low latitude simulation. However, the peaks occur lower in altitude in the low latitude simulation and have less decrease in flux in all but the highest energy range. The differences here are the result of the geomagnetic modification to the primary GCR spectrum. With the lower portion of the spectrum being suppressed at lower latitude, the overall flux is reduced, while the radiation that is left has a greater penetrating power. A similar phenomenon happens with the protons, where if the various energy bins peak at all in the high latitude simulation, they do so in the first 20 g/cm$^2$. In the low latitude simulation, we see many of the lower energy bins peaking near 100 g/cm$^2$ atmospheric depth. The suppression of low energy protons in the source at low latitude means that the flux in this energy range is almost entirely

58

derived from spallations in the atmosphere. The aggregated results of production of select

cosmogenic nuclides from both neutrons and protons show similar patterns in their behavior with

altitude with the peaks in production potential occurring lower in the atmosphere with less

dramatic falloff in the low latitude simulation.

Deep atmosphere simulations of ten different latitudes were performed, including the unaltered

high latitude GCR source. The sea level production rates at high latitude for select nuclides are

listed in Table 3.2.

| Mineral / element and spallation nuclide | Production rate (atoms gram$^{-1}$ yr$^{-1}$) |
|---|---|
| $SiO_2 \rightarrow {}^{10}Be$ | 4.41 |
| $SiO_2 \rightarrow {}^{14}C$ | 15.1 |
| $SiO_2 \rightarrow {}^{26}Al$ | 29.6 |
| $Ca \rightarrow {}^{36}Cl$ | 45.4 |
| $K \rightarrow {}^{36}Cl$ | 131 |
| $SiO_2 \rightarrow {}^{21}Ne$ | 12.2 |

Table 3.2 – Sea level high latitude production rates of
commonly used cosmogenic nuclides from commonly used
minerals using McKinney, 2006 GCR spectra.

For the nine simulations of lower latitudes, we use angular cut-off skymap calculations to modify

the GCR source impinging on the top of the atmosphere. Figure 3.14 shows sea level ${}^{10}Be$ and

${}^{26}Al$ production rates for ten latitudes, organized by vertical cut-off rigidity. The production

rates show the expected falloff with increasing vertical cut-off rigidity. Complete tables of

production rates of commonly used nuclides as functions of altitude for each simulation can be

found in Appendix B.
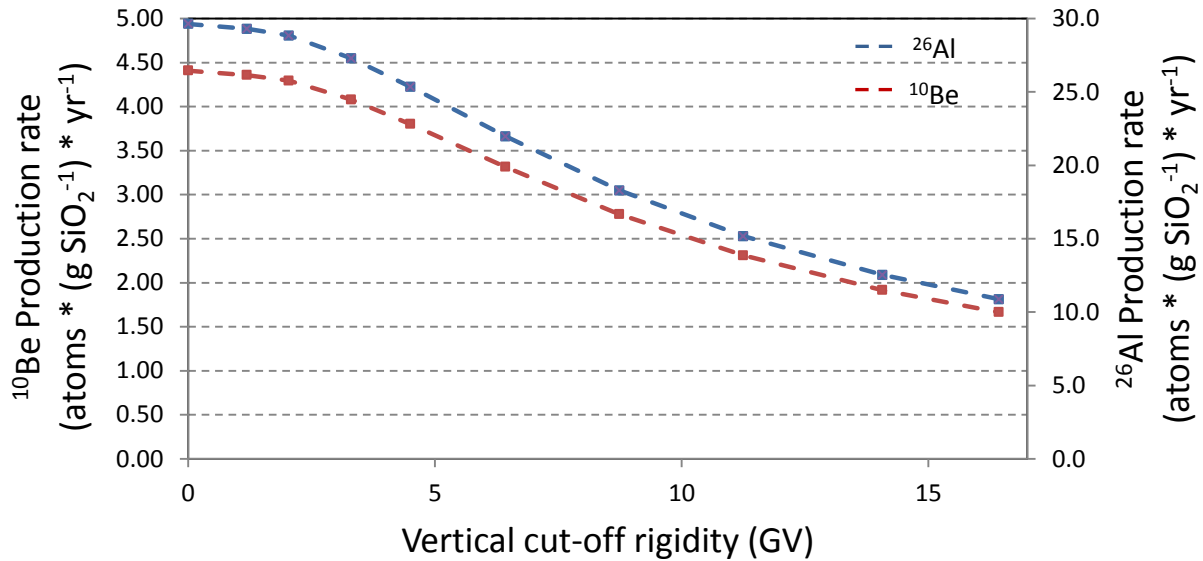
Figure 3.14 – Sea level $^{10}$Be and $^{26}$Al production rates at various vertical cut-off rigidities (geomagnetic latitude). Production rates at lower latitudes fall off normally with latitude although slightly more than expected in previous studies using McKinney, 2006 GCR spectra.

## DISCUSSION

### Validations

Simulation results of Dr. Goldhagen's Bonner Sphere measurements are ~30% lower than most recent analyses (McKinney et al., 2012). However, our results of the ground based measurements agree well at energies higher than ~1 GeV. Below 1 GeV, our results are generally higher than measurements except at thermal energies. The lower energy discrepancy is likely due to hydrated soil below the detector, whereas our simulations utilize an artificially deep atmosphere. There are numerous factors that could contribute to the discrepancies between our results and the Bonner Sphere measurements. As mentioned before, there are two minor sources of error in the original measurements: a lack of proton dosimetry during the measurements for exact proton subtraction, and the complex surroundings of the airplane. Within our model, there

are several sources of uncertainty and potential error. There is disagreement in the two GCR

models in the magnitude of the lower energy portion of the spectrum. There is also significant

disagreement of the models in the alpha particle spectrum and magnitude. While the alpha

portion of the total flux is small, it is important, as the alpha particles have a greater admittance

at lower rigidities because of their lower charge to mass ratio. In addition, low energy "re-

entrant" protons ejected out of the upper atmosphere and re-injected after traveling along

magnetic field lines may also explain some of the discrepancies at these very high altitudes. One

other possible source of error within our model is the curvature of low energy primary and

secondary protons in the uppermost atmosphere due to the geomagnetic field. In the work

presented here, we assume that the protons all travel in a straight line once they are injected into

the system, until they interact with an atmospheric atom. In the upper atmosphere, this could be

a very long distance, and the magnetic bending may have an effect on the altitude of deposition

and atmospheric penetration of the lower energy portion of the spectrum. For example, a 100

MeV proton at the top of the atmosphere in mid-latitudes would have a radius of curvature of ~1

km which could easily affect its point of deposition. On the other hand, a 1 GeV proton would

have a radius of curvature of ~100 km which would affect its trajectory and deposition less.

MCNPX does not have magnetic capabilities, so we cannot directly test this phenomenon. One

last source of uncertainty in these comparisons is the solar modulation and its effect on the GCR

spectrum. (Usoskin et al., 2011) indicates that the solar modulation parameter was ~400 MV at

the time of the measurements (June 1997). Uncertainty in this value will affect the lower energy

portion of the primary spectrum. However, if we consider the lack agreement in the upper

atmosphere in context with the good agreement with the measurements at sea level, we can infer

that the lack of re-entrant particles possibly in combination with magnetic deflection is likely the

source of discrepancy in the upper atmosphere. The high energy spectrum and transport seem to be working well, as the high energy component of the particle flux is the portion responsible for the deeply penetrating radiation.

The Beacon Heights sandstone drill core measurements are a unique data set to benchmark this model system against. Few other calibration sites are at this altitude. Furthermore, the core is ~30 meters deep, providing a deep production profile. The calculated concentration profiles agree well with measurements qualitatively, but are high by ~25% and ~12% for $^{10}$Be and $^{26}$Al respectively. The difference in the offsets is puzzling, as the offsets should be similar for the two nuclides. Equal offsets would indicate potential for a different erosion rate, a different long term barometric pressure, uplift, etc. This much of a difference in offsets could indicate an absence of physics needed to be accounted for (e.g. - snow cover or an issue with the cross sections). Results from the Knyahinya meteorite simulation are puzzling. The calculated nuclide productions exhibit the correct profile, but all seem to be off by a factor of ~ ½. Further investigation into this discrepancy is necessary. Two possible causes of offset are: (i) proton and neutron cross sections should have higher values at very high energies, (ii) the assumed long-term average solar modulation is incorrect, and (iii) alpha particles need to be considered in nuclide production. There are substantial fluxes of very high energy secondary particles throughout the meteorite simulation.

While none of our validation simulations agree exactly with measured data, we do find reasonable overall agreement with no scaling needed. Continued refinement of the input

radiation, transport physics and geologically relevant cross-sections will improve reproduction of these important benchmarks.


**Terrestrial production rates**

In this work, we organize our latitude results by vertical rigidity cut-off ($R_v$). This poses a slight ambiguity when comparing our results with other systems such as (Dunai, 2001) which uses a dipole form of vertical cutoff and (Desilets and Zreda, 2003; Lifton et al., 2008) which use "effective" cut-off. The latter works required a different cut-off term than vertical cut-off because of the non-uniformity in GCR cut-off at various angles and the resulting response of neutron monitors (Clem et al., 1997). Never-the-less, the differences should be small.

The results from the deep atmosphere can provide insight into the nuclide specific scaling with both altitude and latitude. The "attenuation length", the rate at which a nuclide production rate will increase or decrease with altitude, is an aspect of production systematics that has been difficult to quantify. By calculating production rates throughout the atmosphere, needing to know the attenuation length becomes unimportant. However, examining the attenuation length can lend insight into the behavior of the nuclide specific scaling. Figure 3.15 shows the attenuation lengths for some of the most commonly used cosmogenic nuclides at 0 GV (high latitude) and 16.4 GV (low latitude). In both cases, the attenuation lengths of each nuclide are slightly different and they diverge with altitude. This indicates the nuclide production rates are not scaling with altitude at the same rate. In addition, the attenuation lengths all increase with altitude suggesting that any scaling scheme not accounting for this physics will inaccurately predict production rates.
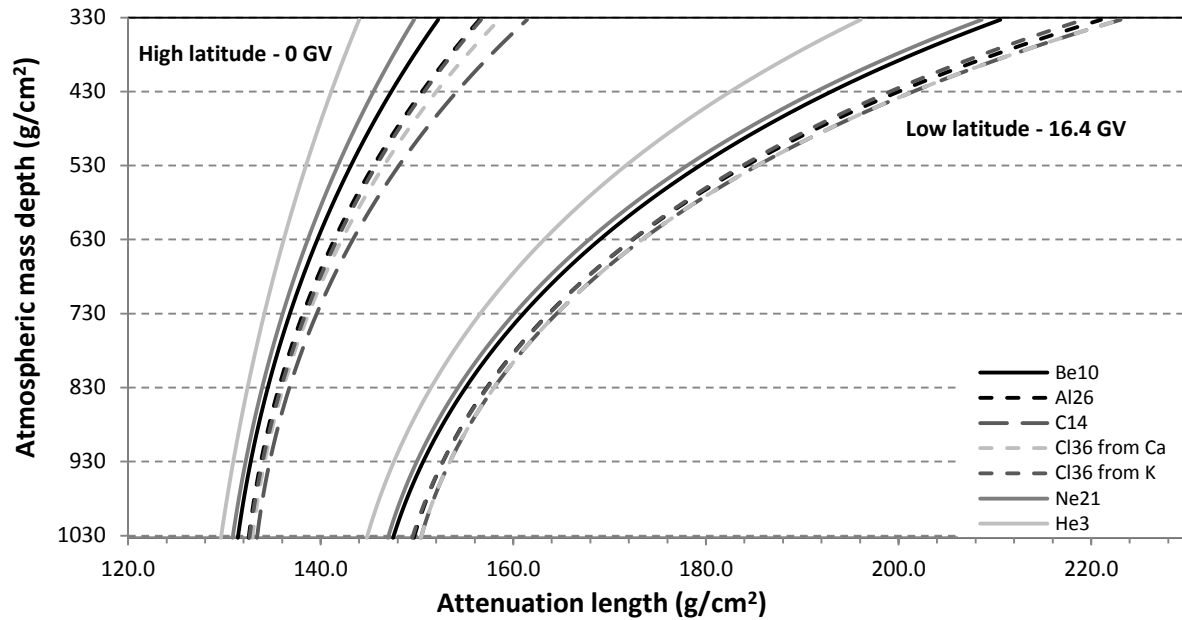
Figure 3.15 – Attenuation lengths for calculated nuclide production rates at 0 and 16.4 GV. Low latitude production rates exhibit greater attenuation lengths at sea level and also increase at a greater rate. High latitude attenuation lengths exhibit a greater divergence at altitude. Sea level is 1033 g/cm$^2$.

Most cosmogenic production rate calibration data is *in-situ* [10]Be concentrations in quartz. Hence, scaling schemes are heavily weighted to predict the altitude and latitude dependence of [10]Be. If a study relies on a different isotope or multiple isotopes, errors are introduced from lack of accounting for unique scaling. In Figure 3.16, we calculate the change in the isotope production ratios as a function of altitude in high and low latitude. These results can be used as the basis for a completely physics based nuclide dependent scaling scheme, or as a basis for augmenting existing scaling schemes.
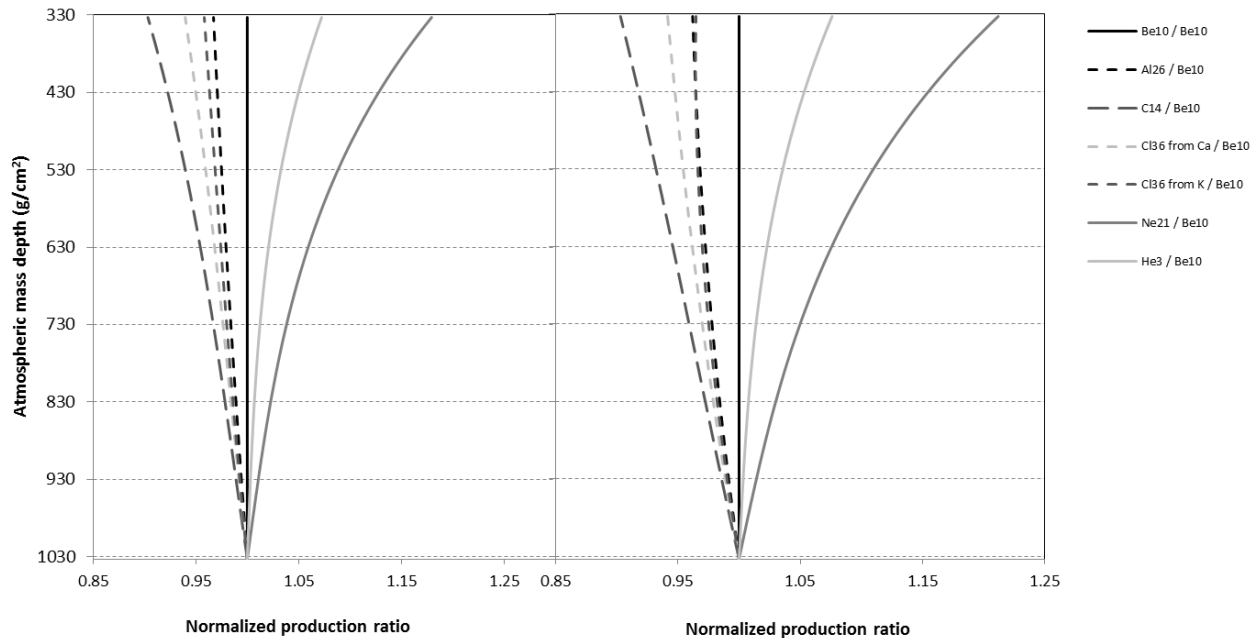
Figure 3.16 – High latitude (0 GV) and low latitude (16.4 GV) production rate ratios as functions of altitude and normalized to their respective sea level values. This demonstrates the error that a user may introduce into their calculations when making the assumption that all nuclides scale with altitude in similar fashion to $^{10}$Be – up to 12% at very high altitudes.

It should be noted that these production rates are specific to the matrix of air. A small "matrix" effect (Masarik and Reedy, 1994) can be experienced within a different material due to a different multiplicity which generally increases with the average atomic mass. However, this multiplicity is not expressed immediately but rather in a transition zone from 0 - ~100 g/cm$^2$. Matrix effects and subsurface production rate profiles will be discussed in a following study.

## CONCLUSION

Cosmic-ray produced nuclide production is a complex process that is affected by many variables. We have built a nuclide production rate system which is modular allowing us to investigate many facets of nuclide production systematics. We validate this model against a well-studied meteorite, Knyahinya (Graf et al., 1990), atmospheric neutron measurements (Goldhagen et al.,

2004), sea level production rates and the Beacon Heights sandstone drill core measurements. While no single measurement is reproduced exactly, the system does perform well in these broad benchmarks. It should be emphasized that there has been no scaling to achieve any benchmark value.

We find that at very high altitudes, the Usoskin and Kovaltsov (2006) GCR model reproduces the Goldhagen Bonner Sphere measurements (McKinney et al., 2012) better than the (McKinney et al., 2006) GCR model; however the sea level production rates are indistinguishable from each other. Sea level production rates calculated using McKinney et al. (2006) and Usoskin and Kovaltsov (2006) for commonly used cosmogenic nuclides are indistinguishable from each other. Results indicate nuclide production rates scale independently with altitude and latitude, with greater reduction at low latitudes than predicted by current scaling schemes. Production ratios can change by up to 20% at very high altitudes, suggesting systematic errors may exist from neglecting this factor.

## APPENDIX A – MCNPX settings

Mode card:

Protons, neutrons, muons, pions, kaons, deuterons, tritons, He-3 nuclei, and alpha particles are transported. Photons and electrons are ignored because of their lack of influence on hadronic flux and spallation reactions. Transporting photons and electrons also increases the computation time dramatically.

Proton physics: phys:h card: 4000001 0 -1 J 0 J 0 3j 0.917

The term "4000001" denotes a maximum energy of 4 TeV was chosen to account for the maximum energy contained in the defined primary alpha spectrum. The next "0" denotes that "no implicit capture" is chosen. The "-1" denotes that MCNPX will use whatever evaluated table data it has and will use models when evaluated data is not available. "J" is a placeholder and does not impact the functionality of the code. The next "0" denotes Vavilov straggling, the default method within MCNPX for ionization energy loss. The next "J" is a placeholder. The next "0" denotes no light ion recoil. This option is a heating concern, rather than a potential spallation concern. The particles that could cause spallations to any significant extent are already transported and tallied. Thus, the option is turned off to reduce computation time. "3j" denotes three placeholders in a row. "0.917" is the default energy spacing in MeV.

Neutron physics: phys:n 4000001 0 0 0 -1 0 0

The term "4000001" is the maximum energy for neutrons as above (as well as all particles listed below). The next "0" denotes that "no implicit capture" is chosen. The next "0" denotes that unresolved resonance probability treatment is on (default). The next "0" denotes that delayed

neutrons are treated as prompt. These simulations are of long term average cosmic ray conditions, so the very small time difference between prompt and delayed neutrons will not have any effect on the results. This term is much more important in criticality calculations when the precise timing of energy release will have profound effects on the state of a chain reaction system. The next "-1" denotes that MCNPX will use whatever evaluated table data it has, and use models when evaluated data is not available. The next "0" denotes integer neutrons per fission, the default in MCNPX. The last "0" denotes no light ion recoil, as above.

Muon, pion, kaon, deuteron, triton, He-3 nucleus, and alpha particle physics:

phys:| 4000001 J J J 0      $muons

phys:/ 4000001 J J J 0      $pions

phys:K 4000001 J J J 0       $kaons

phys:D 4000001 J J J 0        $deuterons

phys:T 4000001 J J J 0       $tritons

phys:S 4000001 J J J 0       $He3s

phys:A 4000001 J J J 0       $aplhas

The same maximum energy is chosen for these particles as above. The next three "J"s are unused placeholders. The next "0" denotes the default Vavilov straggling for ionization energy loss.

LCA physics: LCA 2 1 0 0023 1 1 0 1 1 1

The first term, "2" (default), denotes elastic scattering for both neutrons and protons. The second term, "1" (default) denotes pre-equilibrium treatment for the nucleus after intranuclear cascade. The third term, "0" denotes no use of the ISABEL intra-nuclear cascade model for any particle. The fourth term, "0023", is the default term for controlling the ISABEL model which becomes irrelevant in this case. The fifth term, "1" (default), denotes that the Coulomb barrier is on. The

sixth term, "1" (default), denotes that recoil particle energy is subtracted from the excitation energy of the excited nucleus. The seventh term, "0" (default), denotes that pions are captured by a nucleus when the cut-off energy is reached. The other option is for forced decay. It is not clear whether one option is more appropriate than the other, but with a cut-off energy of 1 MeV, this should have a negligible effect. The eighth term, "1" (default), denotes normal transport. Other options available via this term are for use when exploring cross section physics. The ninth term, "1" denotes use of the CEM03 model for all high E. CEM03 is the combined package of both the CEM and LAQGSM models. This is not the default in MCNPX, but is considered essential to modeling systems with cosmic-ray magnitude energies, as CEM03 is considered to be a superior modeling of the high energy nuclear reactions. The tenth term,"1", denotes the use of LAQGSM over ISABEL in lower energies and FLUKA in higher energies. It is not clear from the user manual why this option is offered, or whether or not the choosing of the CEM03 model in the ninth term makes this tenth term redundant. However, the version of FLUKA contained in MCNPX is an old version, and should be avoided in very large systems like these where small differences in recoil nucleon number, energy and angle of recoil are compounded through the atmosphere.

LCB physics: LCB 1000 1000 j j j j j j

The first term, "1000", denotes the energy in MeV below which the CEM is used. The second term, also "1000", denotes the energy in MeV above which LAQGSM is used. The transition energy of 1000 MeV is not the default for MCNPX (the default is 3500 MeV). However, 1000 MeV is the recommended transition energy from CEM and LAQGSM for high energy particle interactions with light nuclei (lighter than oxygen) (Mashnik, 2008). The primary difference

between the two models is that CEM does not consider the so-called nuclear "trawling" effect, or nucleon depletion, whereas LAQGSM does. Because of the atmosphere's generally light elemental constitution, we use the minimum setting, 1 GeV, as recommended. The rest of the terms in the LCB card are marked as default, as these dictate the control of the Bertin or ISABEL models, which are irrelevant to these simulations.

Lost particles:

We have observed a comparatively small number of particles being "lost" by MCNPX, with the accompanying error: "no intersection found in subroutine track." The MCNPX development team has indicated that it is likely the result of the rare instance of a number rounding which places the tracked particle just on the other side of a surface than it should have been. The default number of lost particles for MCNPX to terminate a run is 10. Because of the size and length of these simulations, we frequently exceed this value. Thus, using the Lost card with a sufficiently large number such as 1,000 avoids an early termination of the simulation. This should be used with caution, as lost particles often can indicate a geometric error.

# REFERENCES

Argento, D.C., Reedy, R.C., Stone, J.O., 2013. Modeling the earth's cosmic radiation. Nuclear Instruments and Methods B 294, 464-469.

Balco, G., Rovey II, C.W., 2008. AN ISOCHRON METHOD FOR COSMOGENIC-NUCLIDE DATING OF BURIED SOILS AND SEDIMENTS. American Journal of Science 308, 1083-1114.

Balco, G., Stone, J., 2005. Measuring middle Pleistocene erosion rates with cosmic-ray-produced nuclides in buried alluvial sediment, Fisher Valley, southeastern Utah. Earth Surface Processes and Landforms 30, 1051-1067.

Balco, G., Stone, J., Jennings, C., 2005. DATING PLIO-PLEISTOCENE GLACIAL SEDIMENTS USING THE COSMIC-RAY-PRODUCED RADIONUCLIDES Be-10 and Al-26. American Journal of Science 305, 1-41.

Bierman, P., Steig, E.J., 1996. Estimating rates of denudation using cosmogenic isotope abundances in sediment. Earth Surface Processes and Landforms 21, 125-139.

Burger, R.A., Potgieter, M.S., Heber, B., 2000. Rigidity dependence of cosmic ray proton latitudinal gradients measured by the Ulysses spacecraft: Implications for the diffusion tensor. Journal of Geophysical Research - Space Physics 105, 27,447-427,455.

Carmichael, H., Bercovitch, M., 1969. V. Analysis of IQSY cosmic-ray survey measurements. Canadian Journal of Physics 47, 2073.

Castagnoli, G., Lal, D., 1980. SOLAR MODULATION EFFECTS IN TERRESTRAIL PRODUCTION OF CARBON-14. Radiocarbon 22, 133-158.

Clem, J., Angelis, G.D., Goldhagen, P., Wilson, J.W., 2004. NEW CALCULATIONS OF THE ATMOSPHERIC COSMIC RADIATION FIELD - RESULTS FOR NEUTRON SPECTRA. Radiation Protection Dosimetry 110, 423-428.

Clem, J.M., Bieber, J.W., Evenson, P.A., Hall, D., Humble, J.E., Duldig, M.L., 1997. Contribution of obliquely incident particles to neutron monitor counting rate. Journal of Geophysical Research 102, 1-8.

Desilets, D., Zreda, M.G., 2003. Spatial and temporal distribution of secondary cosmic-ray nucleon intensities and applications to in situ cosmogenic dating. Earth and Planetary Science Letters 206, 21-42.

Dubin, M., Hull, A.R., Champion, K.S.W., 1976. US Standard Atmosphere, 1976. 241.

Dunai, T.J., 2001. Infuence of secular variation of the geomagnetic field on production rates of in situ produced cosmogenic nuclides. Earth and Planetary Science Letters 193, 197-212.

Erlanger, E.D., Granger, D.E., Gibbon, R.J., 2012. Rock uplift rates in South Africa from isochron burial dating of fluvial and marine terraces. Geology 40, 1019-1022.

Garcia-Munoz, M., Mason, G.M., Simpson, J.A., 1975. The anomolous 4He component in the cosmic-ray spectrum at <= 50 MeV per nucleon during 1972-1974. The Astrophysical Journal 202, 265-275.

Goldhagen, P., Clem, J., Wilson, J.W., 2004. THE ENERGY SPECTRUM OF COSMIC-RAY INDUCED NEUTRONS MEASURED ON AN AIRPLANE OVER A WIDE RANGE OF ALTITUDE AND LATITUDE. Radiation Protection Dosimetry 110, 387-392.

Goldhagen, P., Clem, J.M., Wilson, J.W., 2003. RECENT RESULTS FROM MEASUREMENTS OF THE ENERGY SPECTRUM OF COSMIC-RAY INDUCED NEUTRONS ABOARD AN ER-2 AIRPLANE AND ON THE GROUND. Advanced Space Research 32, 35-40.

Goldhagen, P., Reginatto, M., Kniss, T., Wilson, J.W., Singleterry, R.C., Jones, I.W., Van Steveninck, W., 2002. Measurement ofthe energy spectrum of cosmic-ray induced neutrons aboard an ER-2 high-altitude airplane. Nuclear Instruments and Methods A 476, 42-51.

Gordon, M.S., Goldhagen, P., Rodbell, K.P., Zabel, T.H., Tang, H.H.K., Clem, J., Bailey, P., 2005. Correction to "Measurement of the Flux and Anergy Spectrum of Cosmic-Ray Induced Neutrons on the Ground". IEEE Transactions on Nuclear Science 52, 2703.

Graf, T., Signer, P., Wieler, R., Herpers, U., Sarafin, R., Vogt, S., Fieni, C., Pellas, P., Bonani, G., Suter, M., Wolfli, W., 1990. Cosmogenic nuclides and nuclear tracks in the chondrite Knyahinya. Geochimica et Cosmochimica Acta 54, 2511-2520.

James, M.R., McKinney, G.W., Hendricks, J.S., Moyers, M., 2006. Recent enhancements in MCNPX: Heavy-ion transport and the LAQGSM physics model. Nuclear Instruments and Methods A 562, 819-822.

Lal, D., 1988a. IN SITU-PRODUCED COSMOGENIC ISOTOPES IN TERRESTRIAL ROCKS. Annual Review of Earth Planet Science 16, 355-388.

Lal, D., 1988b. Theoretically expected variations in the terrestrial cosmic-ray production rates of isotopes, In: Castagnoli, G. (Ed.), International School of Physics (1985). North-Holland, Varenna on Lake Como, pp. 216-233.

Lal, D., 1991. Cosmic-ray labeling of erosion surfaces: in situ nuclide production rates and erosion models. Earth and Planetary Science Letters 104, 424-439.

Leya, I., Masarik, J., 2009. Cosmogenic nuclides in stony meteorites revisited. Meteoritics & Planetary Science 44, 1061 - 1086.

Lifton, N.A., Smart, D.F., Shea, M.A., 2008. Scaling time-integrated in situ cosmogenic nuclide production rates using a continuous geomagnetic model. Earth and Planetary Science Letters 268, 190-201.

Masarik, J., Beer, J., 2009. An updated simulation of particle fluxes and cosmogenic nuclide production in the Earth's atmosphere. Journal of Geophysical Research - Atmospheres 114, 1-9.

Masarik, J., Reedy, R., 1994. Effects of bulk composition on nuclide production process in meteorites. Geochimica et Cosmochimica Acta 58, 5307-5317.

Masarik, J., Reedy, R.C., 1995. Terrestrial cosmogenic-nuclide production systematics calculated from numerical simulations. Earth and Planetary Science Letters 136, 381-395.

Mashnik, S.G., 2008. Overview and Validation of the CEM and LAQGSM Event Generators for MCNP6, MCNPX, and MARS15, 1st Workshop on Accelerator Radiation Induced Activation, Paul Scherrer Institut, Switzerland.

McKinney, G.W., Armstrong, H.J., James, M.R., Clem, J.M., Goldhagen, P., 2012. MCNP6 Cosmic-Source Option. Transactions of the American Nuclear Society 106.

McKinney, G.W., Lawrence, D.J., Prettyman, T.H., Elphic, R.C., Feldman, W.C., Hagerty, J.J., 2006. MCNPX benchmark for cosmic ray interactions with the Moon. Journal of Geophysical Research 111, 1-14.

O'Brien, K., 2008. Limitations of the Use of the Vertical Cut-off to Calculate Cosmic-ray Propogation in the Earth's Atmosphere. Radiation Protection Dosimetry 128, 259-260.

Pelowitz, D.B., 2011. MCNPX User's Manual, Version 2.7.0, In: Energy, D.o. (Ed.). Los Alamos National Laboratory.

Reedy, R.C., 1987. Nuclide Production by Primary Cosmic-Ray Protons. Journal of Geophysical Research 92, E697-E702.

Reedy, R.C., 2013. Cosmogenic-Nuclide production rates: reaction cross section update. Nuclear Instruments and Methods B 294, 470-474.

Schaefer, J., Denton, G., Kaplan, M., Putnam, A., Finkel, R.C., Barrel, D.J.A., Andersen, B.G., Schwartz, R., Mackintosh, A., Chinn, T., Schluchter, C., 2009. High-Frequency Holocene Glacier Fluctuations on New Zealand Differ from the Northern Signature. Science 324, 622-625.

Schimmelpfennig, I., Schaefer, J.M., Goehring, B.M., Lifton, N.A., Putnam, A.E., Barrel, D.J.A., 2012. Calibration of the in situ cosmogenic 14C production rate in New Zealand's Southern Alps. Journal of Quaternary Science 27, 671-674.

Steinhilber, F., Abreu, J.A., Beer, J., 2008. Solar modulation during the Holocene. Astrophysics and Space Science Transactions 4, 1-6.

Stone, J., 2000. Air pressure and cosmogenic isotope production. Journal of Geophysical Research 105, 23,753-723,759.

Urch, I.H., Gleeson, L.J., 1972. GALACTIC COSMIC-RAY MODULATION FROM 1965-1970. Astrophys. Space Sci. 17, 426-&.

Usoskin, I.G., Bazilevskaya, G.A., Kovaltsov, G.A., 2011. Solar modulation parameter for cosmic rays since 1936 reconstructed from ground-based neutron monitors and ionization chambers. Journal of Geophysical Research 116.

Usoskin, I.G., Kovaltsov, G.A., 2006. Cosmic ray induced ionization in the atmosphere: Full modeling and practical applications. Journal of Geophysical Research 111, 1-9.

Usoskin, I.G., Solanki, S.K., Kovaltsov, G.A., Beer, J., Kromer, B., 2006. Solar proton events in cosmogenic isotope data. Geophysical Research Letters 33.

Chapter 4



Key aspects of in-situ cosmogenic nuclide production:

Insights from a physics based model

## ABSTRACT

Characteristics of the spallogenic component of nuclide production are investigated through the use of a firs-principles, nuclear-physics based model. Nuclide specific production for commonly used nuclides indicates differences in scaling up to 15% at very high altitude. Angular distribution of nuclide forming particles suggests the current method of shielding correction which is neither altitude nor latitude dependent could be introducing pervasive errors of a few percent. Subsurface production profiles suggest that erosion corrections should be performed with non-constant attenuation lengths. Results are parameterized for easy application.

# INTRODUCTION

## Overview

Cosmogenic nuclide methods have opened the door to quantification of numerous aspects of geomorphology, and holds promise for even more. As methods and studies continue to require increasing accuracy, our understanding of the physics and characteristics of nuclide production must also grow. Chapter 3 describes a physics-based system developed to investigate the characteristics of both the cosmic-ray radiation field and the resulting production rate potential of that field.

Many independently dated calibration sites have been sampled by the CRONUS collaboration and others. The calibration sites were meant to be used both as local calibrations as well as benchmarks for assessing scaling schemes ability to predict sample concentrations. Surprisingly, time-dependent models (Desilets and Zreda, 2003; Dunai, 2001; Lifton et al., 2008) do not predict the scaling data any better than the original time-invariant model (Lal, 1991). Many conclude that this indicates a problem with scaling schemes or the calibration sites, or both. This conclusion neglects the possibility for errors in other systematic correction factors.

The systematic errors possible due to nuclide specific scaling with altitude, latitude (Lifton et al., 2008), and subsurface (Masarik and Reedy, 1995), and improper shielding corrections (Dunai, 2010; Gosse and Phillips, 2001) can be significant. As shown here, neglecting nuclide specific scaling can potentially incur up to 15% error at very high altitudes; low angle shielding corrections should be more substantial than currently estimated (Gosse and Phillips, 2001) causing pervasive error; and subsurface production rates are not adequately described by simple

exponentials.  Our physics based model allows us to investigate these subtle yet important

phenomena.


**Nuclide production**

As shown in Chapter 2 (Argento et al., 2013) and Chapter 3, the energy spectra of both neutrons

and protons changes throughout the atmosphere.  Figure 4.1 shows high-latitude neutron and

proton energy spectra sampled at 100 $g/cm^2$ intervals and normalized to the 500 $g/cm^2$ spectra.

The neutron and proton spectra at 1,000 $g/cm^2$ have the greatest relative enhancement of lower

energies (softest spectra), while the 400 $g/cm^2$ spectra have the greatest relative enhancement in

the higher energies (hardest spectra). This demonstrates how the neutron and proton energy

distributions shift towards lower energies with atmospheric depth.  Each cosmogenic nuclide has

its own set of target elements and unique cross section (Reedy, 2013).  Taken together, this

suggests that we should expect each nuclide production rate to scale uniquely.
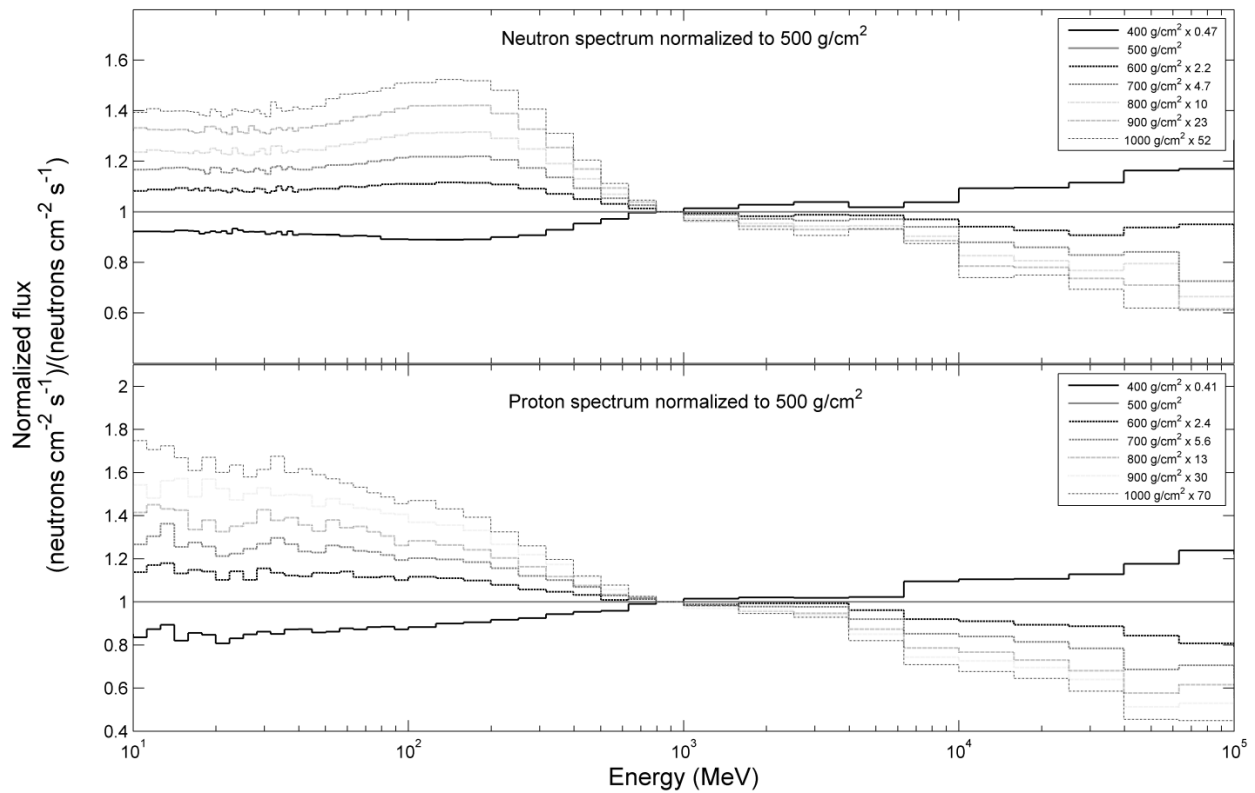
Figure 4.1 – Neutron and proton energy distributions normalized and compared to the energy distribution at 500 g/cm$^2$. With increasing atmospheric depth (decreasing altitude), the energy distribution for both neutrons and protons "softens" or shifts towards the lower energies.

Like the other topics this work examines, nuclide specific scaling is a theory that has been extremely difficult to verify or disprove empirically (Amidon et al., 2008; Gayer et al., 2004; Schimmelpfennig et al., 2011). Because the majority of nuclide sampling and calibration work is based on $^{10}$Be, it is likely that studies employing other nuclides ($^3$He, $^{21}$Ne, $^{26}$Al, $^{36}$Cl, etc.) will contain the systematic error of scaling from sea level high latitude as $^{10}$Be would, rather than the nuclide in use. In Chapter 3, it is shown that a single exponential function with a single attenuation length cannot adequately describe the variation of nuclide production rates as functions of atmospheric depth and cutoff rigidity. Instead, each nuclide's production rate is described by a unique function, and nuclide production ratios vary with both altitude and cut-off rigidity. We use polynomial fitting in natural log space to generate accurate fit functions of

production rates.  These functions can be used to explore production ratios and applied to existing scaling schemes.

*In-situ* cosmogenic nuclide studies rely on correctly accounting for geometric shielding of a given sample.  Currently, angular distribution of spallogenic nuclide producing particles is described by the cosine term:

$$P(\theta) = cos^m(\theta) \qquad \text{(Dunai, 2010; Gosse and Phillips, 2001)} \qquad \text{Eq. 4.1}$$

where $m = 2.3$.  This value first appears in (Nishiizumi et al., 1989) and derives from several sources (Barford and Davis, 1952; Conversi and Rothwell, 1954; Heidbreder et al., 1970; Heidbreder et al., 1971; Lal et al., 1958), all of which have significant uncertainties.  While this form of shielding correction has sufficed for some time, it is well understood that the high energy cosmic-ray field becomes more collimated with depth below the maximum because the lower angle particles have to penetrate more mass to arrive at a given altitude; this leads to the conclusion that $m$ should be a function of altitude if not latitude as well.  However, this has would be difficult to quantify empirically and has not been addressed in any calibration study on natural samples.  Our simulations capture both angular and energy distribution for neutrons and protons.  We use these results, folded with nuclide production cross sections to determine angular production potential at a number of altitudes and latitudes for $^{10}$Be.  We present our results in a modified form of the traditional form listed above to account for the non-insignificant horizontal component our calculations predict.
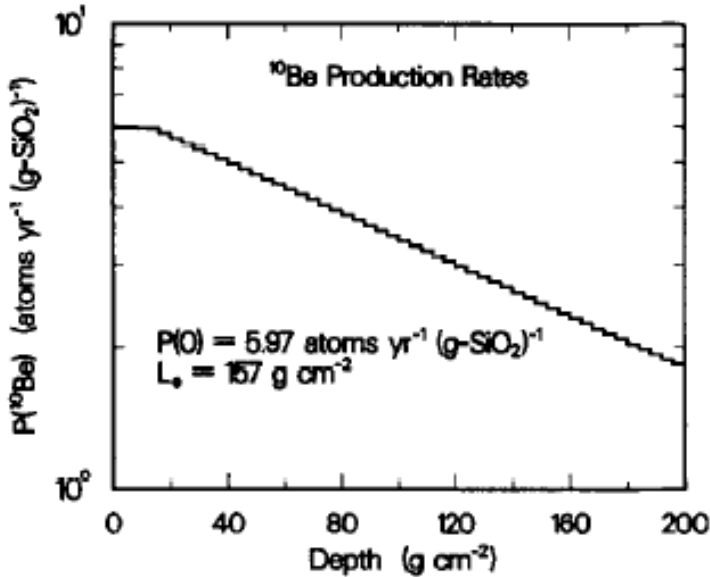
Figure 4.2 – Subsurface [10]Be production profile from Masarik
and Reedy, 1995. X-axis is depth below surface in g/cm^{2}, and y-
axis is [10]Be production rate. Production rate in the uppermost 20
g/cm^{2} (~8 cm) is constant.

Masarik & Reedy (1995) first proposed the possibility of a non-exponential decrease near the

surface (Figure 4.2). They cite enhancement in multiplicity, the average number of energetic

particles ejected from the collision, from the air to the rock as the cause. Little geologic

evidence has supported those specific results, however. Until recently, this effect has not been

seen in depth profile measurements on natural samples (Kubik and Reuther, 2007) (Stone et al.,

in preparation), in large part because even small amounts of erosion remove this near-surface

production profile effect from accumulated nuclide depth profiles. To investigate this

phenomenon further, we fold the subsurface neutron and proton simulations results with energy

dependent cross sections (excitation functions) in three rock types: sandstone, granite and basalt.

We chose these three rock types to investigate the effect of average atomic mass on subsurface

production results with the quartzose sandstone having the lowest and the basalt having the

highest. These results supersede those of (Argento et al., 2013) with several refinements

described in Chapter 3. The results have implications for both scaling, nuclide production ratio studies as well as for erosion corrections.


## METHODS

### Physics based model

Production rates and ratios are calculated entirely through first principles, using empiric data to benchmark how well the system is performing as described in Chapter 3. Beginning with a galactic cosmic-ray model (Usoskin and Kovaltsov, 2006) and modified by cutoff calculations (O'Brien, 2008), proton and alpha spectra are defined for geomagnetic conditions ordered by vertical cutoff rigidity (GV). The geomagnetically modified GCR spectra is used as the source radiation for simulations in MCNPX (Monte Carlo N-Particle eXtended) v2.7. Production rates are calculated by folding neutron and proton fluxes with energy dependent nuclide production cross sections (Reedy, 2013) as described in Chapter 3.


### Geometries

The model geometries used here are made of concentric spheres. For investigation of nuclide production scaling and angular distribution, artificially deep atmospheres are utilized to study the behavior of radiation and resulting nuclide production in air without the effect of a different surface material beneath the model atmosphere. Neutron and proton flux spectra and magnitudes are controlled by the local and nearby material. A different surface material would influence the fluxes of the lower atmosphere skewing the production rate scaling results. In both cases, Standard US Atmosphere, 1976 is used to model the atmosphere.

For the deep atmosphere simulations, the tropospheric lapse rate is used to continue the atmosphere below sea level.  Angular data was captured in $1/10^{th}$ cosine steps in addition to energy binning, allowing for full cross section folding in each angular bin.

Boundary effects and subsurface production rates are explored by using solid planets of sandstone, granite and basalt.  The rock surfaces are at sea level.  Sandstone is modeled as pure $SiO_2$ with density 2.33 g/cm$^3$ and 12% void space which is filled with air.  Granite and basalt are modeled with density 2.7 g/cm$^3$ and 3.0 g/cm$^3$ respectively with no pore space.  Compositions are listed in Table 4.1.

| Element | Granite concentration (mol/mol) | Basalt concentration (mol/mol) |
|---------|---------|---------|
| H | 0.0249 | 0.0008 |
| Li | 1.06e-6 | |
| B | 2.75e-6 | |
| O | 0.55759 | 0.5981 |
| F | | 0.0002 |
| Na | 0.0345 | 0.0252 |
| Mg | 0.05358 | 0.03784 |
| Al | 0.0797 | 0.0811 |
| Si | 0.24704 | 0.18776 |
| P | 0.001 | 0.0009 |
| K | 0.0274 | 0.03 |
| Ca | 0.008419 | 0.040622 |
| Ti | 0.001272 | 0.00558 |
| Mn | 0.0002 | 0.0005 |
| Fe | 0.012613 | 1.8481 |
| Sm | 2.2e-6 | |
| Gd | 2.2e-6 | |

Table 4.1 – Concentrations of granite and basalt used in simulations

**Parameterizing and fitting**

Mono-energetic radiation is absorbed exponentially with mass. Radiation that spans a range of energy will be absorbed roughly exponentially. While the cosmic-ray flux increases through the first ~150 g/cm$^2$, plateaus briefly, then gradually decreases, it is decreasing roughly exponentially in geologically relevant altitudes.

By fitting the omnidirectional production rates as a function of altitude in the natural logarithm space, we seek to address the limitations of fitting an exponential system with polynomials (Lal, 1991) in linear space: (i) Polynomials have little chance of accurately fitting an exponential type function with the accuracy desired for these studies, (ii) fitting in natural log space can describe the changing attenuation length well. These evaluated fits are valid for up to 8 km, covering all but the highest mountain altitudes. Above this region, the prescribed fits diverge from simulation results.

The angular production rates were fit functions in the form of $P(\theta) = A \cdot \cos^m(\theta) + C$ to match the calculated production rates. We use the added constant C to account for the production by cosmic-rays with near-horizontal incidence, the effect of which is suppressed in the conventional $\cos^m(\theta)$ procedure.

## RESULTS

**Total production rate scaling**

Our calculations indicate that production rates scale uniquely and non-linearly in natural log space. Using Eq. 4.2 in conjunction with the provided polynomial values in Appendix A, one

can evaluate the production rate at any altitude between 0.5 km below and 8 km above sea level

(1080 g/cm$^2$ to 350 g/cm$^2$), for a given vertical rigidity cutoff according to our simulated results.

$$P_i(z) = e^{\left(a_i(1033-z)^3 + b_i(1033-z)^2 + c_i(1033-z) + d_i\right)}$$
Eq. 4.2

z is atmospheric depth in g/cm$^2$. Sea level atmospheric depth is 1033 g/cm$^2$ or 1013 hPa in this

system. Production rate ratios can be quickly determined by taking the ratio of one production

fit to another as in Eq 4.3:

$$\frac{P_i(z)}{P_j(z)} = \frac{e^{\left(a_i z^3 + b_i z^2 + c_i z + d_i\right)}}{e^{\left(a_j z^3 + b_j z^2 + c_j z + d_j\right)}}$$
Eq. 4.3

**Angular distribution of nuclide production rates**

Our simulations capture both angular and energy data allowing calculations of production

potential. Here, we have calculated the angular potential for [10]Be at various vertical cutoff

rigidities and altitudes. Figure 4.3 shows the integral normalized angular production results at

sea level and high latitude. The integrated $\cos^{2.3}(\theta)$ function is plotted with the same bins as our

simulation tally. The simulation results show a component of nuclide production from near-

horizontal radiation that is neglected by the standard m = 2.3 function. Furthermore, simulations

show a component of spallogenic production coming from below the tally surface. This is the

product of both scattered neutrons and protons and evaporation neutrons which are released

isotropically (Dunai, 2010). How much of the horizontal component is due to energetic

secondary cosmic-rays produced in spallations and can travel substantial distance versus lower

energy evaporation particles which would necessarily be produced nearby cannot be determined

in this study. This implies that distant horizons (e.g., mountains) may have different shielding

factors than something relatively nearby. Regardless of the nature of the particles responsible for

the production from the low-angle bin, the form and evaluated values presented should provide

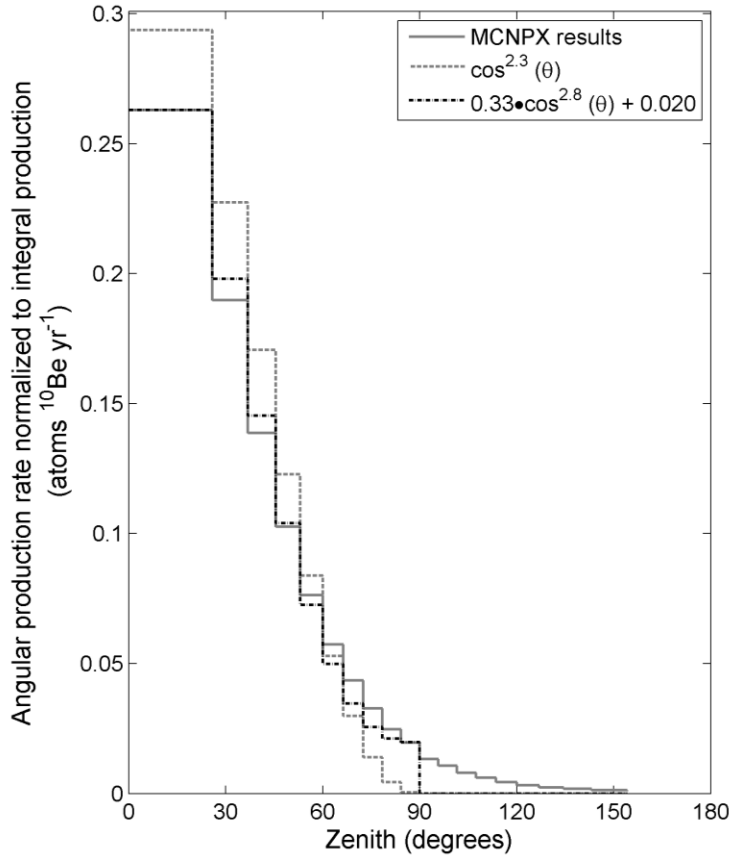significantly more accurate shielding corrections.



Figure 4.3 – High latitude angular production rate distribution at sea level.
Results do not match well with the assumed $\cos^{2.3}(\theta)$ distribution. Rather,
the distribution is more collimated, but yet with a greater horizontal
component. Also of note is the non-insignificant production coming from
below the surface. This is not from a subterranean source, but rather from
neutrons and protons being scattered into the upward direction.

In Figure 4.4, we present high and low latitude (0 GV and 16.4 GV) and high and low altitude

(sea level and 430 g/cm$^2$), each having the MCNPX results, $\cos^{2.3}(\theta)$, and the fitted function.

The results show that, with increasing altitude, the spallogenic radiation's distribution is starting

to spread out towards isotropic distribution, similar to the source radiation. Fit constants for the

latitudes and altitudes are presented in Appendix B. Fit constants are well behaved with

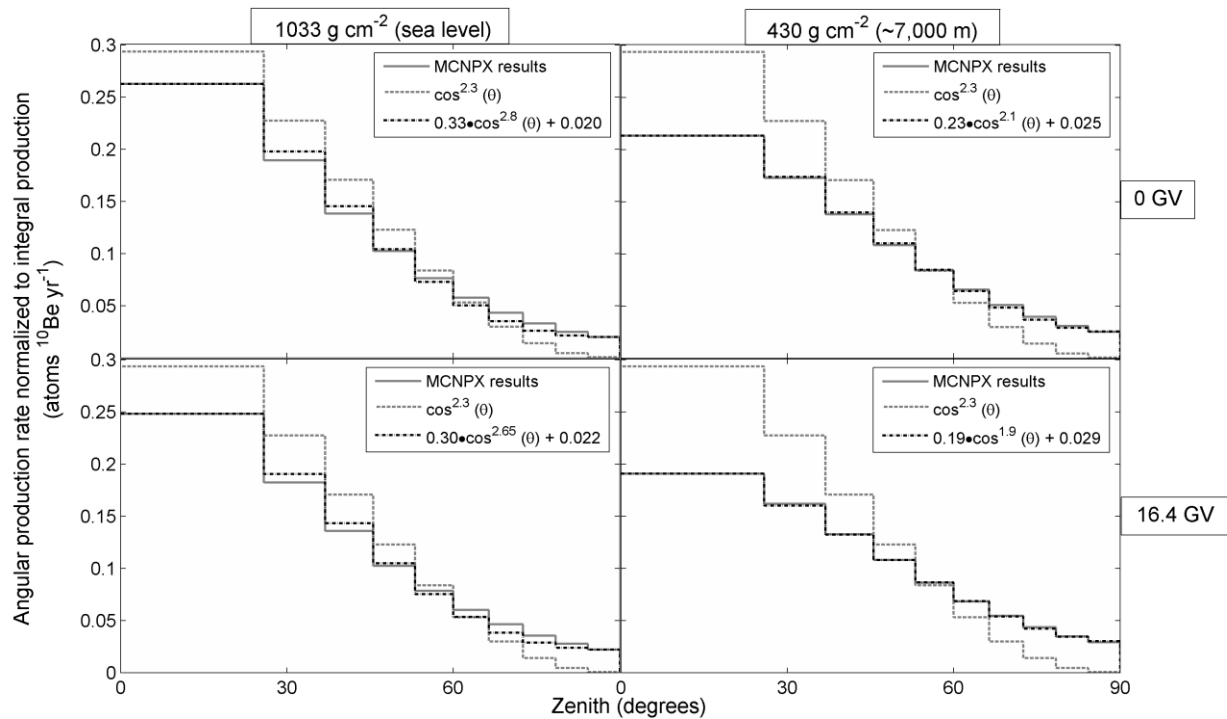monotonic growth or decay in both altitude and latitude dimensions.

Figure 4.4 – Comparison of results at four altitude-latitude points. The sea level results are more collimated than the high altitude results for both latitudes. Collimation also decreases with latitude, however, less strongly than with altitude.

## Subsurface production profiles in solid rock

Neutron and proton flux results from simulations of three different primary rock types were folded with cross sections to calculate production rate potentials for commonly used nuclides near the air-rock boundary. Production rate potentials generally have a slightly greater attenuation length in the rock than in air. While all calculated subsurface production rate potentials deviate slightly from exponential decrease, only the $^{36}$Cl from potassium pathway shows a significant "plateau" as described in Masarik & Reedy (1995) (see Figure 4.1 above and Figure 4.5 below).

Appendix C lists polynomials (Eq. 4.4) for the fit of the subsurface production rates in natural log space in the three rock types

$$P(z) = e^{(az^3 + bz^2 + cz + d)}$$   Eq. 4.4
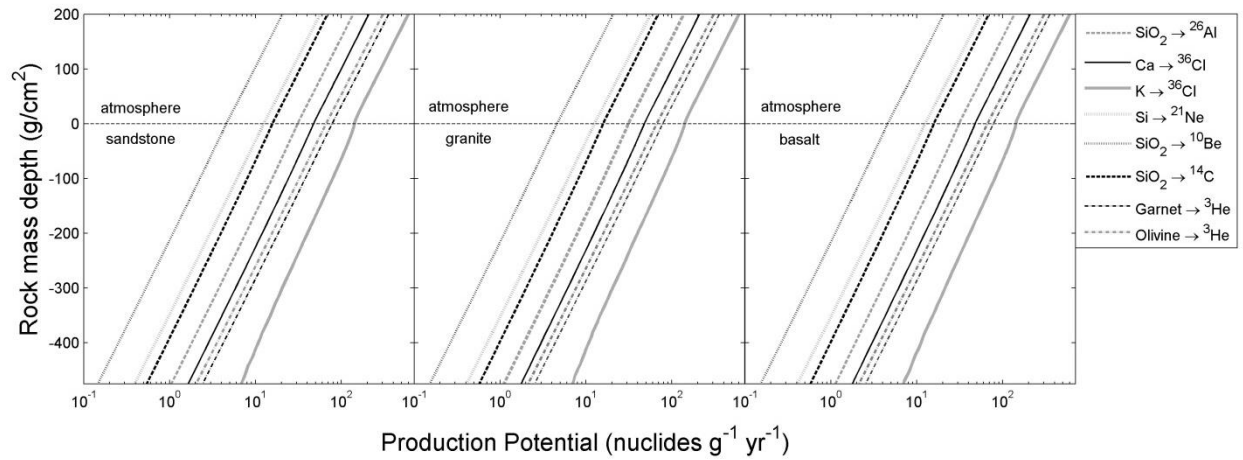
where z is depth in g/cm$^2$.



Figure 4.5 – Total production potential (neutrons and protons summed together) near the surface of rock types – sandstone, granite, and basalt. Note the slight change in slope of the curves with the inflection point being at the surface. For $^{10}$Be production in SiO$_2$ the attenuation length transitions from 133 g/cm$^2$ in air to 143 g/cm$^2$ in the upper portion of the sandstone. Also note the slight deviation from a simple exponential (straight line on a lin-log plot) near the surface, most obvious in the K(n or p,x)$^{36}$Cl reaction.

## DISCUSSION

### Altitude scaling

We find that the cosmic-ray radiation field in the atmosphere, even in the lower region, is not in equilibrium; the nucleonic component of the flux is still transitioning from a flux of protons and alpha particles propagating through space to a flux made up of neutrons and to a lesser extent a flux of protons propagating through air. We find the energy spectrum for neutrons and protons

changes throughout the atmosphere. The changing energy spectrum (Figure 4.1 above) folded

with the unique excitation function for each nuclide leads to a distinct altitude-latitude variation

for each nuclide. As a result, production ratios for each nuclide pair are also unique.

In Figure 4.6, we normalize our computed production ratios to sea level to investigate the

difference in production rate scaling between [10]Be and the other computed production rates.
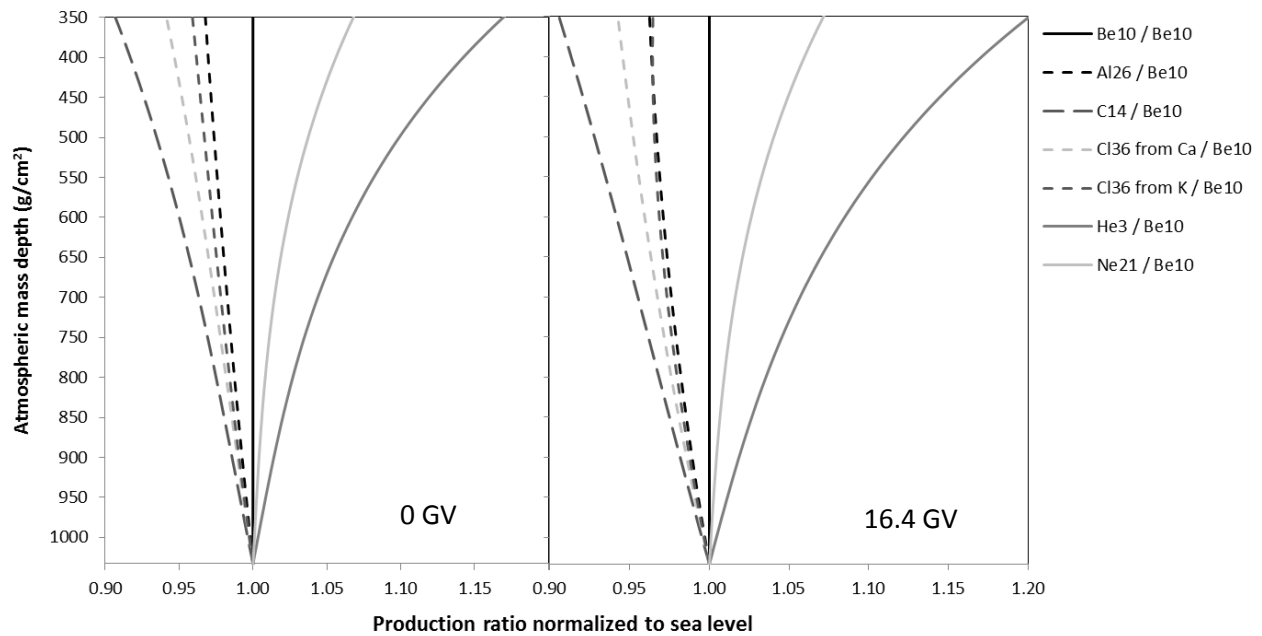


Figure 4.6 – Nuclide production rates as ratios to [10]Be production rates for high latitude (0 GV)
and low latitude (16.4 GV).

These normalized values of ratios can be used for correcting existing scaling schemes when

using nuclides other than [10]Be. The majority of scaling calibration data is based on [10]Be

concentrations, and no current scaling scheme considers nuclide specific scaling. Thus, if a

study relies on a nuclide other than [10]Be, these systematic errors can be avoided by utilizing

these ratio deviations as corrective factors.

**Angular production rate corrections**

The angular production results of our calculations generally follow the form of:

$$I(\theta, R_c, z) = A_{R_c,z} \cdot cos^{m_{R_c,z}}(\theta) + C_{R_c,z}$$

<div align="right">Eq. 4.5</div>

where θ is the zenith angle, 0° representing vertical and 90° horizontal, $R_c$ is the geomagnetic vertical cutoff in GV and z is altitude in g/cm$^2$. $A_{\lambda,z}$, $m_{\lambda,z}$ and $C_{\lambda,z}$ are the latitude and altitude dependent constants found in Appendix B. When determining the shielding correction to a sample, one would evaluate the integral for the angles not obscured:

$$F(\phi, \theta) = \int_{\phi_1}^{\phi_2} \int_{\theta_1}^{\theta_2} I(\theta, \lambda, z) \cdot \sin\theta \cdot d\theta \cdot d\phi$$

<div align="right">Eq. 4.6</div>

When evaluated, the function takes the form:

$$F(\phi, \theta) = \frac{A_{\lambda,z}}{m_{\lambda,z}+1} \left[ cos^{(m_{\lambda,z}+1)}(\theta_1) - cos^{(m_{\lambda,z}+1)}(\theta_2) \right] \cdot (C_{\lambda,z} \cdot (\theta_2 - \theta_1)) \cdot (\phi_2 - \phi_1)$$

<div align="right">Eq. 4.7</div>

The evaluated value $F$ is the factor by which the production rate has been modified.


**Subsurface production**

Similar to the phenomena seen in the atmosphere, the radiation field goes through another transition at the rock surface. This transition is dominated by the average atomic mass of the rock which affects the radiation field in two primary ways: 1) the average multiplicity in each spallation increases with average atomic mass; and 2) the average geometric cross section per atom rises in proportion to A$^{2/3}$. Thus, the average attenuation length in g/cm$^2$ tends to go up with increasing atomic mass.

The results support the form of the depth profile predicted by Masarik and Reedy (1995) but indicate a smaller magnitude. The only production profile that exhibits a flattened region near the surface is $^{36}$Cl from potassium. This is because the $K(n,x)^{36}$Cl cross section has a threshold of 1 MeV, considerably lower than the excitation functions of the other nuclides investigated. The cross section also has a substantial peak at 10 MeV, which is lower than the threshold of most cosmogenic nuclides and is within the energy range of evaporation nucleons produced more abundantly in rock.

In Table 4.2, we show the attenuation length calculated at the surface and at 400 g/cm$^2$ deep in the profile. These results suggest that current thickness and erosion correction calculations that assume a constant attenuation length contain small systematic errors. In all cases, the attenuation length is longer at the surface than 400 g/cm$^2$ down. Note that with few exceptions, the attenuation lengths go up with average atomic mass; sandstone being the lowest and basalt being the highest average atomic mass.

| | Sandstone | | Granite | | Basalt | |
|---|---|---|---|---|---|---|
| Mineral / nuclide | $\Lambda_0$ | $\Lambda_{400}$ | $\Lambda_0$ | $\Lambda_{400}$ | $\Lambda_0$ | $\Lambda_{400}$ |
| $SiO_2 \rightarrow {}^{26}Al$ | 149.6 | 138.1 | 153.4 | 140.0 | 154.6 | 142.1 |
| $Ca \rightarrow {}^{36}Cl$ | 152.4 | 139.0 | 156.9 | 141.8 | 158.6 | 143.1 |
| $K \rightarrow {}^{36}Cl$ | 184.8 | 172.6 | 180.2 | 168.2 | 189.9 | 170.0 |
| $SiO_2 \rightarrow {}^{21}Ne$ | 140.7 | 135.1 | 143.0 | 136.4 | 143.0 | 136.8 |
| $SiO_2 \rightarrow {}^{10}Be$ | 142.5 | 135.9 | 145.0 | 137.1 | 145.2 | 137.7 |
| $SiO_2 \rightarrow {}^{14}C$ | 150.8 | 138.6 | 154.5 | 140.4 | 155.5 | 141.6 |
| $Ca_3Al_2(SiO_4)_3 \rightarrow {}^3He$ | 140.5 | 135.0 | 142.9 | 136.4 | 143.1 | 137.0 |
| $MgFe(SiO_4) \rightarrow {}^3He$ | 139.5 | 134.5 | 141.7 | 135.9 | 142.0 | 136.4 |

Table 4.2 - Similar to the altitude scaling, a byproduct of each nuclide production profile having different attenuation lengths is changing production ratios. We calculate the subsurface production rate ratios for $^{26}Al/^{10}Be$ in the three different rock types to investigate the effect of different average atomic mass on production ratios (Figure 4.7).
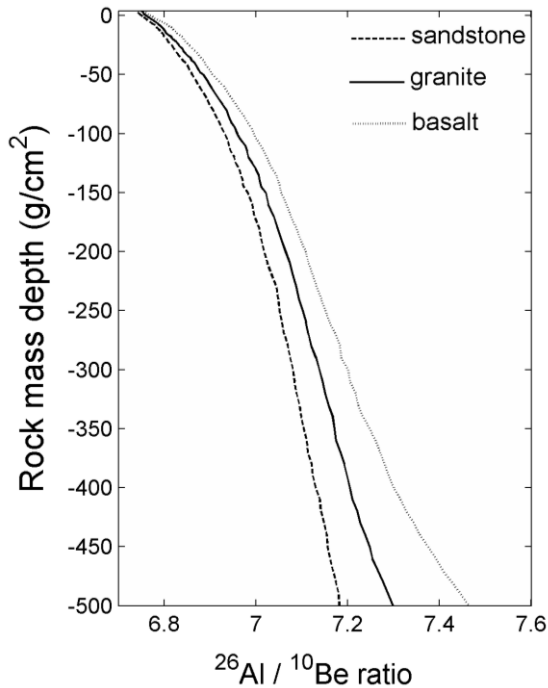
Figure 4.7 – Depth profile for $^{26}$Al/$^{10}$Be production ratios at high latitude for sandstone, granite and basalt. Surface is at sea level. Aluminum-26 production decreases with depth less rapidly than $^{10}$Be production in quartz , thus the ratio is increasing. This is the result of softening of the neutron and proton energy spectra and the $^{26}$Al production cross section being substantial in the lower energy range compared to the $^{10}$Be pathways.

In Figure 4.8, we take the subsurface production ratios and normalize them to their surface values. This provides a view of how much these ratios change with depth. The $^{36}$Cl from potassium pathway is substantially enhanced compared to other ratios. This enhancement may explain some of the variance in current estimates in $^{36}$Cl from potassium (Evans et al., 1997; Schimmelpfennig et al., 2011; Swanson and Caffee, 1999; Zreda et al., 1991).
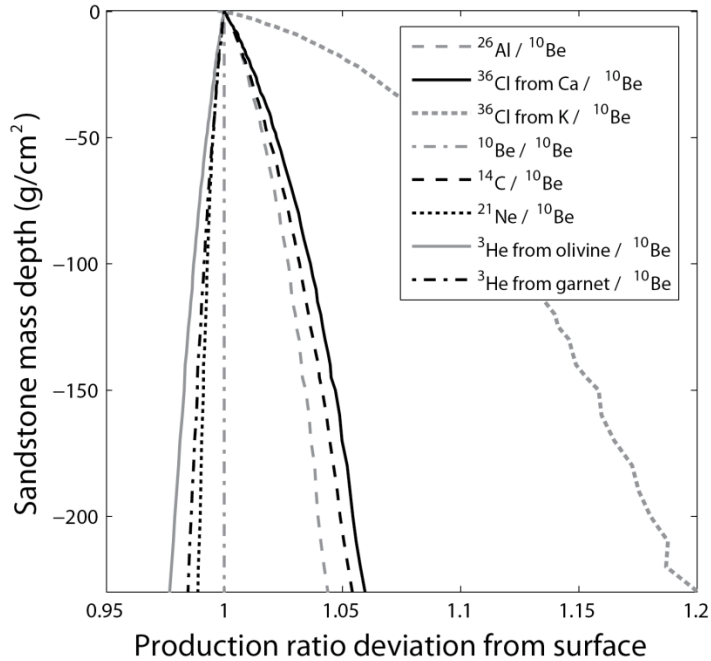
Figure 4.8 – Sandstone production rate ratios at high latitude
normalized to the surface. Curves represent the potential error
introduced into calculations when using nuclides other than $^{10}$Be.
The $^{36}$Cl from potassium is dramatically enhanced compared to $^{10}$Be
with depth.

We compare the normalized production ratio results from the three rock simulations in Figure

4.9. Focusing on all but the K→$^{36}$Cl production ratio, we see a general trend for the production

rate ratios that are greater than 1 to increase as average atomic mass increases. It is interesting to

note that the $^3$He in garnet and the $^{21}$Ne production ratios seem to be almost completely

unaffected by average atomic mass.

Figure 4.9 – A closer look at production rate ratios other than $^{36}$Cl (from K) / $^{10}$Be at high latitude normalized to the surface for sandstone, granite, and basalt. The basalt, with the higher average atomic weight show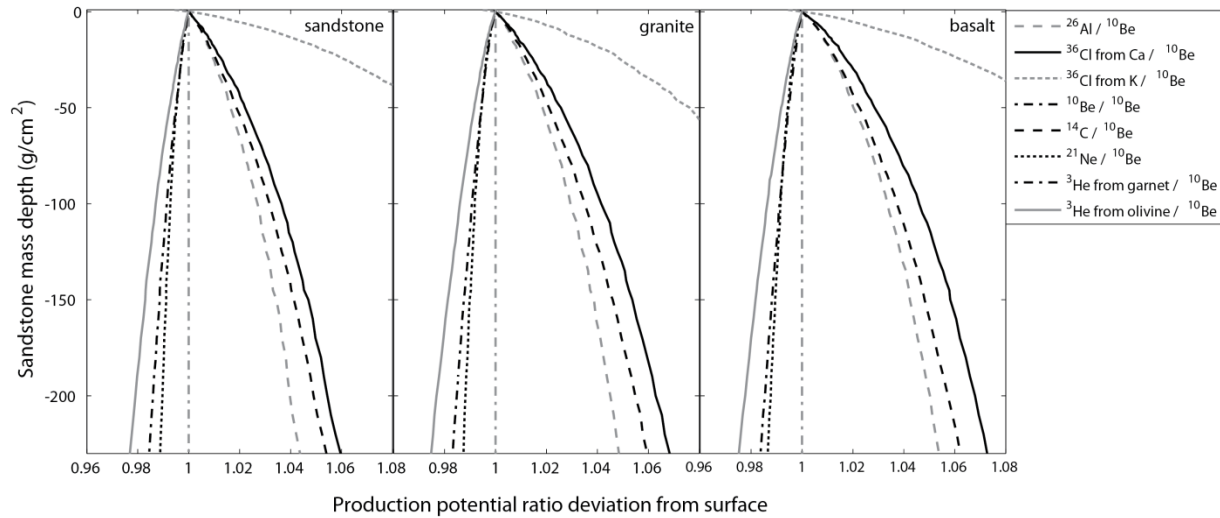s the greatest ratios. The three lower production ratios– the $^{3}$He (from garnet) / $^{10}$Be and $^{3}$He (from olivine) / $^{10}$Be and $^{21}$Ne are the result from cross sections that are even more strongly weighted to high energy particles.

# CONCLUSION

Using our physics-based production model, we have investigated three key aspects of

cosmogenic nuclide production rate systematics that have been difficult to address with natural

calibration. We find that production scales uniquely in altitude and latitude for each of the

nuclides investigated. We have provided parameterized fits for seven commonly used nuclides.

These parameterized scaling functions can also be used to determine production ratios as

functions of altitude and latitude. Angular distribution of nuclide-producing particles has been

investigated. We find the distribution to be significantly different from the standard method for

shielding correction using $\cos^{2.3}(\theta)$. Our results consistently indicate a significant portion of

production coming from near-horizontal particles. This indicates a pervasive systematic error in

cosmogenic nuclide methods exists due to not properly accounting for low-angle horizon

shielding. In addition, the distribution broadens with altitude and decreasing latitude. We

present a new format for shielding corrections and constants for a range of altitudes and latitudes. Subsurface production rates are also investigated to address the uncertainty in the production rate profile. We find nuclide specific profiles which all exhibit changing attenuation lengths with depth. For all nuclides, the attenuation length at the surface is longer than that at moderate depths. Attenuation lengths also increase with average atomic mass.

# APPENDIX A – Polynomial fit for production rates as functions of altitude

Polynomial fits were determined by minimizing the root-mean-square- error in log space.

$SiO_2 \rightarrow {}^{26}Al$
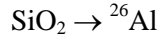
|         | a         | b         | c        | d        |
|---------|-----------|-----------|----------|----------|
| 0 GV    | -5.31E-10 | -2.67E-07 | 7.55E-03 | 3.41E+00 |
| 1.2 GV  | -4.88E-10 | -3.11E-07 | 7.54E-03 | 3.39E+00 |
| 2.0 GV  | -6.62E-10 | -2.03E-07 | 7.47E-03 | 3.38E+00 |
| 3.3 GV  | -7.97E-10 | -2.92E-07 | 7.41E-03 | 3.31E+00 |
| 4.5 GV  | -9.18E-10 | -3.31E-07 | 7.32E-03 | 3.24E+00 |
| 6.4 GV  | -9.35E-10 | -4.10E-07 | 7.14E-03 | 3.09E+00 |
| 8.7 GV  | -9.38E-10 | -4.85E-07 | 7.00E-03 | 2.90E+00 |
| 11.2 GV | -9.45E-10 | -5.14E-07 | 6.87E-03 | 2.71E+00 |
| 14.0 GV | -9.77E-10 | -5.09E-07 | 6.75E-03 | 2.51E+00 |
| 16.4 GV | -1.00E-09 | -4.87E-07 | 6.68E-03 | 2.37E+00 |

Table 4.A1 – $^{26}Al$ from $SiO_2$

$SiO_2 \rightarrow {}^{10}Be$
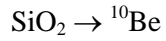
|         | a         | b         | c        | d        |
|---------|-----------|-----------|----------|----------|
| 0 GV    | -4.14E-10 | -3.08E-07 | 7.61E-03 | 1.50E+00 |
| 1.2 GV  | -3.79E-10 | -3.42E-07 | 7.60E-03 | 1.48E+00 |
| 2.0 GV  | -4.89E-10 | -3.11E-07 | 7.57E-03 | 1.46E+00 |
| 3.3 GV  | -6.74E-10 | -3.05E-07 | 7.47E-03 | 1.41E+00 |
| 4.5 GV  | -7.91E-10 | -3.44E-07 | 7.38E-03 | 1.34E+00 |
| 6.4 GV  | -7.95E-10 | -4.51E-07 | 7.23E-03 | 1.19E+00 |
| 8.7 GV  | -8.21E-10 | -4.98E-07 | 7.08E-03 | 1.02E+00 |
| 11.2 GV | -8.23E-10 | -5.36E-07 | 6.95E-03 | 8.27E-01 |
| 14.0 GV | -8.57E-10 | -5.38E-07 | 6.84E-03 | 6.36E-01 |
| 16.4 GV | -8.56E-10 | -5.51E-07 | 6.78E-03 | 4.89E-01 |

Table 4.A2 – $^{10}Be$ from $SiO_2$

$SiO_2 \rightarrow {}^{14}C$
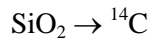
|         | a         | b         | c        | d        |
|---------|-----------|-----------|----------|----------|
| 0 GV    | -6.38E-10 | -2.60E-07 | 7.50E-03 | 2.73E+00 |
| 1.2 GV  | -6.12E-10 | -2.85E-07 | 7.49E-03 | 2.72E+00 |
| 2.0 GV  | -7.17E-10 | -2.70E-07 | 7.45E-03 | 2.69E+00 |
| 3.3 GV  | -8.86E-10 | -3.03E-07 | 7.36E-03 | 2.63E+00 |
| 4.5 GV  | -9.88E-10 | -3.53E-07 | 7.26E-03 | 2.56E+00 |
| 6.4 GV  | -9.92E-10 | -4.36E-07 | 7.09E-03 | 2.40E+00 |
| 8.7 GV  | -9.96E-10 | -5.03E-07 | 6.95E-03 | 2.21E+00 |
| 11.2 GV | -9.99E-10 | -5.31E-07 | 6.81E-03 | 2.01E+00 |

| | a | b | c | d |
|---|---|---|---|---|
| 14.0 GV | -1.03E-09 | -5.28E-07 | 6.70E-03 | 1.81E+00 |
| 16.4 GV | -1.02E-09 | -4.78E-07 | 6.65E-03 | 2.78E+00 |

Table 4.A3 – $^{14}$C from $SiO_2$

$Ca \rightarrow {}^{36}Cl$
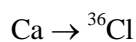
| | a | b | c | d |
|---|---|---|---|---|
| 0 GV | -5.80E-10 | -2.60E-07 | 7.52E-03 | 3.83E+00 |
| 1.2 GV | -5.42E-10 | -2.97E-07 | 7.52E-03 | 3.82E+00 |
| 2.0 GV | -6.80E-10 | -2.32E-07 | 7.46E-03 | 3.80E+00 |
| 3.3 GV | -8.24E-10 | -2.99E-07 | 7.39E-03 | 3.74E+00 |
| 4.5 GV | -9.30E-10 | -3.49E-07 | 7.29E-03 | 3.66E+00 |
| 6.4 GV | -9.52E-10 | -4.14E-07 | 7.12E-03 | 3.51E+00 |
| 8.7 GV | -9.49E-10 | -4.90E-07 | 6.98E-03 | 3.32E+00 |
| 11.2 GV | -9.51E-10 | -5.23E-07 | 6.85E-03 | 3.12E+00 |
| 14.0 GV | -9.85E-10 | -5.12E-07 | 6.73E-03 | 2.93E+00 |
| 16.4 GV | -1.02E-09 | -4.78E-07 | 6.65E-03 | 2.78E+00 |

Table 4.A4 – $^{36}$Cl from Ca

$K \rightarrow {}^{36}Cl$
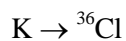
| | a | b | c | d |
|---|---|---|---|---|
| 0 GV | -5.06E-10 | -2.95E-07 | 7.54E-03 | 4.89E+00 |
| 1.2 GV | -4.80E-10 | -3.22E-07 | 7.53E-03 | 4.87E+00 |
| 2.0 GV | -5.86E-10 | -3.02E-07 | 7.50E-03 | 4.85E+00 |
| 3.3 GV | -7.76E-10 | -3.03E-07 | 7.40E-03 | 4.80E+00 |
| 4.5 GV | -8.92E-10 | -3.42E-07 | 7.30E-03 | 4.72E+00 |
| 6.4 GV | -8.98E-10 | -4.36E-07 | 7.14E-03 | 4.57E+00 |
| 8.7 GV | -9.25E-10 | -4.72E-07 | 6.99E-03 | 4.38E+00 |
| 11.2 GV | -9.40E-10 | -4.89E-07 | 6.85E-03 | 4.19E+00 |
| 14.0 GV | -9.51E-10 | -5.08E-07 | 6.74E-03 | 3.99E+00 |
| 16.4 GV | -9.41E-10 | -5.30E-07 | 6.69E-03 | 3.85E+00 |

Table 4.A5 – $^{36}$Cl from K

$SiO_2 \rightarrow {}^{21}Ne$
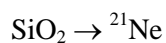
| | a | b | c | d |
|---|---|---|---|---|
| 0 GV | -3.44E-10 | -3.26E-07 | 7.64E-03 | 2.50E+00 |
| 1.2 GV | -3.02E-10 | -3.65E-07 | 7.63E-03 | 2.49E+00 |
| 2.0 GV | -4.26E-10 | -3.21E-07 | 7.60E-03 | 2.47E+00 |
| 3.3 GV | -6.47E-10 | -2.90E-07 | 7.50E-03 | 2.42E+00 |
| 4.5 GV | -7.85E-10 | -3.19E-07 | 7.41E-03 | 2.35E+00 |
| 6.4 GV | -7.89E-10 | -4.36E-07 | 7.26E-03 | 2.21E+00 |
| 8.7 GV | -8.24E-10 | -4.76E-07 | 7.11E-03 | 2.03E+00 |
| 11.2 GV | -8.23E-10 | -5.19E-07 | 6.98E-03 | 1.84E+00 |

| | | | | |
|---|---|---|---|---|
| 14.0 GV | -8.58E-10 | -5.23E-07 | 6.87E-03 | 1.65E+00 |
| 16.4 GV | -8.65E-10 | -5.28E-07 | 6.80E-03 | 1.51E+00 |

Table 4.A6 – $^{21}$Ne from $SiO_2$

$SiO_4 \rightarrow {}^3He$
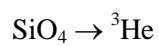
| | a | b | c | d |
|---|---|---|---|---|
| 0 GV | -2.04E-10 | -3.35E-07 | 7.71E-03 | 4.51E+00 |
| 1.2 GV | -1.60E-10 | -3.78E-07 | 7.71E-03 | 4.50E+00 |
| 2.0 GV | -2.85E-10 | -3.13E-07 | 7.67E-03 | 4.48E+00 |
| 3.3 GV | -4.85E-10 | -2.90E-07 | 7.59E-03 | 4.44E+00 |
| 4.5 GV | -6.37E-10 | -3.03E-07 | 7.50E-03 | 4.38E+00 |
| 6.4 GV | -6.48E-10 | -4.25E-07 | 7.36E-03 | 4.24E+00 |
| 8.7 GV | -6.77E-10 | -4.74E-07 | 7.21E-03 | 4.07E+00 |
| 11.2 GV | -6.85E-10 | -5.13E-07 | 7.08E-03 | 3.89E+00 |
| 14.0 GV | -7.18E-10 | -5.22E-07 | 6.97E-03 | 3.70E+00 |
| 16.4 GV | -7.25E-10 | -5.28E-07 | 6.91E-03 | 3.56E+00 |

Table 4.A7 – $^3$He from $SiO_4$

## APPENDIX B - Angular distribution fit constants for:

$$A \cdot \cos^m(\theta) + b$$

Polynomial fits were determined by minimizing the root-mean-square- error.

| Altitude (g/cm²) | 0 GV | 1.2 GV | 3.3 GV | 4.5 GV | 6.4 GV | 8.7 GV | 11.2 GV | 14.0 GV | 16.4 GV |
|---|---|---|---|---|---|---|---|---|---|
| 0 | 2.80E+00 | 2.80E+00 | 2.80E+00 | 2.75E+00 | 2.70E+00 | 2.70E+00 | 2.65E+00 | 2.65E+00 | 2.65E+00 |
| 100 | 2.70E+00 | 2.75E+00 | 2.75E+00 | 2.65E+00 | 2.65E+00 | 2.60E+00 | 2.60E+00 | 2.60E+00 | 2.60E+00 |
| 200 | 2.65E+00 | 2.65E+00 | 2.65E+00 | 2.60E+00 | 2.55E+00 | 2.55E+00 | 2.50E+00 | 2.50E+00 | 2.50E+00 |
| 300 | 2.55E+00 | 2.55E+00 | 2.55E+00 | 2.50E+00 | 2.45E+00 | 2.45E+00 | 2.40E+00 | 2.40E+00 | 2.40E+00 |
| 400 | 2.45E+00 | 2.45E+00 | 2.45E+00 | 2.35E+00 | 2.35E+00 | 2.30E+00 | 2.30E+00 | 2.25E+00 | 2.25E+00 |
| 500 | 2.30E+00 | 2.30E+00 | 2.30E+00 | 2.20E+00 | 2.15E+00 | 2.15E+00 | 2.10E+00 | 2.10E+00 | 2.10E+00 |
| 600 | 2.10E+00 | 2.10E+00 | 2.10E+00 | 2.00E+00 | 1.95E+00 | 1.95E+00 | 1.90E+00 | 1.90E+00 | 1.90E+00 |

Table 4.B1 – m values for angular distribution fit

| Altitude (g/cm2) | 0 GV | 1.2 GV | 3.3 GV | 4.5 GV | 6.4 GV | 8.7 GV | 11.2 GV | 14.0 GV | 16.4 GV |
|---|---|---|---|---|---|---|---|---|---|
| 0 | -3.29E-01 | -3.29E-01 | -3.26E-01 | -3.19E-01 | -3.11E-01 | -3.08E-01 | -3.02E-01 | -3.00E-01 | -2.99E-01 |
| 100 | -3.17E-01 | -3.19E-01 | -3.17E-01 | -3.07E-01 | -3.01E-01 | -2.94E-01 | -2.92E-01 | -2.90E-01 | -2.89E-01 |
| 200 | -3.07E-01 | -3.07E-01 | -3.05E-01 | -2.95E-01 | -2.88E-01 | -2.83E-01 | -2.79E-01 | -2.76E-01 | -2.75E-01 |
| 300 | -2.93E-01 | -2.93E-01 | -2.90E-01 | -2.80E-01 | -2.72E-01 | -2.68E-01 | -2.63E-01 | -2.60E-01 | -2.59E-01 |
| 400 | -2.76E-01 | -2.76E-01 | -2.73E-01 | -2.60E-01 | -2.55E-01 | -2.48E-01 | -2.45E-01 | -2.40E-01 | -2.38E-01 |
| 500 | -2.54E-01 | -2.55E-01 | -2.52E-01 | -2.37E-01 | -2.30E-01 | -2.25E-01 | -2.20E-01 | -2.17E-01 | -2.15E-01 |
| 600 | -2.27E-01 | -2.27E-01 | -2.24E-01 | -2.08E-01 | -2.00E-01 | -1.96E-01 | -1.90E-01 | -1.88E-01 | -1.86E-01 |

Table 4.B2 – A values for angular distribution fit

| Altitude (g/cm²) | 0 GV | 1.2 GV | 3.3 GV | 4.5 GV | 6.4 GV | 8.7 GV | 11.2 GV | 14.0 GV | 16.4 GV |
|---|---|---|---|---|---|---|---|---|---|
| 0 | 1.96E-02 | 1.96E-02 | 2.06E-02 | 2.02E-02 | 2.09E-02 | 2.12E-02 | 2.16E-02 | 2.18E-02 | 2.20E-02 |
| 100 | 2.03E-02 | 2.03E-02 | 2.08E-02 | 2.08E-02 | 2.14E-02 | 2.21E-02 | 2.22E-02 | 2.25E-02 | 2.26E-02 |
| 200 | 2.07E-02 | 2.09E-02 | 2.09E-02 | 2.17E-02 | 2.23E-02 | 2.28E-02 | 2.30E-02 | 2.33E-02 | 2.34E-02 |
| 300 | 2.11E-02 | 2.13E-02 | 2.19E-02 | 2.25E-02 | 2.28E-02 | 2.35E-02 | 2.38E-02 | 2.40E-02 | 2.43E-02 |
| 400 | 2.24E-02 | 2.22E-02 | 2.27E-02 | 2.34E-02 | 2.41E-02 | 2.46E-02 | 2.50E-02 | 2.54E-02 | 2.56E-02 |
| 500 | 2.33E-02 | 2.32E-02 | 2.38E-02 | 2.48E-02 | 2.53E-02 | 2.63E-02 | 2.64E-02 | 2.68E-02 | 2.70E-02 |
| 600 | 2.48E-02 | 2.46E-02 | 2.51E-02 | 2.67E-02 | 2.75E-02 | 2.82E-02 | 2.85E-02 | 2.87E-02 | 2.92E-02 |

Table 4.B3 – C values for angular distribution fit

# APPENDIX C – Polynomial constants for subsurface production rates at high latitudes

Polynomial fits were determined by minimizing the root-mean-square- error in log space.

| Mineral / nuclide | a | b | c | d |
|---|---|---|---|---|
| $SiO_2 \rightarrow {}^{26}Al$ | 1.509e-9 | -1.606e-6 | -6.683e-3 | 3.425 |
| $Ca \rightarrow {}^{36}Cl$ | 1.927e-9 | -1.949e-6 | -6.561e-3 | 3.853 |
| $K \rightarrow {}^{36}Cl$ | 1.065e-8 | -6.870e-6 | -5.411e-3 | 4.963 |
| $SiO_2 \rightarrow {}^{21}Ne$ | 5.247e-11 | -3.945e-7 | -7.109e-3 | 2.517 |
| $SiO_2 \rightarrow {}^{10}Be$ | 4.004e-10 | -6.633e-7 | -7.019e-3 | 1.515 |
| $SiO_2 \rightarrow {}^{14}C$ | 1.507e-9 | -1.632e-6 | -6.632e-3 | 2.750 |
| $Ca_3Al_2(SiO_4)_3 \rightarrow {}^{3}He$ | 1.769e-10 | -4.690e-7 | -7.119e-3 | 4.347 |
| $MgFe(SiO_4) \rightarrow {}^{3}He$ | 5.052e-11 | -3.580e-7 | -7.171e-3 | 4.187 |

Table 4.C1 – polynomial values for sandstone ($SiO_2$) in log space

| Mineral / nuclide | a | b | c | d |
|---|---|---|---|---|
| $SiO_2 \rightarrow {}^{26}Al$ | 1.865e-9 | -1.899e-6 | -6.520e-3 | 3.433 |
| $Ca \rightarrow {}^{36}Cl$ | 2.455e-9 | -2.324e-6 | -6.373e-3 | 3.862 |
| $K \rightarrow {}^{36}Cl$ | 8.834e-9 | -5.795e-6 | -5.548e-3 | 4.954 |
| $SiO_2 \rightarrow {}^{21}Ne$ | 2.285e-10 | -5.551e-7 | -6.995e-3 | 2.522 |
| $SiO_2 \rightarrow {}^{10}Be$ | 5.952e-10 | -8.528e-7 | -6.895e-3 | 1.520 |
| $SiO_2 \rightarrow {}^{14}C$ | 1.810e-9 | -1.898e-6 | -6.472e-3 | 2.758 |
| $Ca_3Al_2(SiO_4)_3 \rightarrow {}^{3}He$ | 4.110e-10 | -6.598e-7 | -7.000e-3 | 4.352 |
| $MgFe(SiO_4) \rightarrow {}^{3}He$ | 2.796e-10 | -5.420e-7 | -7.057e-3 | 4.192 |

Table 4.C2 – polynomial values for granite in log space

| Mineral / nuclide | a | b | c | d |
|---|---|---|---|---|
| $SiO_2 \rightarrow {}^{26}Al$ | 2.388e-9 | -2.143e-6 | -6.467e-3 | 3.431 |
| $Ca \rightarrow {}^{36}Cl$ | 3.018e-9 | -2.661e-6 | -6.306e-3 | 3.860 |
| $K \rightarrow {}^{36}Cl$ | 1.026e-8 | -6.928e-6 | -5.265e-3 | 4.971 |
| $SiO_2 \rightarrow {}^{21}Ne$ | 3.157e-10 | -5.910e-7 | -6.991e-3 | 2.518 |
| $SiO_2 \rightarrow {}^{10}Be$ | 7.160e-10 | -8.988e-7 | -6.886e-3 | 1.516 |
| $SiO_2 \rightarrow {}^{14}C$ | 2.205e-9 | -2.111e-6 | -6.430e-3 | 2.755 |
| $Ca_3Al_2(SiO_4)_3 \rightarrow {}^{3}He$ | 5.556e-10 | -7.276e-7 | -6.986e-3 | 4.349 |
| $MgFe(SiO_4) \rightarrow {}^{3}He$ | 3.985e-10 | -5.968e-7 | -7.044e-3 | 4.188 |

Table 4.C3 – polynomial values for basalt in log space

# REFERENCES

Amidon, W.H., Farley, K.A., Burbank, D.W., Pratt-Sitaula, B., 2008. Anomalous cosmogenic 3He production and elevation scaling in the high Himalaya. Earth and Planetary Science Letters 265, 287-301.

Argento, D.C., Reedy, R.C., Stone, J.O., 2013. Modeling the earth's cosmic radiation. Nuclear Instruments and Methods B 294, 464-469.

Barford, N.C., Davis, G., 1952. The Angular Distribution and Attenuation of the Star-Producing Component of Cosmic Rays. Proceedings of the Royal Society of London. Series A, Mathematical and Physical Sciences 214, 225-237.

Conversi, N.C., Rothwell, P., 1954. Angular Distributions in Cosmic Ray Stars at 3500 Meters. Il Nuovo Cimento 12, 191-210.

Desilets, D., Zreda, M.G., 2003. Spatial and temporal distribution of secondary cosmic-ray nucleon intensities and applications to in situ cosmogenic dating. Earth and Planetary Science Letters 206, 21-42.

Dunai, T.J., 2001. Infuence of secular variation of the geomagnetic field on production rates of in situ produced cosmogenic nuclides. Earth and Planetary Science Letters 193, 197-212.

Dunai, T.J., 2010. Cosmogenic nuclides: principles, concepts and applications in the Earth Surface Sciences, First ed. Cambridge University Press, Cambridge.

Evans, J.M., Stone, J., Fifield, L.K., Cresswell, R.G., 1997. Cosmogenic chlorine-36 production in K-feldspar. Nuclear Instruments and Methods 123, 334-340.

Gayer, E., Pik, R., Lave, J., France-Lanourd, C., Bourles, D.L., Marty, B., 2004. Cosmogenic 3He in Himalayan garnets indicating an altitude dependence of the 3He/10Be production ratio. Earth and Planetary Science Letters 229, 91-104.

Gosse, J., Phillips, F., 2001. Terrestrial in situ cosmogenic nuclides: theory and application. Quaternary Science Reviews 20, 1475-1560.

Heidbreder, E., Pinkau, K., Reppin, C., Schonfelder, V., 1970. A balloon borne detector to determine high energy neutrons in energy and directions. Nuclear Instruments and Methods 88, 137-147.

Heidbreder, E., Pinkau, K., Reppin, C., Schönfelder, V., 1971. Measurements of the Distribution in Energy and Angle of High-Energy Neutrons in the Lower Atmosphere. Journal of Geophysical Research 76, 2905-2916.

Kubik, P.W., Reuther, A.U., 2007. Attenuation of cosmogenic 10Be production in the first 20 cm below a rock surface. Nuclear Instruments and Methods B 259, 616-624.

Lal, D., 1991. Cosmic-ray labeling of erosion surfaces: in situ nuclide production rates and erosion models. Earth and Planetary Science Letters 104, 424-439.

Lal, D., Malhotra, P.K., Peters, B., 1958. On the production of radioisotopes in the atmosphere by cosmic radiation and their application to meteorology. Journal of Atmospheric and Terrestrial Physics 12, 306-328.

Lifton, N.A., Smart, D.F., Shea, M.A., 2008. Scaling time-integrated in situ cosmogenic nuclide production rates using a continuous geomagnetic model. Earth and Planetary Science Letters 268, 190-201.

Masarik, J., Reedy, R.C., 1995. Terrestrial cosmogenic-nuclide production systematics calculated from numerical simulations. Earth and Planetary Science Letters 136, 381-395.

Nishiizumi, K., Winterer, E.L., Kohl, C.P., Klein, J., Middleton, R., Lal, D., Arnold, J.R., 1989. Cosmic Ray Production Rates of 10Be and 26Al in Quartz from Glacially polished Rocks. Journal of Geophysical Research 94, 17,907-917,915.

O'Brien, K., 2008. Limitations of the Use of the Vertical Cut-off to Calculate Cosmic-ray Propogation in the Earth's Atmosphere. Radiation Protection Dosimetry 128, 259-260.

Reedy, R.C., 2013. Cosmogenic-Nuclide production rates: reaction cross section update. Nuclear Instruments and Methods B 294, 470-474.

Schimmelpfennig, I., Williams, A., Pik, R., Burnard, P., Niederman, S., Finkel, R., Schneider, B., Benedetti, L., 2011. Inter-comparison of cosmogenic in-situ 3He, 21Ne and 36Cl at low latitude along an altitude transect on the SE slope of Kilimanjaro volcano (3S, Tanzania). Quaternary Geochronology 6, 425-436.

Swanson, T., Caffee, M., 1999. Determination of Cl-36 Production Rates Derived from the Well-Dated Deglaciation Surfaces of Whidbey and Fidalgo Island, Washington. Quaternary Research 56, 366-382.

Usoskin, I.G., Kovaltsov, G.A., 2006. Cosmic ray induced ionization in the atmosphere: Full modeling and practical applications. Journal of Geophysical Research 111, 1-9.

Zreda, M.G., Phillips, F.M., Elmore, D., Kubik, P.W., Sharma, P., Dorn, R.I., 1991. COSMOGENIC CL-36 PRODUCTION-RATES IN TERRESTRIAL ROCKS. Earth and Planetary Science Letters 105, 94-109.

Chapter 5



Chlorine-36 in the oceans: sources and significance

# ABSTRACT

We present measurements of $^{36}$Cl/Cl ratios in several seawater samples, and sea-salts and fossil salt. The average $^{36}$Cl/Cl ratio of the seawater samples is $7.1 \pm 0.9 \times 10^{-16}$. We have performed several radiation transport simulations of cosmic-rays in the atmosphere and oceans where the bulk of $^{36}$Cl is produced. Simulation results of the current geomagnetic field sum to 22 g of $^{36}$Cl per year which translates to a steady state $^{36}$Cl/Cl ratio of $3.6 \times 10^{-16}$.
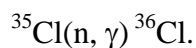
# INTRODUCTION

The radioisotope chlorine-36 ($^{36}$Cl) is produced in the earth's atmosphere and at its surface by cosmic rays. Since the earth's surface is 71% ocean, the bulk of this $^{36}$Cl is either produced in or deposited on the ocean surface, while most of that deposited on land in rainfall will also find its way to the ocean. Hence the oceans are the repository of essentially the complete inventory of the earth's $^{36}$Cl. The inventory is then a measure of either the average cosmic ray flux over the past ~1 million years, weighted by the 301,000 year half-life of $^{36}$Cl, or of the cross sections of the nuclear reactions that produce the radioisotope. In this work, we report a measurement of the $^{36}$Cl/Cl ratio in the ocean, and compare this with other measures of $^{36}$Cl production and with the predictions of physics-based models.

There are two principal mechanisms for the natural production of $^{36}$Cl. First, it is produced in the atmosphere via the spallation of argon-40 ($^{40}$Ar) and argon-36 ($^{36}$Ar) by energetic secondary cosmic-rays (Phillips, 2000). This component falls out in rainfall, either directly on the ocean surface, or on land from where it finds its way to the ocean in rivers. The second mechanism is the production of $^{36}$Cl via neutron capture by stable $^{35}$Cl, which constitutes 75% of the chloride in the oceans, i.e.:

$$^{35}Cl + n \rightarrow {}^{36}Cl + \gamma,$$
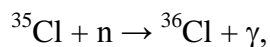
which can also be expressed as:

$$^{35}Cl(n, \gamma)\,^{36}Cl.$$

Other contributions such as *in-situ* production in surface rocks, nuclear weapons testing, and discharges from nuclear power plants and reprocessing facilities are found to be negligible.

Since the oceans have a mixing time of $\sim 10^3$ yr (Murray, 1992) that is short compared to $^{36}Cl$ half-life of $3.01 \times 10^5$ yr, and since the residence time of chloride in the oceans is on the order of $\sim 4 \times 10^9$ years (Berner and Berner, 1987), the $^{36}Cl$ inventory should be well-mixed. Hence the $^{36}Cl/Cl$ ratio should be uniform throughout the oceans. A consequence of the very large amount of chloride in the oceans is, however, that the $^{36}Cl/Cl$ ratio is very low, $\leq 10^{-15}$, the measurement of which poses a significant analytical challenge (Argento et al., 2010; Fifield et al., 2013).

An early attempt to measure the $^{36}Cl/Cl$ ratio of seawater was able to set only an upper limit of $< 4 \times 10^{-15}$ (Finkel et al., 1980). More recently, (Galindo-Uribarri et al., 2007) reported measurements on three samples with values ranging from 1 to $50 \times 10^{-15}$. In contrast, in a precursor to the present work, (Fifield et al., 2013) found significantly lower ratios $\sim 7 \times 10^{-16}$.

Neutron monitors have provided extensive data on cosmic-ray flux at the surface of the earth, the cosmic-ray flux history within the atmosphere is less well constrained. In addition, the history of the geomagnetic field and the nuclear reaction cross sections are still being assessed to yield a more accurate cosmic-ray flux history. While carbon-14 has received considerable study due to its extensive use in dating archeological objects and Pleistocene geomorphic processes (Castagnoli and Lal, 1980; Lal, 1988; Lal et al., 1958; Libby, 1946), the production rate as a function of time is still being assessed (Kovaltsov et al., 2012; Masarik and Beer, 2009; O'Brien, 1979). Meteoric $^{36}Cl$ production rates are also somewhat unconstrained (Masarik and Beer, 1999; Phillips, 2000) which limits its use as a hydrological tracer.

Earlier attempts to estimate the overall production rate of the isotope in the atmosphere include numerous studies of $^{36}$Cl in rainwater - (Finkel et al., 1980): ($29 \times 10^{-15}$), (Kneis et al., 1994): ($40 \times 10^{-15}$ to $400 \times 10^{-15}$), (Herut et al., 1992): ($1.8 \times 10^{-15}$ to $50 \times 10^{-15}$), but temporal and regional variability is large, making these studies difficult to interpret (Keywood et al., 1998). Attempts using purely physics based models (Huggle et al., 1996; Lal and Peters, 1967; Masarik and Beer, 2009; Oeschger et al., 1969; Parrat et al., 1996a; Parrat et al., 1996b) have also been limited because of the difficulty in comparing integrated production rates with regional measurements. This study provides a crucial set of data to bridge the two methods. Because the ocean's $^{36}$Cl derives from all latitudes, and chloride is so retentive, these measurements provide a global production integrated across latitude, through seasons and solar cycles.

Oceanic $^{36}$Cl differs from other cosmic-ray proxies because of its integrated and signal and insensitivity to spatial and temporal fluctuations. For instance, the bulk of meteoric cosmogenic nuclides production occurs in the stratosphere. However, the injection of these nuclides are irregular and postulated to be unevenly distributed between the two hemispheres (Keywood et al., 1998). Radiocarbon has the added complexity of reservoir effects. However, unlike ice core records and tree rings, this data set will not yield temporal records.

To investigate the production processes responsible for the majority of $^{36}$Cl, we have developed a terrestrial cosmic-ray model for estimating the production of $^{36}$Cl in the atmosphere and the oceans as shown in Chapter 2 and 3 (Argento et al., 2013). Using MCNPX to simulate the comic-ray radiation cascade throughout the atmosphere and in the oceans, we fold the neutron

and proton flux with cross sections for argon (Reedy, 2013) and chlorine (Guber et al., 2004) to calculate column integrated production rates.

## SAMPLES

For this initial study, five samples of seawater taken at 42ºN, 152ºW in the Pacific Ocean were obtained.  The samples were collected in 2006 by the R/V Thomas G. Thompson on the CLIVAR P16N repeat hydrography cruise, in a vertical column at depths of 5m, 1900m, 2875m, 4200m (prepared into two separate samples) and 5000m.  The range of depths allows chloride from different water masses and ventilation ages to be sampled.  Salinity ranges from 33.05‰ in the surface sample to 34.69‰ at 5000m (http://cdiac.ornl.gov/ftp/oceans/p16nwoce/).

Another sample was obtained from the Strait of Juan De Fuca, Washington, USA at 48º 09′ 57.7″N and 123º 42′ 23.3″ W.  The sample was taken near 5 meters depth.  Two commercially available sea salts, two standard table salts, and a commercially available rock salt were dissolved and re-precipitated along with seawater samples.  Three separate blanks were prepared from Weeks Island halite, a rock salt, during the processing of the samples.

## ANALYTICAL METHODS

Measuring the $^{36}$Cl/Cl ratio in ocean water has been elusive until recently owing to its very low value.  Even a significant source of $^{36}$Cl, such as atmospheric production, is extremely diluted with the large quantities of naturally occurring chloride in the ocean. AMS facilities routinely measure sample ratios down to $1 \times 10^{-14}$.  However, for this study, we needed to measure ratios

in the $10^{-16}$ range. This requires very high separation from the isobar $^{36}$S and long count times because of beam current limitations. Furthermore, we address the potential cross contamination in the accelerator injection source by running only very low level samples and standards prior to these analyses (Fifield et al., 2013). Samples were prepared using the standard Cl chemistry as described by (Conard et al., 1986). They were hand carried to Canberra, Australia where they were pressed into a Cu cathode wheel, surrounded by an AgBr mask. Cathode wheels were allowed to degas over 24 hours.

Negative chlorine ions from the 32-sample MC-SNICS ion source were mass-selected by the injection magnet, accelerated to the high-voltage terminal of the accelerator and stripped by ~2μg/cm$^2$ of oxygen gas. An electrostatic chopper located immediately after the injection magnet allowed the intense stable-isotope beams to be attenuated by a factor of 100 before injection into the accelerator in order to avoid beam-loading effects. Typical $^{35}$Cl$^-$ beam currents before attenuation were 15 μA. After the second stage of acceleration, chlorine ions in the 7$^+$ charge state were selected by the analyzing magnet for transport to the detector. A slow cycling procedure was employed in which both the injection magnet and accelerating voltage were adjusted to transmit sequentially $^{35}$Cl, $^{37}$Cl and $^{36}$Cl. Accelerating voltages of 14.40, 13.62, and 14.00 MV for $^{35}$Cl, $^{37}$Cl and $^{36}$Cl respectively ensured that all three isotopes had the same magnetic rigidity after acceleration. Hence, they could be transmitted to the detector station without the need to change any of the magnetic elements on the high-energy side of the accelerator. Fluxes of $^{35}$Cl$^{7+}$ and $^{37}$Cl$^{7+}$ ions were measured as electric currents in a removable Faraday cup positioned just in front of the gas-ionization detector. The gas-ionization detector makes five measurements of the energy loss of the ions as they slow and stop in propane gas. By

accelerating the ions to 112 MeV, excellent separation of [36]Cl ions from the much more abundant [36]S ions is achieved (Fifield et al., 2013).  Total [36]Cl counting times were 50 minutes for each sample, which were subdivided into five blocks of 10 minutes with [35]Cl and [37]Cl measurements between each block as well as at the beginning and end.  The methodology is described in more detail in (Fifield et al., 2009; Fifield et al., 2013).

## COSMOGENIC NUCLIDE PRODUCTION MODELING

To model the radiation cascade from cosmic-rays, we employ the radiation transport code MCNPX (Monte Carlo N-Particle eXtended) v2.7 developed and maintained by Los Alamos National Laboratories as described in Chapter 3 (Argento et al., 2013; James et al., 2006; Pelowitz, 2011).  We use (Usoskin and Kovaltsov, 2006) for the GCR source of both protons and alpha particles.  The model has 1033 g/cm$^2$ of dry air in 150 concentric spherical shells of varying density according to the US Standard Atmosphere 1976 (Dubin et al., 1976) up to 100 km over a planet of seawater, as described in Chapter 3.  Different latitudes are simulated by modifying the GCR source by angular rigidity cutoffs (O'Brien, 2008).  For this study we have simulations of 10 geomagnetic latitudes (including the unmodified source at high latitude) for the atmospheric calculations and 6 geomagnetic latitudes for the seawater calculations.  Atmospheric and oceanic compositions in the simulations are listed in Table 5.1a & 5.1b.

| Molecule | % by volume |
|----------|-------------|
| $N_2$ | 78.08 |
| $O_2$ | 20.95 |
| Ar | 0.93 |
| $CO_2$ | 0.038 |
| Ne | 0.0018 |
| He | 0.0005 |
| Kr | 0.0001 |
| H | 0.00005 |
| Xe | 8.70E-06 |

Table 5.1a – Atmospheric composition by volume used in simulations

| Z | Elements | concentration (g / kg seawater) |
|----|----------|--------------------------------|
| 3 | Li | 1.84E-04 |
| 5 | B | 4.49E-03 |
| 6 | C | 2.36E-02 |
| 7 | N | 5.10E-04 |
| 9 | F | 1.30E-03 |
| 11 | Na | 1.08E+01 |
| 12 | Mg | 1.28E+00 |
| 14 | Si | 2.25E-03 |
| 16 | S | 9.05E-01 |
| 17 | Cl | 1.94E+01 |
| 18 | Ar | 4.59E-04 |
| 19 | K | 3.99E-01 |
| 20 | Ca | 4.12E-01 |
| 35 | Br | 6.73E-02 |
| 37 | Rb | 1.23E-04 |
| 38 | Sr | 7.94E-03 |

Table 5.1b – Seawater composition used in simulations

Neutron and proton results are then folded with cross sections for production of $^{36}Cl$ as described

in Chapter 3 (Argento et al., 2013).  We utilize the cross sections of $^{36}Ar(n,p)^{36}Cl$,

$^{40}$Ar(n,4np)$^{36}$Cl and $^{40}$Ar(p,x)$^{36}$Cl (Reedy, 2013) for atmospheric calculations and $^{35}$Cl(n,$\gamma$)$^{36}$Cl (Guber et al., 2004) for seawater calculations.

## RESULTS

### Seawater measurements

Measurements made in November of 2008 are shown in Figure 5.1. The three blank samples had an average value of $5 \pm 2 \times 10^{-17}$. We assume that this is the inherent background of the 14UD Pelletron due to contamination and $^{36}$S isobar interference and perhaps even carrier chlorine signal. The nature of the background deserves further investigation.

The blank corrected, weighted average of $^{36}$Cl/Cl ratios of the seawater transect and Puget Sound sample is $6.3 \pm 0.8 \times 10^{-16}$ with a normalized chi squared result of 3.0. However, if one considers the 4200m-1 result to be an outlier, then the weighted average is $7.1 \pm 0.9 \times 10^{-16}$ with a normalized chi squared result of 0.22.

The results for three commercially available sea salts were $8.8 \pm 1.7 \times 10^{-16,}$ $8.5 \pm 1.7 \times 10^{-16}$, and $12.6 \pm 2.1 \times 10^{-16}$. This agrees well with the values of seawater, as expected.

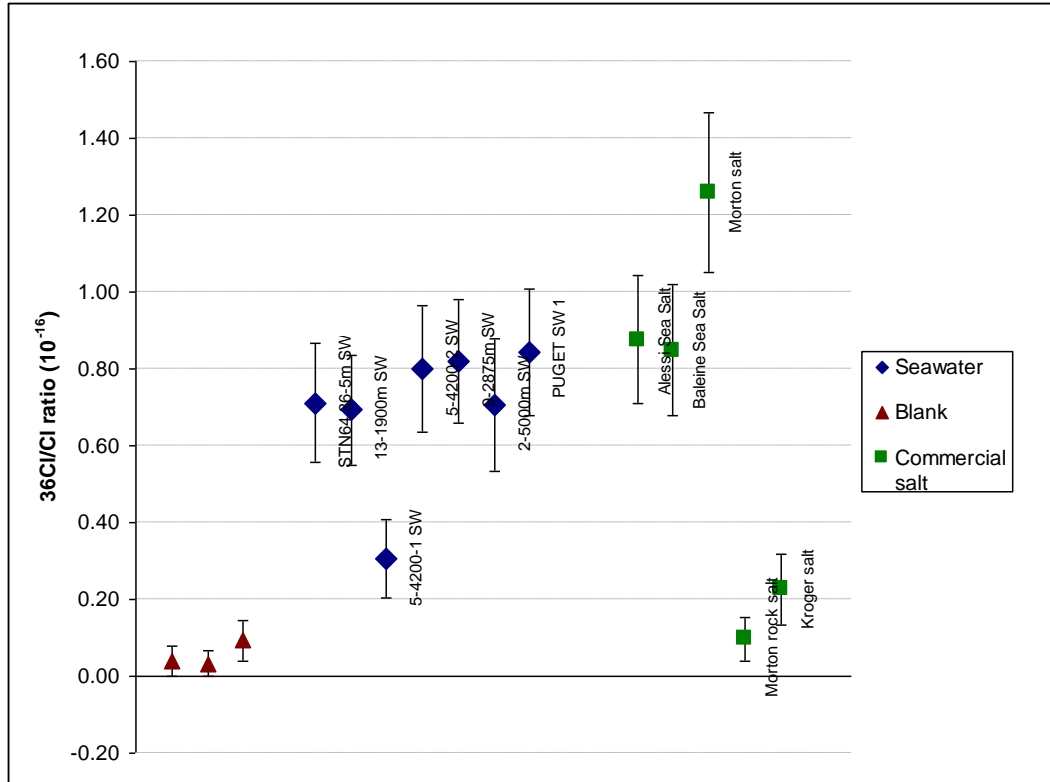Figure 5.1 – Accelerator mass spectrometry results from November 2008 (Fifield et al., 2013)

## Sources of $^{36}$Cl in the ocean

Chlorine-36 in the oceans has been postulated to come from five sources: i) spallation of atmospheric argon; ii) neutron capture by $^{35}$Cl in the ocean (Lal, 1999); iii) nuclear power and nuclear fuel reprocessing plants; iv) and spallation of Ca and K in the lithosphere which is eventually eroded and transported to the ocean; v) oceanic nuclear weapons testing. We estimate these sources here:

### i) Atmospheric production by spallation of argon

We use simulations of atmospheric cosmic-ray neutrons and protons at ten geomagnetic latitudes ranging from 0 to 16.4 GV vertical cutoff to determine the production of $^{36}$Cl by the $^{40}$Ar(n,4np)$^{36}$Cl, $^{40}$Ar(p,x)$^{36}$Cl and $^{36}$Ar(n,p)$^{36}$Cl reactions. Figure 5.2 shows the

altitude profile of atmospheric $^{36}$Cl production. Figure 5.3 shows the latitude profile (in

vertical cutoff rigidity) of the column integrated production. Figure 5.4 shows the

production binned in 5 degrees in geomagnetic latitude. We used the Elsasser Equation

(Dunai, 2010) to convert vertical cutoff rigidity to geomagnetic latitude, assuming

modern magnetic conditions. Using the (Usoskin and Kovaltsov, 2006) GCR results, we

calculate a global production of 16 g/yr which contributes to the oceanic equilibrium

$^{36}$Cl/Cl ratio contribution of $2.6 \times 10^{-16}$. Prior estimates of this value range from 9 – 30

g/yr $^{36}$Cl (Lal and Peters, 1967; Masarik and Reedy, 1995; O'Brien, 1979; Oeschger et al.,

1969; Phillips, 2000). These production rates would result in an oceanic equilibrium

$^{36}$Cl/Cl ratio contribution of 1.4 to $4.8 \times 10^{-16}$; the latter coming from Phillips' (2000)

estimate of 30 g/yr.
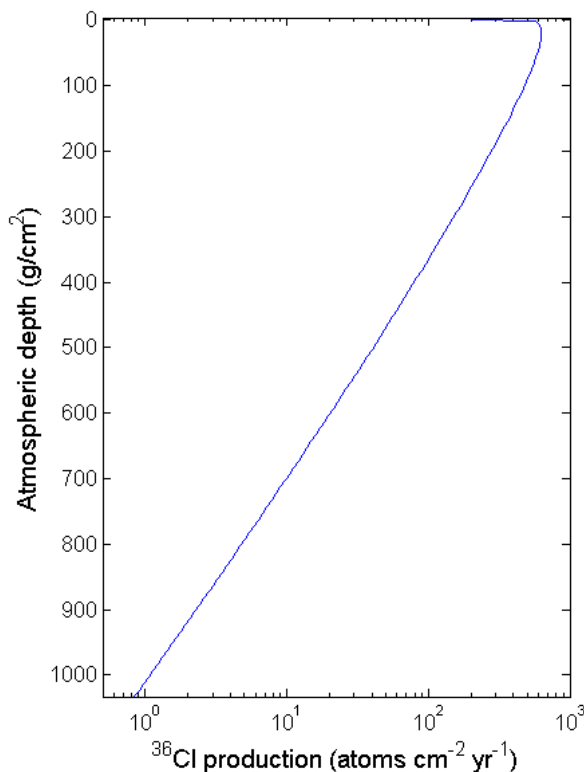


Figure 5.2 – Calculated production rate of $^{36}$Cl using
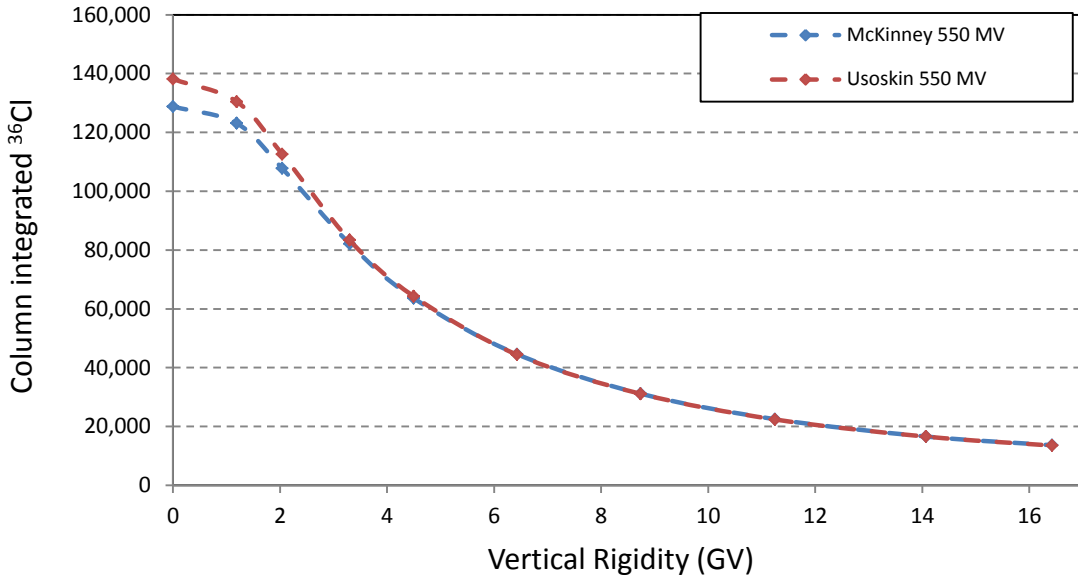Usoskin and Kovaltsov (2006) at high latitude as a
function of atmospheric depth

Figure 5.3 – Column integrated $^{36}Cl$ results as a function of vertical cutoff rigidity. Results using the two different GCR models are very similar at low latitudes, but diverge at higher altitudes. Both show a significant decrease with increasing cutoff due to the high flux of particles below 5 GeV.
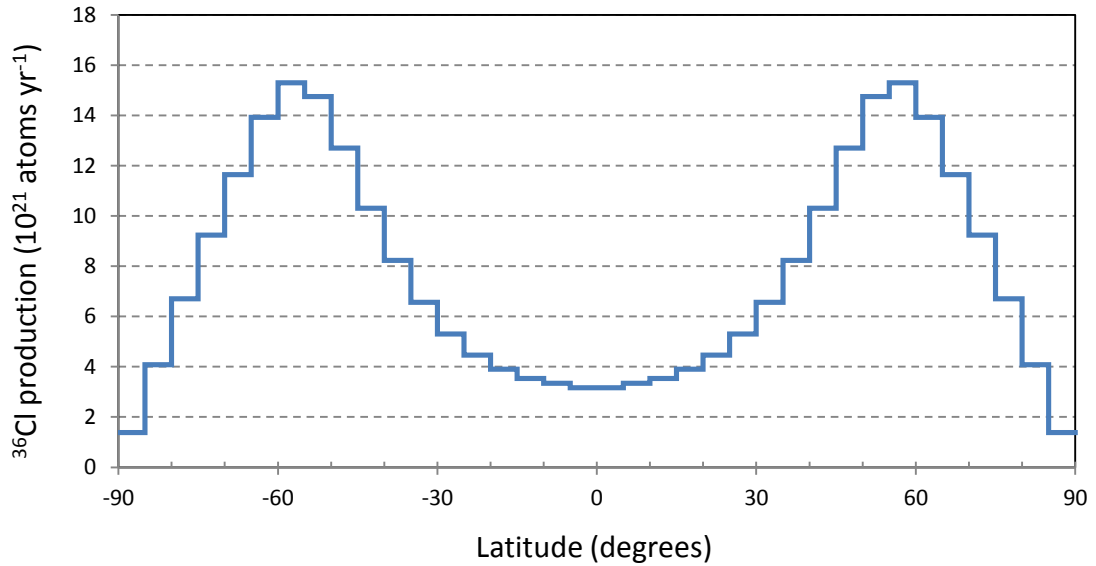


Figure 5.4 – Atmospheric production of $^{36}Cl$ using Usoskin and Kovaltsov (2006) GCR model in 5 degree bins. With decreasing latitude (from pole to equator), production diminishes, but surface area per 5° region increases, hence the peak near 50°.

## ii) Neutron capture by $^{35}$Cl in seawater

For seawater, we performed six simulations for different geomagnetic conditions modifying the Usoksin and Kovaltsov (2006) GCR spectra. Figures 5.5 and 5.6 show results for high-latitude $^{36}$Cl production as a function of depth. We see a sharp peak in the production of $^{36}$Cl via neutron capture at ~4 g/cm$^2$ below the surface, similar to the profile for thermal neutrons calculated in (O'Brien et al., 1978). Figure 5.7 shows the column integrated production of $^{36}$Cl as a function of vertical cutoff rigidity. We use current geomagnetic conditions and calculations of the ocean's surface area in 5 degree bands, shown in Figure 5.8. We calculate a global production of 6.7 g $^{36}$Cl /yr which results in a contribution of $1.1 \times 10^{-16}$ to the $^{36}$Cl/Cl ratio. In contrast, (Bentley et al., 1986) predicts a sub-aqueous production of 13 g/yr resulting in a $^{36}$Cl/Cl ratio contribution of $2.1 \times 10^{-16}$.
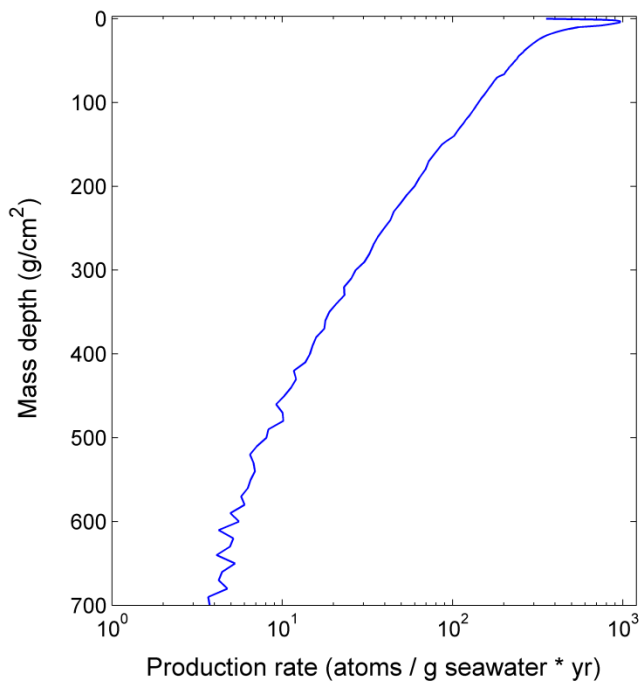


Figure 5.5 – Chlorine-36 production profile via neutron capture by chlorine-35. Statistics get worse lower in the regions, resulting in greater noise.
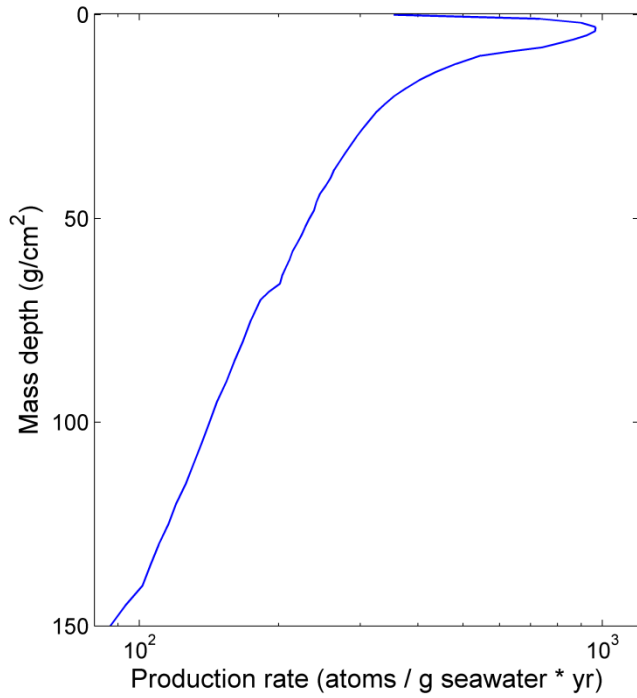
Figure 5.6 – Upper portion of seawater $^{36}$Cl production profile showing the peak in production similar to the peak in thermal neutrons in O'Brien (1978).



Figure 5.7 – Column integrated $^{36}$Cl production as a function of vertical rigidity cutoff.  Note the drop in production with increasing cutoff is less severe than atmospheric results.  While the flux of particles is significant at the lower end of the spectrum, the lower energy particles have much less penetrating power, thus contribute only a fraction of high altitude production at sea level.

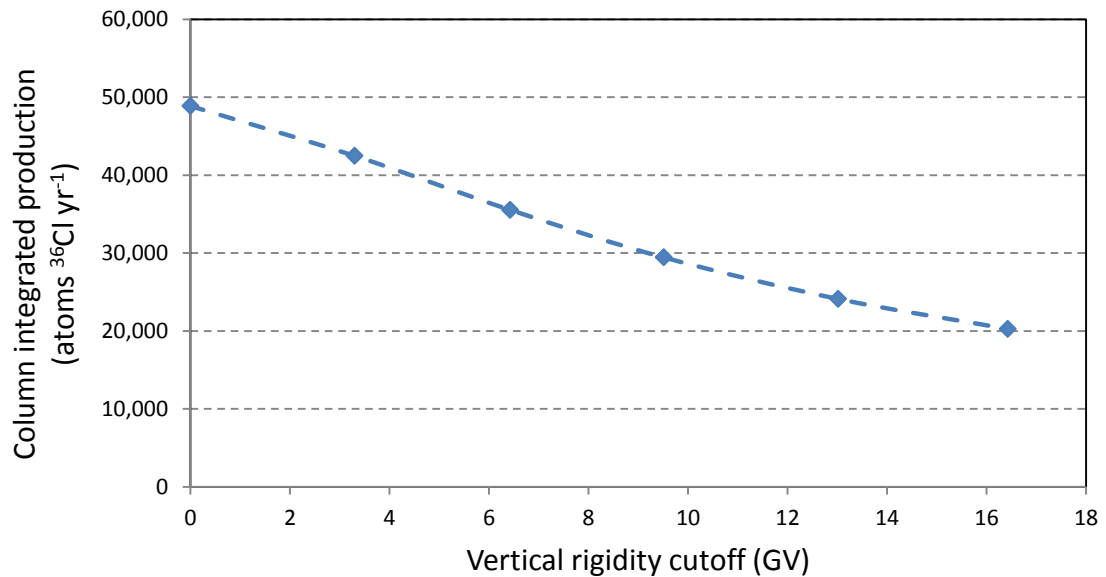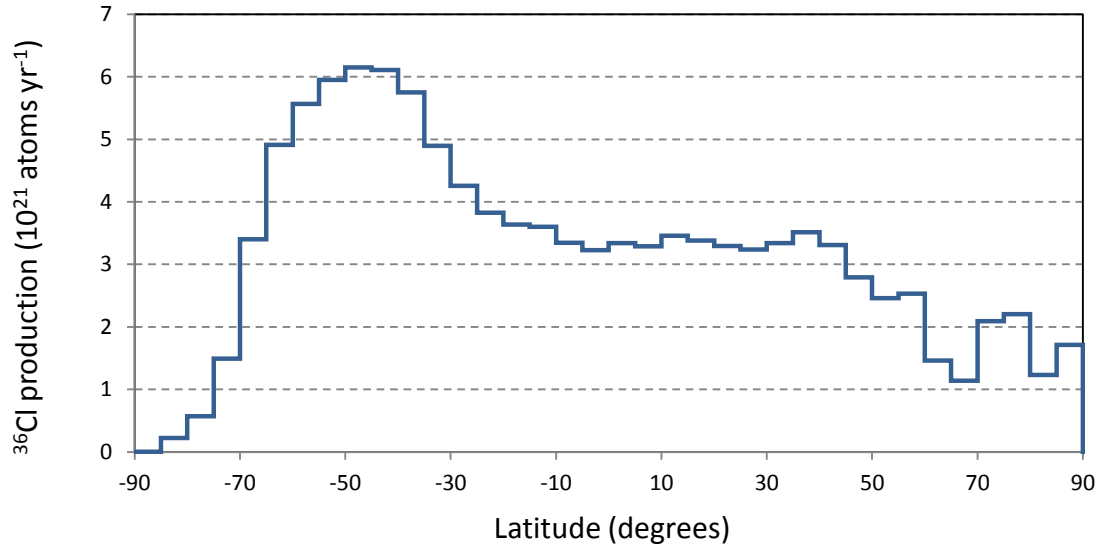Figure 5.8 – Oceanic $^{36}$Cl production in 5 degree bins. The asymmetry around the equator in production reflects the asymmetry in the ocean's surface area.

Calculations of neutron production from cosmic ray muons were performed, based on the incomplete isotope production of oxygen target nuclei in (Heisinger et al., 2002). The annual flux of neutrons produced from fast and slow muons was determined to be roughly 8 orders of magnitude lower than that of secondary neutrons resulting from spallation. Therefore we ignore this mode of production.

iii) Nuclear power and nuclear fuel reprocessing plants

River and ground waters utilized by nuclear reactors can show an elevated $^{36}$Cl/Cl ratio due to neutron absorption by $^{35}$Cl in the cooling water (Beasley et al., 1992). This source is insignificant in terms of global production owing to the very small total production from these point sources.

iv) Spallation of calcium and potassium in the lithosphere

Using an average crustal composition (Table 5.2), we make the assumption that the global average erosion rate is on the order of 20-30 m/Myr. Because *in-situ* production decreases exponentially with depth, the highest values are at the surface. This results in the efficient removal of the bulk of *in-situ* produced $^{36}$Cl and its rapid transport to the oceans. Using an average elevation of 800 m, an average continental latitude of 30°, and cosmogenic calibration data (Lal and Peters, 1967; Stone et al., 1996; Zreda et al., 1991), we estimate ~0.10 g of *in-situ* $^{36}$Cl per year is produced, leading to a contribution to the $^{36}$Cl/Cl ratio of $1.3 \times 10^{-18}$. This is well below current analytic sensitivity, and as shown above, two orders of magnitude lower than the atmospheric and oceanic production rates.

| Element | % by weight |
|---------|-------------|
| Oxygen | 46 |
| Silicon | 28 |
| Aluminum | 8 |
| Iron | 6 |
| Calcium | 2.4 |
| Sodium | 2.1 |
| Potassium | 2.3 |
| Magnesium | 4 |
| All others | 1 |

Table 5.2 – Crustal composition; Earth, Fourth Edition, Press & Siever

v) Oceanic Weapons Testing

Nuclear weapons tests produced $^{36}$Cl via neutron absorption by the $^{35}$Cl in the seawater nearby the testing sites. Chlorine-36 is created in ocean-based nuclear tests when fission neutrons are absorbed by seawater $^{35}$Cl. According to (Bentley et al., 1982), 82 kg of $^{36}$Cl was produced, vaporized and subsequently injected into the troposphere and

stratosphere.  Bomb-pulse isotopes such as $^{3}$H and $^{14}$C have been used by oceanographers to track the mixing process of surface waters (ocean isotope reference - WOCE).  Over the last forty years, these isotopes have been seen to mix to depths of ~1000 m across the oceans (Feely et al., 2006).  Assuming that $^{36}$Cl diffuses in the same manner and has reached these depths yields a $^{36}$Cl/Cl ratio on the order of $1 \times 10^{-17}$, again, well below analytical sensitivity.


## DISCUSSION

Under current geomagnetic conditions, seventy percent of $^{36}$Cl produced in the atmosphere is produced in the stratosphere and the remainder in the troposphere.  The portion of $^{36}$Cl formed in the stratosphere has a residence time of several months, whereas the residence time in the troposphere is about one week (Bentley et al., 1986).  This is effectively instantaneous with respect to the half-life of $^{36}$Cl; very little of the atmospherically produced $^{36}$Cl should decay prior to reaching the oceans.


Hammer (1986), reports endorheic (internally drained) basins make up 10% of the area of continental land mass.  However, they are extremely arid.  Ultra-low precipitation is a requirement for these regions to remain isolated from the oceans; otherwise, the erosion from runoff will quickly carve a channel to the ocean.  Therefore, because these regions are 3% of the global area, and they are at a severe deficit in precipitations, the effect of entrapped atmospheric $^{36}$Cl is considered negligible for endorheic basins.

Water masses in ice caps have a mean average residence time much shorter than the half-life of $^{36}$Cl. Even if all $^{36}$Cl precipitated onto the primary ice sheets and ice caps were sequestered long enough to decay away completely, this would account for only ~3% of the atmospherically produced $^{36}$Cl. While there are regions which have very old ice, this is the rare exception; very little of the annual precipitation is locked up as ice for time spans that are significant in comparison with the $^{36}$Cl half-life. Considering realistic transit times, decay of $^{36}$Cl in ice mass is also considered to be negligible.

**Chloride-36 sinks**

There are no significant sinks for $^{36}$Cl aside from radioactive decay. Sea spray is a significant remover of chlorine out of the oceans. However, it is generally considered to be brought back to the ocean rapidly, so this should not be a significant sink for the isotope. The only true large sink for chloride out of the oceans is episodically removing large volumes of seawater from communication from the rest of the oceans, causing evaporitic deposition (Graedel and Keene, 1996). The last major episode of deposition occurred 5 million years in the Messinian when the Mediterranean evaporites were deposited (Roveri et al., 2006). This leaves removal via subduction of ocean sediments into the mantle. This process is estimated to remove <.00000001 % of the chlorine per year and we can ignore this effect (Graedel and Keene, 1996).

**Total $^{36}$Cl inventory**

Summing up the various sources, we arrive at a total predicted input of 22 g $^{36}$Cl per year which leads to steady-state $^{36}$Cl/Cl ratio of $3.6 \times 10^{-16}$. Because the three sources of $^{36}$Cl are directly

tied to the cosmic ray flux, the production rates in the past should in fact be modified to compensate the paleomagnetic field (Lifton, 2008; Masarik and Beer, 2009).

Because the Earth's magnetic field has on average been lower than it is currently (Korte et al., 2011; Valet et al., 2005), the total production rate of $^{36}$Cl should be higher in the past. In addition, the solar magnetic field has been theorized to be lower on average during the Holocene (Steinhilber et al., 2010). We expect integrating paleomagnetic and solar modulation data with production rate calculations to account for at least some of the discrepancy between our calculated results and the average measured $^{36}$Cl/Cl ratio. Another significant source of uncertainty is the $^{40}$Ar$(n,x)^{36}$Cl spallation cross section which is estimated to have 15% uncertainty at any point. The other proposed sources of $^{36}$Cl have been shown to be negligible in their contribution to the ocean's inventory.

## CONCLUSION

Measuring the $^{36}$Cl/Cl ratio of seawater has been a long held goal in the cosmogenic nuclide community for its potential to provide insight to atmospheric production rates as well as a measure of the cosmic ray flux in the past. Measuring the $^{36}$Cl/Cl ratio of seawater has also been a goal for the AMS community because of the inherent challenge of accurately measuring such a low ratio. In this study, we present the measured $^{36}$Cl/Cl ratio of seawater to be $7.1 \pm 0.9 \times 10^{-16}$. Analyses of ultra-low ratio samples such as these requires: i) extreme care in the sample preparations to ensure maximum reduction of sulfur, ii) proper attention to reducing cross-contamination in the ion source, and iii) tuned detector gating to discriminate the residual $^{36}$S.

The majority of $^{36}$Cl in seawater originates from spallation of argon in the atmosphere and neutron capture by $^{35}$Cl in the oceans; both processes are driven by the cosmic-ray flux impinging on the Earth. Integration of $^{36}$Cl simulation results with paleomagnetic data and models for the last million years can be used as an important benchmark for terrestrial cosmic-ray modeling.

# REFERENCES

Argento, D.C., Reedy, R.C., Stone, J.O., 2013. Modeling the earth's cosmic radiation. Nuclear Instruments and Methods B 294, 464-469.

Argento, D.C., Stone, J.O., Fifield, L.K., Tims, S.G., 2010. Chlorine-36 in Seawater. Nuclear Instruments and Methods B 268, 1226-1228.

Beasley, T.M., Elmore, D., Kubik, P., Sharma, P., 1992. Chlorine-36 Releases from the Savannah River Site Nuclear Fuel Reprocessing Facilities. Ground Water 30, 539-548.

Bentley, H.W., Phillips, F.M., Davis, S., 1986. Chlorine-36 in the terrestrial environment, In: Fritz, P., Fontes, J.-C. (Eds.), Handbook of environmental isotope geochemistry - The terrestrial environment. Elsevier, Amsterdam, Netherlands, pp. 427-480.

Bentley, H.W., Phillips, F.M., Davis, S., Gifford, S., Elmore, D., Tubbs, L.E., Gove, H.E., 1982. Thermonuclear 36Cl pulse in natural water. Nature 300, 737-740.

Berner, E.K., Berner, R.A., 1987. The global water cycle. Prentice-Hall.

Castagnoli, G., Lal, D., 1980. SOLAR MODULATION EFFECTS IN TERRESTRAIL PRODUCTION OF CARBON-14. Radiocarbon 22, 133-158.

Conard, N.J., Elmore, D., Kubik, P., Gove, H.E., Tubbs, L.E., Chrunyk, B.A., Wahlen, M., 1986. THE CHEMICAL PREPARATION OF AgCl FOR MEASURING 36Cl IN POLAR ICE WITH ACCELERATOR MASS SPECTROMETRY. Radiocarbon 28, 556-560.

Dubin, M., Hull, A.R., Champion, K.S.W., 1976. US Standard Atmosphere, 1976. 241.

Dunai, T.J., 2010. Cosmogenic nuclides: principles, concepts and applications in the Earth Surface Sciences, First ed. Cambridge University Press, Cambridge.

Feely, R., Sabine, C., Millero, F., Wanninkhof, R., Hansell, D., 2006. Carbon Dioxide, Hydrographic, and Chemical Data Obtained During the R/V Thomas Thompson Cruise in the Pacific Ocean on CLIVAR Repeat Hydrography Sections P16N_2006 (Feb. 14 - Mar. 30, 2006). . Carbon Dioxide Information Analysis Center,  Oak Ridge National Laboratory, US Department of Energy, Oak Ridge, Tennessee, p. Available from: <http://cdiac.ornl.gov/oceans/RepeatSections/clivar_p16n.html>.

Fifield, L.K., Tims, S.G., Fujioka, T., Hoo, W.T., Everett, S.E., 2009. Accelerator Mass Spectrometry with the 14UD accelerator at the Australian National University.

Fifield, L.K., Tims, S.G., Stone, J.O., Argento, D.C., De Cesare, M., 2013. Ultra-sensitive measuremtns of 36Cl and 236U at the Australian National University. Nuclear Instruments and Methods B 294, 126-131.

Finkel, R.C., Nishiizumi, K., Elmore, D., Ferraro, R.D., Gove, H.E., 1980. 36Cl IN POLAR ICE, RAINWATER AND SEAWATER. Geophysical Research Letters 7, 983-986.

Galindo-Uribarri, A., Beene, J.R., Danchev, M., Doupe, J., Fuentes, B., Gomez del Campo, J., Hausladen, P.A., Juras, R.C., Liang, J.F., Litherland, A., Liu, Y., Meigs, M.J., Mills, G.D.,

Mueller, P.E., Padilla-Rodal, E., Pavan, J., Sinclair, J.W., Stracener, D.W., 2007. Pushing the limits of accelerator mass spectrometry. Nuclear Instruments and Methods B 259, 123-130.

Graedel, T.E., Keene, W.C., 1996. The budget and cycle of Earth's natural chlorine. Pure and Applied Chemistry 68, 1689-1697.

Guber, K.H., Leal, L.C., Sayer, R.O., Koehler, P.E., Valentine, T.E., Derrien, H., Harvey, J.A., 2004. New Neutron Cross Section Measurements at ORELA for Improved Nuclear Data. The Physics of Fuel Cylces and Advanced Nuclear Systems: Global Developements PHYSOR 2004.

Hammer, U.T., 1986. Saline lake ecosystems of the world. Dr. W. Junk Publishers, Dordrecht; Boston.

Heisinger, B., Lal, D., Jull, A.J.T., Kubik, P., Ivy-Ochs, S., Knie, K., Nolte, E., 2002. Production of selected cosmogenic radionuclides by muons: 2. Capture of negative muons. Earth and Planetary Science Letters 200, 357-369.

Herut, B., Starinsky, A., Katz, A., Paul, M., Boaretto, E., Berkovitz, D., 1992. $^{36}Cl$ in chloride-rich rainwater, Israel. Earth and Planetary Science Letters 109, 179-183.

Huggle, D., Blinov, A., Stan-Sion, C., Korschinek, G., Scheffel, C., Massonet, S., Zerle, L., Beer, J., Parrat, Y., Gaeggeler, H., Hajdas, V., Nolte, E., 1996. Production of cosmogenic $^{36}Cl$ on atmospheric argon. Planetary Space Science 44, 147-151.

James, M.R., McKinney, G.W., Hendricks, J.S., Moyers, M., 2006. Recent enhancements in MCNPX: Heavy-ion transport and the LAQGSM physics model. Nuclear Instruments and Methods A 562, 819-822.

Keywood, M.D., Fifield, L.K., Chivas, A.R., Cresswell, R.G., 1998. Fallout of chlorine 36 to the Earth's surface in the southern hemisphere. Journal of Geophysical Research 103, 8281-8286.

Kneis, D.L., Elmore, D., Sharma, P., Vogt, S., Li, R., Lipschutz, M.E., Petty, G., Farrell, J., Monaghan, M.C., Fritz, S., Agee, E., 1994. $^{7}Be$, $^{10}Be$ and $^{36}Cl$ in precipitation. Nuclear Instruments and Methods B 92, 340-344.

Korte, M., Constable, C., Donadini, F., Holme, R., 2011. Reconstructing the Holocene geomagnetic field. Earth and Planetary Science Letters 312, 497-505.

Kovaltsov, G.A., Mishev, A., Usoskin, I.G., 2012. A new model of cosmogenic production of radiocarbon $^{14}C$ in the atmosphere. Earth and Planetary Science Letters 337, 114-120.

Lal, D., 1988. Theoretically expected variations in the terrestrial cosmic-ray production rates of isotopes, In: Castagnoli, G. (Ed.), International School of Physics (1985). North-Holland, Varenna on Lake Como, pp. 216-233.

Lal, D., 1999. An overview of five decades of studies of cosmic ray produced nuclides in oceans. The Science of the Total Environment 237/238, 3-13.

Lal, D., Malhotra, P.K., Peters, B., 1958. On the production of radioisotopes in the atmosphere by cosmic radiation and their application to meteorology. Journal of Atmospheric and Terrestrial Physics 12, 306-328.

Lal, D., Peters, B., 1967. Cosmic Ray Produced Radioactivity on the Earth, In: Flugge, S. (Ed.), HANDBUCH DER PHYSIK. Springer-Verlag, Berlin, Heidelberg, New York, pp. 551-608.

Libby, W.F., 1946. Atmospheric Helium Three and Radiocarbon from Cosmic Radiation. Physical Review 69, 671-672.

Lifton, N.A., 2008. In situ cosmogenic 14C from surfaces at secular equilibrium. Geochimica et Cosmochimica Acta 72, A552.

Masarik, J., Beer, J., 1999. Simulation of particle fluxes and cosmogenic nuclide production in the Earth's atmosphere. Journal of Geophysical Research D104, 12099-13012.

Masarik, J., Beer, J., 2009. An updated simulation of particle fluxes and cosmogenic nuclide production in the Earth's atmosphere. Journal of Geophysical Research - Atmospheres 114, 1-9.

Masarik, J., Reedy, R.C., 1995. Terrestrial cosmogenic-nuclide production systematics calculated from numerical simulations. Earth and Planetary Science Letters 136, 381-395.

Murray, J.W., 1992. The Oceans, In: Butcher, S.S., Charlson, R.J., Orians, G.H., Wolfe, G.V. (Eds.), Global Biogeochemical Cycles. Academic Press Inc., San Diego, pp. 175-209.

O'Brien, K., 1979. Secular Variations in the Production of Cosmogenic Isotopes in the Earth's Atmosphere. Journal of Geophysical Research 84, 423-431.

O'Brien, K., 2008. Limitations of the Use of the Vertical Cut-off to Calculate Cosmic-ray Propogation in the Earth's Atmosphere. Radiation Protection Dosimetry 128, 259-260.

O'Brien, K., Sandmeier, H., Hansen, G., Campbell, J., 1978. Cosmic Ray Induced Neutron Background Sources and Fluxes for Geometries of Air Over Water, Ground, Iron, and Aluminum. Journal of Geophysical Research 83, 114-120.

Oeschger, H., Houternmans, J., Loosli, H., Wahlen, M., 1969. The constancy of cosmic radiation from isotope studies in meteorites and on the Earth, Nobel Symposium. Nobelstiftelsen : Stockholm, International, Stockholm, International.

Parrat, Y., Hajdas, W., Baltensperger, U., Synal, H.A., Kubik, P., Gaggeler, H.W., Suter, M., 1996a. Atmospheric Production Rate of 36Cl, In: Baltensperger, U., Lorenzan, R. (Eds.), Paul Scherrer Institute, Annual Report 1996, Annex III A. Paul Scherrer Institute, Villigen, Switzerland, p. 87.

Parrat, Y., Hajdas, W., Baltensperger, U., Synal, H.A., Kubik, P., Suter, M., Gaggeler, H.W., 1996b. Cross section measurements of proton induced reactions using a gas target. Nuclear Instruments and Methods B 113, 470-473.

Pelowitz, D.B., 2011. MCNPX User's Manual, Version 2.7.0, In: Energy, D.o. (Ed.). Los Alamos National Laboratory.

Phillips, F.M., 2000. Chlorine-36, In: Cook, P.G., Herczeg, A.L. (Eds.), Environmental tracers in subsurface hydrology. Kluwer Academic Publishers, Boston, pp. 299-348.

Reedy, R.C., 2013. Cosmogenic-Nuclide production rates: reaction cross section update. Nuclear Instruments and Methods B 294, 470-474.

Roveri, M., Manzi, V., Lugli, S., Schreiber, B.C., Caruso, A., Rouchy, J.-M., Iaccarino, S.M., Gennari, R., Vitale, F.P., Ricci Lucchi, F., 2006. CLASTIC VS. PRIMARY PRECIPITATED EVAPORITES IN THE MESSINIAN SICILIAN BASINS, In: Barbieri, F. (Ed.), R.C.M.N.S. Interim Colloquium "The Messinian salinity crisis revisited - II". Acta Naturalla de "L'Ateneo Parmense", Parma, Italy, pp. 125-199.

Steinhilber, F., Abreu, J.A., Beer, J., McCracken, K.G., 2010. Interplanetary magnetic field during the past 9300 years inferred from cosmogenic radionuclides. Journal of Geophysical Research 115.

Stone, J., Allan, G.L., Fifield, L.K., Cresswell, R.G., 1996. Cosmogenic chlorine-36 from calcium spallation. Geochimica et Cosmochimica Acta 60, 679-692.

Usoskin, I.G., Kovaltsov, G.A., 2006. Cosmic ray induced ionization in the atmosphere: Full modeling and practical applications. Journal of Geophysical Research 111, 1-9.

Valet, J.-P., Meynadier, L., Guyodo, Y., 2005. Geomagnetic dipole strength and reversal rate over the past two million years. Nature 425, 802-805.

Zreda, M.G., Phillips, F.M., Elmore, D., Kubik, P.W., Sharma, P., Dorn, R.I., 1991. Cosmogenic chlorine-36 production rates in terrestrial rocks. Earth and Planetary Science Letters 105, 94-109.

# Chapter 6


# Conclusion

# SUMMARY

The aims of this thesis are to address gaps in the knowledge of cosmogenic nuclide systematics, thereby reducing uncertainties for researchers employing cosmogenic nuclides to measure exposure ages or erosion rates. To accomplish those aims, I have built a comprehensive, first-principles model of cosmogenic nuclide production. Cosmic-ray particle fluxes are simulated using the radiation transport software, MCNPX. Particle fluxes are tallied with respect to both angle and energy. Nuclide production rates are determined by folding the particle flux results with nuclear reaction cross sections. Systematics such as nuclide specific scaling and geometric shielding are investigated as functions of altitude and geomagnetic latitude.

# IMPLICATIONS

This research has several significant implications for the use of cosmogenic nuclides in earth sciences. Numerous aspects of nuclide production systematics are difficult to address through natural calibration. This work is focused on those aspects such as nuclide specific scaling, angular distribution of nuclide producing particles, and subsurface production profiles. Chlorine-36 measurements of seawater are presented and discussed as a unique benchmark for terrestrial cosmic-ray models.

The production rate model presented in this dissertation shows that nuclear physics and radiation transport codes have evolved to the point that sea level high latitude cosmogenic nuclide production rates can be modeled successfully. This model has the potential to become a platform

for developing a purely physics-based scaling scheme for the prediction of global production rates. Geologic calibration data can be used as benchmarks for the performance of this model.

The work contained in Chapter 2 shows the initial results yielded by the model. Initial comparisons with Dr. Paul Goldhagen's ER-2 neutron measurements are used as the primary validation. Production rates ratios are investigated and shown to change with altitude. Subsurface production rates are also shown to be neither strictly exponential, nor having significant plateaus at the surface. Rather, production decreases gently near the surface and transitions to a steady exponential at depth. The characteristics of the profiles are unique for each nuclide and rock type.

Nuclide specific scaling is addressed quantitatively in Chapter 3 and demonstrates that using the same scaling for all nuclides introduces small, pervasive systematic error into production rate calculations. However, with further characterization of production ratios and further calibration sampling, this facet of nuclide production systematics could be used to researchers' advantage.

The work in Chapter 4 focuses on using the model to develop parameterized production rates as functions of altitude and sophisticated corrections for production rates. The immediately applicable result from this research is the derivation of physically justified geometric shielding corrections. Simulation results show that the conventional method of estimating shielding corrections underestimates the contribution of cosmic-rays at low horizon angles. Low angle horizon obstructions are frequently encountered when sampling, making this a pervasive systematic error in cosmogenic nuclide production rate estimates. The results also indicate that

the nuclide producing particle distribution becomes more collimated with decreasing altitude; the resulting exponent in the cosine component decreases with increasing altitude and increases with latitude.

Subsurface production rate profile simulations indicate nuclide specific scaling also occurs below the surface, leading to production ratios changing with depth. Attenuation lengths near the surface are longer than those at depth. In addition, both the attenuation lengths and production ratios show sensitivity to the average atomic mass of the rock. The systematics with which production ratios change as a function of average atomic mass need to be better constrained to reduce this source of error.

Chapter 5 discusses measurements and calculations of seawater $^{36}$Cl/Cl as recorders of the long-term average cosmic-ray flux impinging on the top of the atmosphere. Chlorine-36 is produced both in the atmosphere from spallation of $^{40}$Ar and in the ocean when chlorine-35 captures cosmic-ray neutrons. Calculations of $^{36}$Cl production in the atmosphere and oceans are made by folding simulation results with cross sections. Current calculations based on the modern geomagnetic field and a mean solar modulation of 550 MV estimates about half of the $^{36}$Cl production rate necessary to explain the measured $^{36}$Cl/Cl ratio of the ocean. This is likely because the production of $^{36}$Cl in the upper atmosphere is very sensitive to the changing solar and geomagnetic field, and currently, our calculations do not account for this. Paleomagnetic and solar data suggest that both of these parameters would lead to increased production.

# LIMITATIONS

In the current form, this model is limited in its geomagnetic scope. Having a maximum of 16.4 GV vertical cutoff is not sufficient for examining production rates during Earth's periods of greatest magnetic strength (Korte et al., 2011). Ideally, simulations would have a vertical cutoff of up to 20 GV. Greater resolution within that range, especially between 0 and 3 GV to characterize the "knee" in production rate would be optimal. In all cases except for the Bonner Sphere benchmark simulations, the long-term solar modulation average 550 MV is used, as determined by Reedy (1987). However, Steinhilber (2008) suggests that the average for the Holocene is closer to 500 MV. Lower solar modulation would mostly affect *in-situ* production rates in the uppermost geomagnetic latitudes, but should be considered nonetheless. More importantly, it can strongly influence atmospheric production rates.

Perhaps the greatest limitations to this system are the uncertainties in the radiation transport and cross sections. Estimated to be around ~15%, these uncertainties are poorly defined. The uncertainties associated with the radiation transport are likely small; however, the simulations are large in spatial extent, making compounding errors a serious concern. Because of the massively statistical nature to these simulations, there is no way to formally address the uncertainties beyond calculations of statistical uncertainty based on the number of particles reported in MCNPX. Uncertainties also enter the system from the GCR model. Lastly, if developed into a proper scaling scheme, the long term history of both the solar modulation and the geomagnetic shielding will also add uncertainties that may be difficult to assess.

# IMPROVEMENTS

This dissertation contains both the methodology and results of a comprehensive, physics-based cosmogenic nuclide production model. The latest high-energy nuclear transport models are utilized in conjunction with the latest cosmogenic production rate nuclear cross-sections. Several GCR models have been tested, with two (McKinney et al., 2006; Usoskin and Kovaltsov, 2006) being used to generate results. GCR results are modified by angular cutoff calculations provided by Keran O'Brien (O'Brien, 2008). The model has been validated against sea level calibration measurements, high-altitude calibration measurements, and neutron spectrum measurements (Goldhagen et al., 2002; McKinney et al., 2012).

By folding neutron and proton spectra with nuclear reaction cross sections the model predicts nuclide specific production rates for all cosmogenic nuclides in all minerals for which I have corresponding cross sections. This allows investigation of changes in production ratios with altitude and latitude, and depth in multiple rock types. Angular information is captured in addition to energy in these simulations allowing investigation of angular production rates topographic shielding corrections.

The first reliable measurements of the $^{36}$Cl/Cl ratio in seawater presented in this dissertation (Argento et al., 2010; Fifield et al., 2013). Calculations of atmospheric and oceanic $^{36}$Cl production rates using current geomagnetic conditions don't match the production needed to generate the measured concentrations. These measurements of the $^{36}$Cl/Cl ratio in seawater can be developed into an important benchmark for cosmic-ray models such as this one.

# FUTURE WORK

The work contained in this thesis shows that current high-energy transport and modern geologically relevant nuclear cross-sections are capable of reproducing sea level productions within cross section uncertainties. Much work is left to be done to expand the geomagnetic latitude simulations and other solar conditions.

To fully assess the performance of this model, production rate results can be integrated with geomagnetic data / models to develop a formal scaling scheme. Integrating the scaling scheme into the CRONUS web calculator (Balco 2008) would make the results of the model immediately accessible to researchers worldwide. Furthermore, building this capability will provide a platform for comparison of this model's various permutations against each other, as well as against other scaling schemes. Acquisition and testing of nuclear cross-sections developed by other physicists should also be pursued.

According to this model, angular distribution of nuclide forming particles is both latitude and altitude dependent. Furthermore, in all cases, there is both a near-horizontal and upward oriented component to the distribution. The results suggest that some of these low-angle particles originate locally while some originate from greater distances. This would imply that shielding corrections are also dependent on proximity to the shielding object (i.e., nearby boulder vs. distant mountain).

Non-concentric objects are the next geometric aspect to develop in this model. A concern within the cosmogenic user community is the production profile within non-planar surfaces such as boulders. This model can be modified to investigate such objects and surfaces.

Terrestrial cosmogenic nuclide production, especially at the surface, is very sensitive to the accuracy of the high energy spallation model used. I am eager to work with radiation transport developers to explore possible modifications to the high energy models using terrestrial cosmogenic calibration data as benchmarks.

There are numerous other opportunities to benchmark this system. (Kowatari et al., 2005) has a series of Bonner Sphere measurements made at several altitudes along the flanks of Mt. Fuji. Many muon studies can be used to benchmark the muon results. Lunar cosmogenic studies would also be valuable benchmarks for the system.

The research described in this thesis represents the basis for a comprehensive cosmogenic nuclide production system. This system will illuminate production systematics that are difficult to assess empirically, assess uncertainties, and function as a test bed for proposed physics such as alternative nuclear reaction cross-sections and alternative paleomagnetic models.

# REFERENCES

Argento, D.C., Stone, J.O., Fifield, L.K., Tims, S.G., 2010. Chlorine-36 in Seawater. Nuclear Instruments and Methods B 268, 1226-1228.

Fifield, L.K., Tims, S.G., Stone, J.O., Argento, D.C., De Cesare, M., 2013. Ultra-sensitive measuremtns of 36Cl and 236U at the Australian National University. Nuclear Instruments and Methods B 294, 126-131.

Goldhagen, P., Reginatto, M., Kniss, T., Wilson, J.W., Singleterry, R.C., Jones, I.W., Van Steveninck, W., 2002. Measurement ofthe energy spectrum of cosmic-ray induced neutrons aboard an ER-2 high-altitude airplane. Nuclear Instruments and Methods A 476, 42-51.

Korte, M., Constable, C., Donadini, F., Holme, R., 2011. Reconstructing the Holocene geomagnetic field. Earth and Planetary Science Letters 312, 497-505.

Kowatari, M., Nagaoka, K., Satoh, S., Ohta, Y., Abukawa, J., Tachimori, S., Nakamura, T., 2005. Evaluation of the Altitude Variation of the Cosmic-ray Induced Environmental Neutrons in the Mt. Fuji Area. Journal of Nuclear Science and Technology 42, 495-502.

McKinney, G.W., Armstrong, H.J., James, M.R., Clem, J.M., Goldhagen, P., 2012. MCNP6 Cosmic-Source Option. Transactions of the American Nuclear Society 106.

McKinney, G.W., Lawrence, D.J., Prettyman, T.H., Elphic, R.C., Feldman, W.C., Hagerty, J.J., 2006. MCNPX benchmark for cosmic ray interactions with the Moon. Journal of Geophysical Research 111, 1-14.

O'Brien, K., 2008. Limitations of the Use of the Vertical Cut-off to Calculate Cosmic-ray Propogation in the Earth's Atmosphere. Radiation Protection Dosimetry 128, 259-260.

Usoskin, I.G., Kovaltsov, G.A., 2006. Cosmic ray induced ionization in the atmosphere: Full modeling and practical applications. Journal of Geophysical Research 111, 1-9.